UNIVERSITÀ DEGLI STUDI DI PADOVA

Dipartimento di Fisica e Astronomia “Galileo Galilei”

Master Degree in Physics

Final Dissertation

Spectroscopic characterization and numerical modelling of an IEC device

Thesis supervisor
Dr. Gianluigi Serianni
Thesis co-supervisors
Dr. Roger J.E. Jaspers
Dr. Emanuele Sartori

Candidate
Margherita Altin

Academic Year 2019/2020

A mamma, papà, Elia ed Elena,
per avermi su(o)pportato incondizionatamente.

Abstract

In an inertial electrostatic device, a potential well is built between concentric electrodes, in order to confine energetic ions. High densities of ions may be obtained due to the formation of virtual electrodes inside the hollow cathode grid, though relevant parameters influencing their formation are still to be understood. The objective of this project is to characterize plasma discharge in a fusor, with particular stress on the potential well shape.

An experiment exploiting Doppler shift produced by fast excited hydrogen atoms is developed; the kinetic energy of fast neutrals is determined along a microchannel during Star mode operation and prominent population of diverging neutrals is established in a pressure range between 0.3 Pa and 1.5 Pa. Increase of neutral kinetic energy is detected outside the cathode grid, reaching $\sim 40\%$ of the applied potential.

A Particle-In-Cell simulation of the fusor is developed to support experimental data interpretation and gain an in-depth knowledge of particle behaviour inside the machine. The equilibrium population of the discharge is in accord with previous results and Star mode operation is achieved. Virtual anode formation is not observed, but synthetic spectra are extracted from the simulated discharge revealing that absence of virtual anode does not produce the desired spectrum, while imposing its presence as an input causes spectra to show the same features of experimental ones, corroborating the hypothesis of virtual anode formation.

Contents

Chapter 1

Introduction to IEC devices

1.1 Operating principle and current experiments

Inertial Electrostatic Confinement (IEC) of charged particle was developed as an alternative way of producing fusion reactions.

Electrostatic confinement alone cannot be exploited to confine a plasma; this can be understood intuitively: if plasma is produced in an electrostatic potential, ions will eventually be accelerated towards the potential well and will be separated from the electrons, causing the neutralization of the potential and subsequently the loss of the plasma.

IEC devices deal, however, with a dynamical situation (whence the term *inertial*). To understand how this works, let us consider a simple type of IEC device, the gridded one. Such device consists in an outer vessel, which serves as anode and an inner spherical grid, which serves as cathode. When a plasma is created inside this device, one would expect the ions to be attracted by the gridded cathode and enter the space inside it. The electric field is null inside the cathode (considering the solution of the Laplace equation), therefore the ion is not slowed down and reaches the other side of the cathode with the same kinetic energy it had at the entrance; the ion then exits the cathode and travels towards the vessel until its velocity is reversed and the motion repeats itself cyclically.

This oscillatory motion provides the possibility that ions with high kinetic energy collide in the centre, with an energy high enough to cause fusion reaction between the two projectiles.

This picture is highly ideal and does not take into consideration limits introduced both by the engineering of the machine and by the underlying physics. The former refers to possible asymmetries both in the vessel and in the cathode geometry, which modify the operating regimes of the fusor. The latter refers to effects that cause loss of fast ions, such as charge exchange reactions, space charge repulsion and possible ion up-scattering due to elastic collisions. Such losses cause a reduction of the characteristic confinement time of the machine. Limits of the fusor are found both in achieving the correct ion energy and the large confinement time; in order to exploit resonances of fusion reactions, energy of $\sim 100keV$ are required (this is the case of $deuterium - tritium$ fuel): with the simple concept of ions being born at the wall and accelerated by the potential, such energy seems relatively simple to achieve, but scattering and charge exchange may prevent ions from reaching the centre and therefore reaching the required energy. As for the confinement time, it can be estimated as the diameter divided by the average ion velocity (therefore it would be related to ion recirculation); the same reactions that limited kinetic energy, limit the confinement time. In particular, one could try to apply Lawson criterion to an IEC device, though remembering that it is just an approximate indication of the required operation parameters, as the ion population is expected not to be Maxwellian. For a D-T fuel, Lawson criterion at $T_i = 25keV$ is $n\tau = 10^{14} s/m^3$. Assuming a core density of $10^{16} m^{-3}$, the criterion leads to the necessity of 0.01s confinement time.

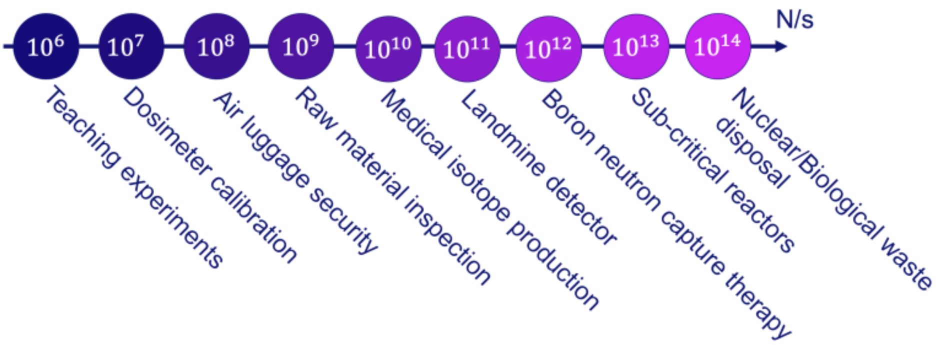

Figure 1.1: Possible applications of neutron fluxes [29].

A critique of the concept of inertial electrostatic confinement was thoroughly conducted by Rider [38].

Without getting in the details linked to the machine design, one can point out several phenomena that cause power losses in timescales significantly smaller than the one for fusion reaction; such phenomena are ion thermalization, ion upscattering and bremsstrahlung losses.

Firstly, ion thermalization poses a limit to the dream of having almost mono-energetic fast ions, which would be necessary to exploit resonances in the fusion cross-section (particularly for aneutronic fuels like $p -^{11} B$). When an ion beam is inserted in an IEC device, its particles start spreading in the velocity space, causing the convergence of their energy distribution to a Maxwellian with a time scale equal to the ion-ion collision time. Considering on up- and down-scattering of radial velocity one can show that:

$$\frac{\tau_{i1-i1}}{\tau_{fus}} = 1.0 \cdot 10^7 \frac{\sqrt{\mu_{i1}} T_{i1}^{3/2} \langle \sigma v \rangle}{Z_{i1}^4 ln(\Lambda_{i1-i1})} \frac{n_{i2}}{n_{i1}} \tag{1.1}$$

for typical values of $\langle \sigma v \rangle \approx 10^{-16} - 10^{-15}\text{cm}^3/\text{s}$ and $T_{i1} \approx 50 - 100keV$ it is found that (1.1)$\sim 10^{-3} - 10^{-2}$, thus indicating that the mono-energetic ions are lost in a time scale 3 orders of magnitude smaller than the one of fusion reactions.

Another energy loss mechanism in a fusor is related to the loss of fast ions due to collisions with other ions. If the kinetic energy of ions is even just half of the potential well, they will be scattered out and lost in a few ion-ion collision times.

Finally, bremsstrahlung losses must be evaluated, due to the fact that they are impossible to reduce. Power loss due to bremsstrahlung is prohibitively large for all fuels excepting $D-T$, $D-D$ and $D-^3He$ [38]. Electron temperature used to evaluate such losses can be calculated by equating the ion-electron heat transfer rate to the cooling rate of electrons due to bremsstrahlung.

Despite such limitations, which undermine the possibility of reaching break-even with an IEC device, the machine has many other applications related to neutron production. The advantages offered by an IEC device are the low-cost engineering and the portability of the device. Commercially relevant neutron production rates must reach values larger than $10^8 s^{-1}$. Possible applications are shown in Fig.1.1.

In order to optimize neutron production, subsequent IEC concepts were elaborated. The first project dates back to 1966: Farnsworth and Hirsch [12][18] elaborated a machine (the original project is shown in Fig.1.2) with concentric electrodes, two of which were partially transparent and allowed the movement of ions and electrons through them. Farnsworth idea was to produce eletrons with a low voltage glow discharge between the outer vessel and the middle grid, extract the electrons produced in such discharge and accelerate them towards the centre using the inner positively-biased grid. The negative space charge formed in the centre by the converging electrons would cause the build-up of a virtual cathode and the consequent attraction of ions born in the intergrid region.

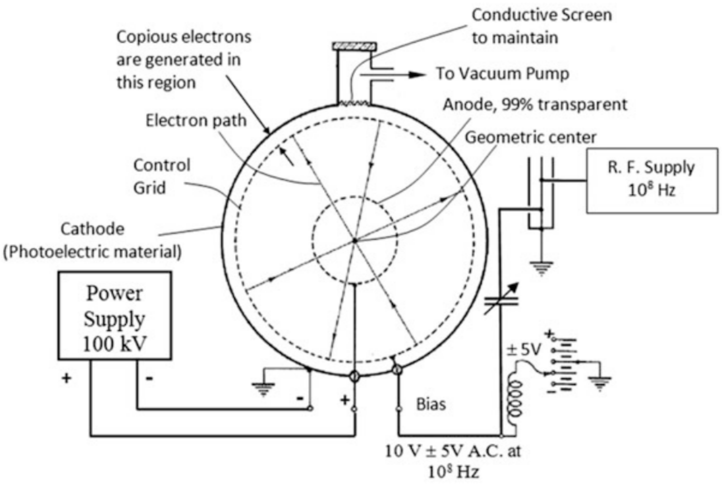

Figure 1.2: Original project by Farnsworth [12].

Many improvements have been made on this machine ever since, the most relevant of which was the inversion of the electrode order: using an outer anode and an inner cathode, thus exploiting ion current towards the centre.
All following developments have gone into the direction of limiting energy losses, which are mostly caused by electrons and ions hitting the electrodes.

1.1.1 Confining potential

Part of the optimizing journey consists also in designing the potential well in such a way to better confine high energy ions.
One of the most investigated potential features of a fusor is the possibility of self-forming concentric potential wells and hills (called virtual electrodes or, as will be clear later, Poissors).
As described above, focusing of ion current in the centre of the cathode grid may lead to the formation of a virtual anode, capable of confining electrons and therefore one potential well, where ions may be confined, increasing their density.
The electron confinement may lead theoretically to the formation of a virtual cathode (potential well) where ions are confined; this process may lead to the birth of a nested configuration of virtual electrodes. However, spread in the velocities of ions and the presence of trajectories with a non-null angular momentum leads to the restriction of having a maximum of 2 virtual nested electrodes; the presence of the innermost potential well caused by enhanced electron density is possible only at high ion currents. The benefits of the presence of nested electrodes would be higher ion density and higher recirculation current (higher confinement time).
The mechanism of formation of a virtual anode is still not established, however two main phenomena may be responsible of it according to literature. First, the positive space charge accumulation due to ion focusing in the centre and secondly, the space charge accumulation due to ionization of the central region; the latter can be understood in the following way: if most ionization reactions occur in the centre (which is expected, due to ion convergence and secondary electron emission towards the centre), then the core will be dominated by ions, rather than electrons. In fact, due to lower inertia, electrons will leave the central region faster, while ions may linger there longer. This model would then lead on to predict electron accumulation as the virtual anode grows and therefore lead to virtual cathode formation, and so on. It is clear that both phenomena must collaborate in order to keep virtual anode at a significant intensity.
First calculation of what are now called *Poissors* was carried out by Elmore, Tuck and Watson [8] considering electrons as primary particles and by Hirsch [18], considering ions as "primary particles". In both cases, very strong assumptions were made to make calculations easier.

Firstly, background gas is completely ignored and the only present species are ions and electrons; this excludes ion losses via charge exchange or slowing down of particles due to collisions with slower particles. Secondly, ions and electrons with only one energy are considered, which is physically impossible to obtain, for many ions are born in the region between the anode and the cathode grid, giving rise to an energy distribution dependent on the distance from the centre at which the ion population is observed, as will be seen in detail in Sec.4.

Nevertheless, their derivation might be of some help when trying to guess what is at least the shape of the virtual anode inside the grid.

Both studies are set to derive the shape of multiple nested electrodes, Potential in the chamber satisfies the Poisson's equation (in CGS units) in spherical coordinates:

$$\frac{1}{r^2}\frac{d}{dr}\left[r^2\frac{dV(r)}{dr}\right] = -4\pi(\rho_i(r) + \rho_e(r)) \tag{1.2}$$

where $\rho(r)$ is the charge density and the subscript i and e stand for *ions* and *electrons* respectively.

We will consider the potential to be 0 at the virtual anode, while potential at the cathode (real) will be V_0; under such conditions conservation of energy entails:

$$\frac{1}{2}m_i v_i^2 = e|V(r)| \tag{1.3}$$

$$\frac{1}{2}m_e v_e^2 = e(V(r) - V_0) \tag{1.4}$$

choosing normalized variables:

$$\phi(r) = V(r)/V0 \tag{1.5}$$

$$R = r/r_a \tag{1.6}$$

where r_a is the position of the virtual anode.

By defining:

$$K_+ = \frac{I_i}{|V_0|^{3/2}}\left(\frac{m_i}{2e}\right)^{1/2} \tag{1.7}$$

$$\lambda_+ = \frac{I_e}{I_i}\left(\frac{m_e}{m_i}\right)^{1/2} \tag{1.8}$$

Poisson's equation can be rewritten as:

$$\frac{d^2\phi}{dR^2} + \frac{2}{R}\frac{d\phi}{dR} = \frac{K_+}{R^2}\left[\phi^{-1/2} - \lambda_+(1-\phi)^{-1/2}\right] \tag{1.9}$$

Assuming that the virtual anode defines the zero potential, then necessarily $\phi(R = 1) = 0$; close to such value the second term in brackets on the R.H.S can be easily neglected, due to the dominance of the first term, and the equation can be solved according to Langmuir-Blodgett:

$$\phi(R) \approx (\frac{9}{4}K_+)^{2/3}(R-1)^{4/3} \tag{1.10}$$

Eq.1.9 was solved using finite difference method, starting from $R = 1$ and calculating the first two values by Eq.1.10. Solutions for $K_+ = 1$ and different values of λ_+ are shown in Fig.1.3. The result is in accord with what is presented in Hirsch's study. It can be noticed that a λ_{max} exists, above which the curve does not reach $\phi = 1$, that is, it does not satisfy the boundary condition that at some point the potential must reach the cathode voltage. This method allows to calculate the shape of the virtual anode and the distance between virtual anode and real cathode for different values of K_+ and λ_+. The information about the relative distance will not be used, as it will be assumed that in the proposed experiment only one virtual electrode

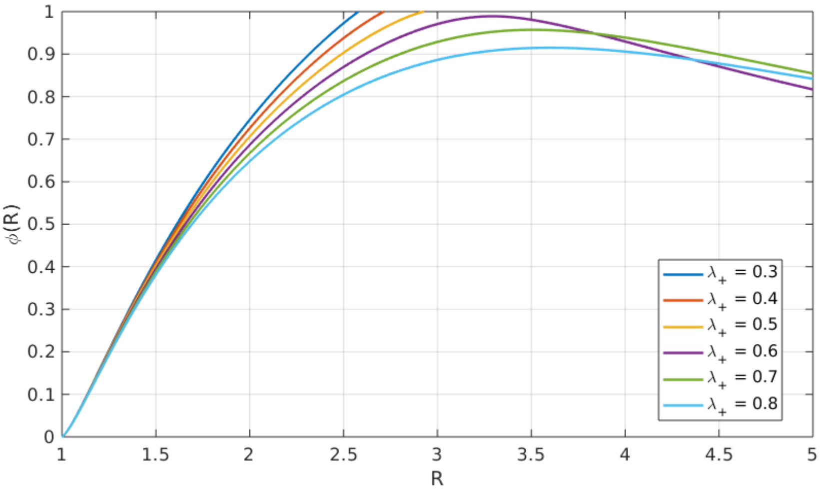

Figure 1.3: Shape of the virtual anode, reproduced from Hirsch article. Note that to have the shape we are familiar with, the values should be multiplied by the value of cathode voltage (V_0 <0).

is formed, exactly at the center of the cathode grid, so that such distance is fixed by the real apparatus.

The shape of the virtual anode can be fit with a parabola with 95% confidence level.

The expected evolution of potential, ion density profile and proton rate is depicted in Fig.1.4 [31].

Neutron production is expected to raise in the inner region due to virtual cathode formation. If the inner cathode is deep enough, energetic ions may be trapped inside, creating the right enviroment for fusion.

Hirsch's results show the possibility of the formation of a double well in a spherical IEC device, the properties of which are dependent upon grid transparency, angular momentum spread and energy spread of the particles. In particular, clear virtual electrodes appear when spread in ion energy and ion angular energy are small; the depth also depends on the ratio $\frac{I_i}{I_e}$ and on the ion perveance $\frac{I_i}{V_c^{3/2}}$.

Further development of Hirsch work was carried out by Hu and Klevans [20], who included energy and angular momentum distribution of ions. In particular, the introduced distribution was determined in order to self-consistently find Hirsch solution of concentric potential wells. They found that the effect of spread in the angular momentum of ions on the formation of a virtual anode is critical only in the case of low values of perveance of the ion beam ($K < 0.1$): very small deviation from radial motion of ions will prevent the system from forming a clear virtual electrode. On the other hand, for $K > 1$, one can expect such formation even with a spread in angular momentum.

Hu and Klevans also highlighted the importance of high grid transparency to guarantee high ion recirculation current. Large grid transparency is linked to very broad openings on the grid, which would lead to a poor ion focusing, thus contradicting the conditions posed above; however, if the fusor is operated in Star mode (which will be described in the following sections), high focusing and broad openings can be present at the same time.

Further effort to determine the physical conditions in which a virtual anode might form was carried out by Black and Klevans [6], who once again indicated focusing and mono-energetic energy distribution as crucial conditions for virtual anode formation; they also argued that charge exchange reactions and poor grid spherical symmetry would have a degrading effect on such process.

Tzonev and colleagues [44] used a 1D uncollisional code, in order to provide limiting case for virtual anode formation, showing the formation of a virtual anode even in the presence of angular

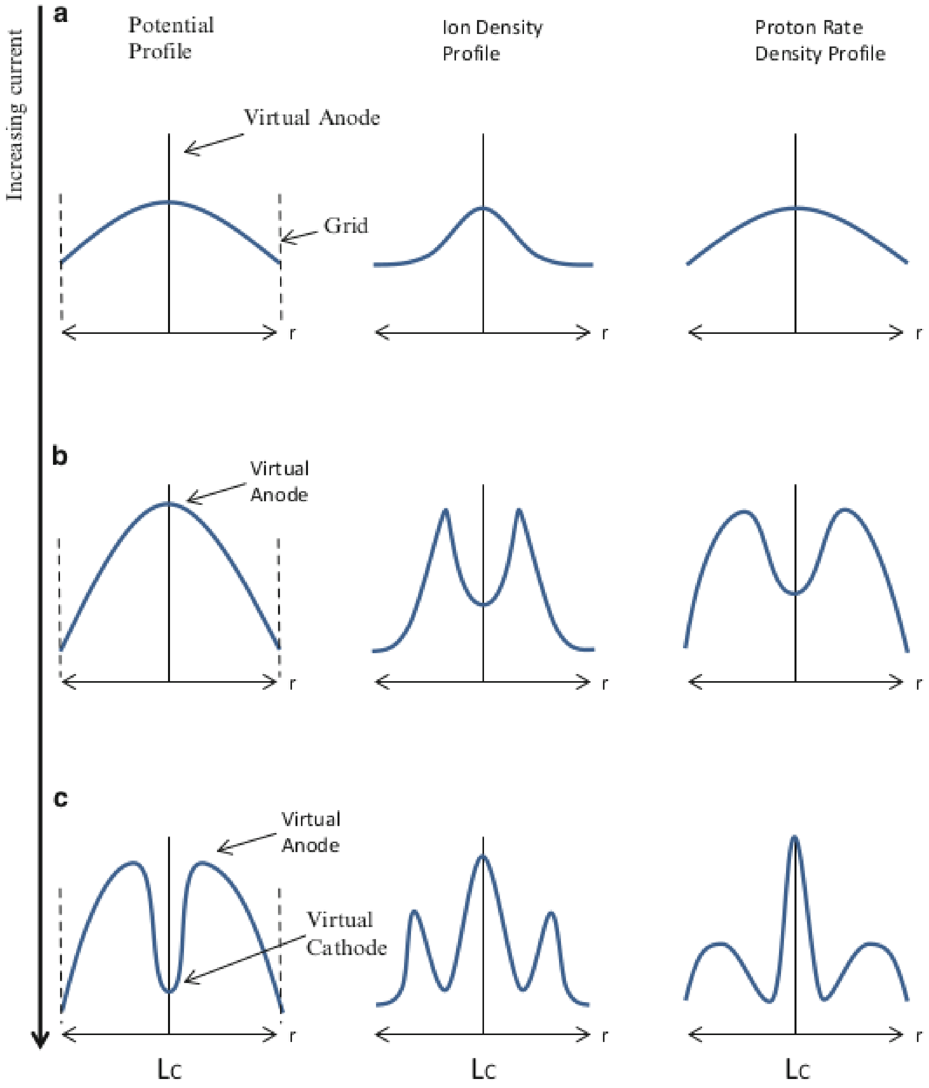

Figure 1.4: Expected behaviour of potential, proton density and neutron yield as current is increased [31]

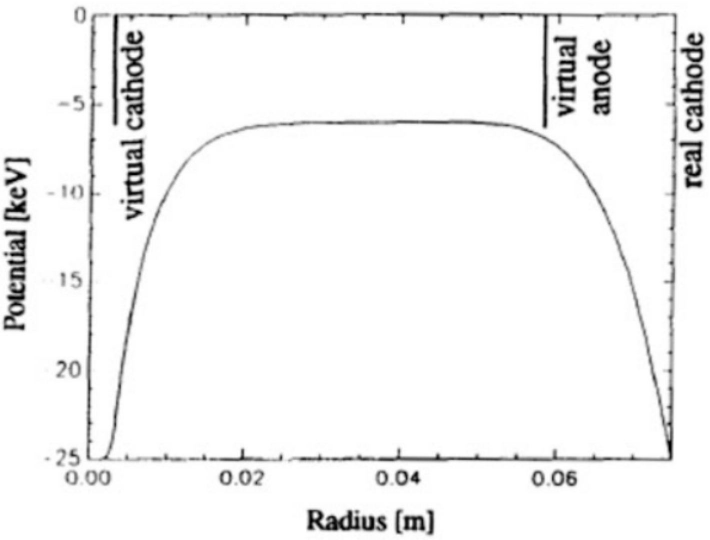

Figure 1.5: Tzonev et al.[44] simulated structure for virtual anode and inner virtual cathode with the IXL 1D code.

momentum spread, though with a more spread out shape than the one obtained by Hirsch. The result is shown in Fig.1.5. The general dependence of virtual anode height lies, according to simulation, in the perveance of recirculating ion current. Tzonev employed ion currents of the order of $\sim 50A$.

The first notable experimental attempt to observe potential wells in a spherical IEC were conducted by Hirsch [18]. He designed an experimental apparatus capable of providing very sharp ion focusing. To do this, he used 6 ion guns capable of operating at currents between 10mA and 60mA, positioned at diametrically opposite positions.

To detect the presence of potential wells he measured firstly neutron production rate in a D-T discharge; results show a sharp maximum in emission intensity at the centre, followed by two symmetrical peaks on the side.

Moreover, he detected bremsstrahlung emission from electrons, which would be slowed down by the presence of virtual anodes. The shape of gamma emission resembled the one obtained with neutron detection.

Though such results were very positive for a further development of the IEC fusor, they were never reproduced.

Following experimental studies showed contradictory results. In particular, Kachan detection of a virtual anode during star-mode operation [22] was contradicted by Thorson [42], who detected a flat potential inside the cathode and Yoshikawa [47], who detected negligible electric field in such spot.

On the other hand, Kachan measured ion kinetic energy by employing Doppler spectroscopy on a single microchannel [21]; to do so he used a peculiar biconical cathode. The probe measurements he presented are susceptible of doubt, since probe is expected to perturbe the ion velocity and behaviour along the microchannel.

Gu and Miley [15] measured the proton density profile in the attempt of proving the presence of multiple potential wells and argued that a lower energy spread might be achieved by adding a floating grid between anode and cathode. Their results show clear peaks in proton production at certain distances from the central spot.

1.2 Fusion reactions

Fusion reactions in an IEC device may occur between the three main types of particles present in the machine: fast ions, fast neutrals and background neutrals. This section will cover the main mechanisms that lead to neutron production in a fusor.
If we consider two species of colliding particles (1 and 2), heading towards each other with relative velocity v, the number of reactions per unit time can be calculated as:

$$R = \int n_1 n_2 \sigma(v) v dV \tag{1.11}$$

where $\sigma(v)$ is the velocity-dependent cross section.
Particles colliding in a fusor may be of different nature.
Beam-beam fusion is obtained when two fast ions head towards each other. In order to give an estimation of the contribution given from such kind of collision, the density of fast ions is necessary. Assuming typical values of ion current ($\sim 50mA$), applied voltage ($\sim 20kV$) and core radius ($\sim 5mm$), fast ion density can be estimated as $n_{i,f} = I/(evA) \approx 5 \cdot 10^{14} m^{-3}$; the reactivity is therefore proportional to the square of ion current. Since such density is roughly five orders of magnitude lower than background gas density, such reaction channel is considered negligible. Fast particle colliding with background gas provide a reactivity proportional to $n_{i,f} n_{gas}$.
Fast ions may result in the formation of fast neutrals via charge-exchange, which may in turn collide and fuse with the background gas. This contribution is significant if the mean free path for charge exchange reactions , that is $\lambda_{mfp} = 1/(n_{gas}\sigma_{cx})$ is smaller than the fusor dimension.
Finally, if a virtual electrode forms inside the cathode grid, it is possible to confine inside the potential well a thermal plasma; if temperature is high enough (tens of keVs), then fusion reaction become relevant also among ion in such a plasma. However, evidence of high temperature in such region has not been provided.
As a conclusion: if the most relevant processes are beam-background and neutral-background fusion, then the reaction rate scales linearly with the background gas pressure; however, limitations of electrostatic confinement mentioned above, undermine such dependency.
The most advantageous mode of operation of a fusor is the Star-mode operation, as microchannels have the following beneficial effects on fusion reactivity:

- The higher density of particles on microchannels causes most fusion reactions to happen in such regions [32];
- The only ions that hit the cathode grid are the ones scattered out of the microchannel: this causes a reduction in ion losses and therefore an increase of grid transparency [30];
- Microchannels are filled preferentially by high energy ions (this will be shown in Sec.4), thus increasing fusion reactivity. The reason is that fast ions are less affected by potential perturbations near the grid [30].

1.3 Gas discharge in a spherical device

Many experimental IEC devices employ a gas discharge between the electrodes as the ion source, rather than an external ion gun.
In the case examined in this thesis, the discharge is initiated and sustained by a DC voltage. The physical explanation of a DC discharge ignition can apply to any geometry, though quantitative results must be derived for each specific case. In order to understand the underlying mechanism, the case of linear geometry will be taken into consideration and later adapted to the spherical case. An electrical discharge is considered to be initiated when ion and electron losses are balanced by the source function. In particular, source terms consist of background ionization

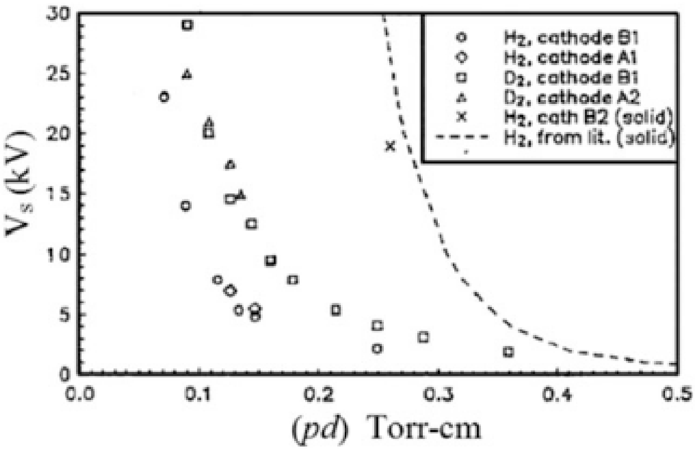

Figure 1.6: Breakdown voltage for different cathodes [30].

and secondary electron emission from the electrodes.

Due to their lower inertia, electrons are the first to be affected by the potential applied to the electrode plates. They are present in the vessel before ignition due to cosmic rays ionization. If the applied potential is increased to a threshold value (V_t), such electrons acquire enough kinetic energy to produce ionization on their path towards the anode. From each ionization reaction another electron is born, which can cause further ionization, thus leading to an avalanche and to an exponential increase of the number of electron-ion pairs in the vessel. In turn, ions are accelerated towards the cathode and cause secondary electron emission from the electrode, which adds up to the source terms.

The value of the applied potential required to initiate a discharge in a linear device depends on pressure and on the distance between the electrodes according to Paschen law:

$$V_t = \frac{B(pd)}{C + log(pd)}, \quad C = log\left(\frac{A}{log(1/\gamma + 1)}\right) \tag{1.12}$$

where γ is the secondary electron emission coefficient and A and B are parameters related to the specific gas filling the vessel.

Miley et al.[30] investigate experimentally the breakdown of a discharge in a IEC spherical device, showing the dependence of breakdown voltage on the product *pd*.

The value d was assumed to be the difference between the chamber radius and the spherical cathode radius.

Fig.1.6 shows the behaviour of the breakdown voltage as a function of *pd* for different types of cathode grids, including a comparison with a solid cathode. As can be seen, hollow cathode grids allow for a lower breakdown voltage for low value of *pd*, thus suggesting the importance of microchannel formation in discharge evolution.

A scaling law was proposed in the article to determine breakdown voltage as a function of the ratio $A/(pd)^2$, where A is the mass of the background gas in *a.m.u.*.

1.3.1 Operating regimes

Any IEC device may operate in three different regimes depending mostly on pressure and cathode-anode geometry.

Star mode operation and microchannel creation was discovered at University of Illinois Urbana-Champaign labs and typically takes place at low pressure $\leq 2Pa$; microchannels present themselves as sharp stokes crossing the cathode grid and focusing on the centre, causing a bright

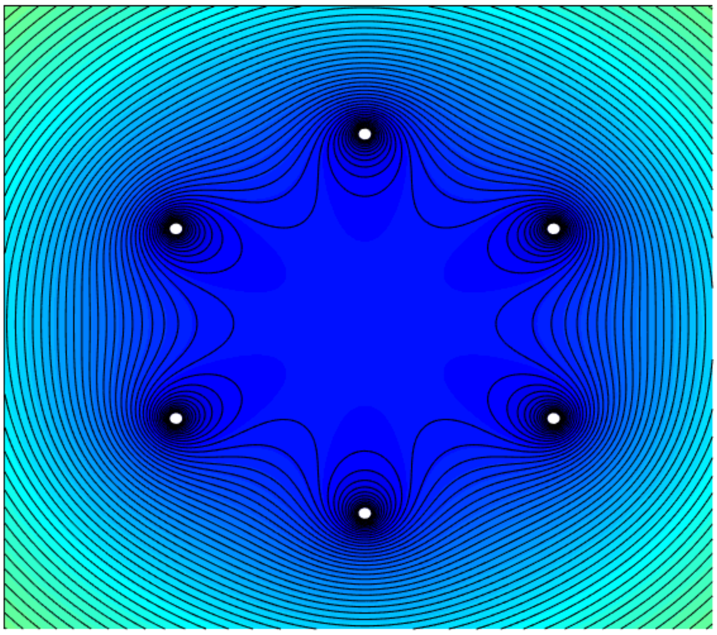

Figure 1.7: Potential near the cathode grid.

spot in such position. Such operation mode allows high ion focusing, without compromising grid transparency.

Microchannels are created due to the perturbed non-spherical structure of the potential near the grid. Such potential has the shape shown in Fig.1.7

The potential exhibits a maximum between two grid wires, therefore defining a preferential position for electrons; such structure works as a trough, through which electrons preferentially move. Once electrons are ejected outwards they cause ionization of background gas. The ions that are formed along their trajectories are positioned in a way that causes them to accelerate towards the cathode grid passing through the grid open, therefore enhancing their focusing in the center of the machine. Negative space charge accumulation along the microchannel enhances ion movement along the channel.

Movement along the channels reduces the probability of an ion hitting the cathode grid, effectively enhancing grid transparency.

To test the hypothesis of the enhanced grid transparency Miley et al. [30] performed experiments using grids with equal geometric transparency, but with holes drilled on them in order to have either diametrically opposing holes or holes oriented 90° with respect to each other; the first case allowed the formation of a microchannel and therefore very high transparency was detected.

As pressure is increased, transition to glow-mode operation is expected. The transition coordinates in terms of pressure, voltage and current depend on the specific geometry and on the type of gas, but it is recognisable due to the uniform glow and the absence of spokes. Mean free path in glow-mode is shorter and ions are usually born very close to the cathode grid and lost easily through charge exchange reactions, reducing ion recirculation and therefore confinement time.

Operation in Jet-mode can be observed only at interemediate pressure values and if the cathode grid shows a larger aperture, causing electrons and ions to move preferentially along the axis of such aperture; jet mode can be easy recognised through the emitted radiation, which is located in correspondence of the larger aperture.

1.3.2 Ion flow and density

As already mentioned before, fast ion density and ion convergence are two important factors contributing to the efficiency of an IEC device.
Using a simple non-collisional model it is possible to derive an estimation for the plasma core radius and ion density. In order to develop such first order model, several strict assumptions must be made:

- All ions are assumed to be non-interacting;
- Neither sources nor sinks are present in the vessel;
- Only ions generated at the edge (radius equal to R) are considered;
- Ions converge to a core of radius r_c;

Due to conservation of angular momentum $M\langle v_\perp \rangle R \approx (2/3)Mv_c r_c$, where v_c is the velocity reached by ions when they get to the core; the identity states that the angular momentum of the ion at the edge should be equal to its angular momentum in the centre.
The core radius is therefore approximated as:

$$r_c = \frac{3}{2}R\frac{\langle v_\perp \rangle}{v_c} \approx \frac{3}{2}R\sqrt{\frac{k_B T_{\perp i}(R)}{qV_c}} \tag{1.13}$$

where $T_{\perp i}$ is the temperature associated with motion perpendicular to the radial velocity at the vessel edge, while V_c is the applied cathode voltage. Knowledge of core radius is fundamental to optimize beam-beam fusion, which is advantageous if resonance peaks in fusion cross section are to be exploited; in fact, previously it was stated that beam-beam fusion is proportional to the square of the ion current: however, if the increasing current causes an increase in core radius, the resulting beam-beam reactivity will scale with current slower than expected.
Thorson et al.[43] have measured experimentally the core size, concluding that it decreases with applied potential, having a steeper variation as the spacing between grid wires is increased.
Since it is assumed that neither sources nor sinks are present in the model, the number of ions must be conserved as well as ion current through each spherical shell; this leads to $n_i(r)v(r)r^2 = const$, where v is the velocity normal to the spherical shell, therefore the radial component of velocity.
Therefore, due to current conservation:

$$n_{ic} = 4n_i(R)\left(\frac{R}{r}\right)^2 \frac{v(R)}{v(r)} = n_i(R)\left(\frac{R}{r}\right)^2 \sqrt{\frac{E_\parallel(R)}{qV_c}} \tag{1.14}$$

Experimental studies by Thorson et al. [43] show that the simple model allows to reach a good agreement, in terms of order of magnitude, of the central density, that is $n_{ic} \sim 1 \cdot 10^{-15} m^{-3}$.
Finally, it is possible to calculate the effective transparency of the grid upon knowing the cathode current in the following way.
The transparency of the grid can be calculated as

$$\eta = \frac{I_{core}}{I_{grid}} = \frac{I_{grid} - I_{ion,cathode}}{I_{grid}} \tag{1.15}$$

where I_{core} is the ion current entering the core region, while I_{grid} is the current just outside the grid (approximated as a sphere in this case) and $I_{ion,cathode}$ is the component of the collected cathode current given by ions entering the material. The latter component may be calculated from the total collected current as $I_{tot}/(1+\delta)$, where δ is the average number of electrons ejected per impinging ion.
The secondary electron emission coefficient may be approximated with $\delta \sim 1$.

Alternatively, it is possible to estimate the average recirculating factor of converging ions in the device, assuming that grid transparency is actually given by the geometric estimation (as the ratio between the actual grid surface and the sphere surface). According to Hirsch [19], the ion current in the centre is equal to

$$I_{core} = \eta I_{grid} + \eta^3 I_{grid} + \eta^5 I_g rid + ... = I_{grid}\eta \sum_{n=0}^{\infty} \eta^{2n} = I_{grid}\frac{\eta}{1-\eta^2} \tag{1.16}$$

Thus the recirculating factor is

$$\xi = \frac{I_{grid}}{I_{core}} = \frac{\eta}{1-\eta^2} \tag{1.17}$$

It's possible to estimate the oscillating ion current upon knowing the total current collected by the grid using:

$$I_{core} = \frac{\eta I_{meas,tot}}{(1-\eta^2)(1+\delta)} \tag{1.18}$$

With typical values of current around $20mA$, the ion current in the core is around $\sim 100mA$.

1.4 Research question and methods

The presence of a virtual anode inside the cathode grid influences neutron production, which is the main application of fusor devices. Study of the potential structure both experimentally and via simulation is therefore an open field of research. The behaviour of the potential structure was demonstrated to depend on ion convergence and flow, so that it is not possible to treat the potential problem separately from the understanding of the whole functioning of a fusor.

The ultimate goal of this thesis is to detect the presence or absence of a virtual anode inside the cathode grid of the Tu/e fusor employing spectroscopic techniques, as already presented by other studies [22][24] [21].

As a secondary yet fundamental task, a Particle-In-Cell simulation will also try to clarify the link between the potential structure and the measured spectra.

Ion convergence, microchannel formation and characterization will also be addressed by the simulation.

The following questions summarize the aim of this thesis:

- Does a virtual anode form in the Tu/e fusor?
- What consequences does the virtual anode have on the spectrum?
- What determines virtual anode formation?

Outline of the thesis

- Chapter 1. In this chapter an introduction to inertial electrostatic ocnfinement in fusor is given. The problem of the confining potential is described alongside several computational and experimental results.
- Chapter 2. In this chapter spectroscopic characterization of plasma will be presented, particularly the application of Doppler spectroscopy. Previous spectroscopic measurements on fusors will be presented.
- Chapter 3. In this chapter the experiment will be described and results will be presented and discussed, highlighting problematic aspects of data interpretation.

- Chapter 4. In this chapter, a Particle-In-Cell simulation of the fusor will be developed. Characterization of the simulated discharge will be cariied out, according to the relevant aspects presented in Chap.1. Synthetic spectra will be obtained and compared to the experiment.

Chapter 2

Plasma spectroscopy

2.1 Broadening of spectral line

In an ideal world, the wavelength emitted by a de-exciting atom is univocally linked to the energy difference of the two states by the relation:

$$\lambda_0 = \frac{hc}{E_f - E_i} \tag{2.1}$$

However, such wavelength may vary in an interval around the central value due to natural line broadening (quantistic effect), pressure broadening or Doppler broadening [14]. In this section, results will be presented first in terms of angular frequency, as it is more easily related to energy than wavelength. Conversion in wavelength units will however be introduced.

Natural broadening is linked to the lifetime of initial and final state, due to the Heisenberg time-energy indetermination principle. The shape of the emitted spectral line in this case is Lorentzian, with width Γ_N, which is typically negligible with respect to all other effects.

Pressure broadening is difficult to link to a particular physical mechanism; however, the largest contribution is given by Stark effect caused by local electric fields produced by nearby ions. The electric field introduces an additional term in the hamiltonian describing the atom, perturbing the original state and modifying its energy: variation in state energy causes in turn different wavelength of the emitted photon when the atom de-excites.

Also interactions with neutrals can be relevant, due to long-range Van der Waals interaction or dipole-dipole interaction.

A traditional classification of pressure broadening is provided by the different mathematical approaches used to model it. Among the considered approximation, the one providing an easy analytical expression for line profile is the Lorentz impact approximation for single lines; according to such treating the shape of the line is Lorentzian.

Since correlation of the line width to pressure is heavily dependent on plasma composition, estimation of the exact broadening is not attempted. Rather, experimental studies demonstrated that pressure broadening is relevant for plasma density higher than $\sim 10^{16} cm^{-3}$ [13], which is six orders of magnitude higher than the density in the fusor.

Finally, what is expected to be the most relevant broadening mechanism with the operation parameters used in this thesis is Doppler shift broadening. The wavelength of the radiation emitted after de-excitation is fixed by the energy difference between the initial and final energy state of the excited electron; if, however, the emitter is moving with a velocity $\vec{v}$ in the reference frame of the observer, then the recorded wavelength will be :

$$\lambda = \lambda_0 \left(1 + \frac{\vec{v} \cdot \hat{l}}{c}\right) \tag{2.2}$$

where $\hat{l}$ is the unit vector describing the direction of the line connecting the emitter to the observer. Now, in the real world, the chamber will be populated with many particles, with many different velocities, depending on the temperature, following a distribution given by the Maxwell-Boltzmann distribution:

$$f_{MB}(v) = 4\pi \left(\frac{m}{2\pi k_B T} \right)^{3/2} v^2 e^{-\frac{mv^2}{2k_B T}} \tag{2.3}$$

assuming they are actually moving in random directions (so that ϕ_0 is distributed with a uniform distribution). The emission peak resulting from particles with velocities distributed according to Eq. 2.3, will be a gaussian peaked at λ_0 and with a full width at half maximum proportional to the temperature according to:

$$\Delta\lambda_{FWHM} = \frac{\lambda_0}{c} \sqrt{\frac{2k_B T}{m}} \tag{2.4}$$

So far, observing a Doppler shift in the optical spectrum leads to knowledge of a particle's velocity and direction of motion (hence, also whether it is diverging or converging). The general treating of Doppler broadening will be limited to this, while detailed effect of fast directioned emitter motion will be treated later.

2.2 H$_\alpha$ emission

Balmer α line is the most intense emission line of atomic hydrogen, with $\lambda = 656.3nm$. The emission of a photon is caused by a transition of the hydrogen only electron from a higher energy state (3s,3p or 3d) to a lower energy state (2s). Since three possible transitions contribute to the H_α line, it is necessary to specify that slightly different wave length are associated with such transition, specifically $656.272nm$ (3s→2s), $656.279nm$ (3p→2s) and $656.285nm$ (3d→2s); sensitivity of the spectrometer does not allow to resolve the difference between such transitions, they will therefore never be mentioned separately from now on.

The three possible transitions have a radiative lifetime of $160ns$ and $44.5ns$ and $15.5ns$ respectively [33].

2.2.1 Emission from background gas

Balmer α emission from the background gas is caused by dissociative excitation of background molecular hydrogen. Dissociative excitation may be caused by collisions of electrons, H^+, fast H and H_2^+.

Fig.2.1 shows the cross sections for impact dissociative excitation of background gas causing emission of a photon at $\lambda = 656.3nm$. The dominant process at low energies is electron-impact excitation, while ions and neutrals are relevant at higher energies. The excitation to the three different levels listed before is not distinguished by the presented cross sections, which represent therefore the total contribution.

Previous studies have identified electron impact dissociative excitation as the most relevant process in creating low energy excited H atoms [3]; this observation will be confirmed by the simulation in Sec.4.

Production of an excited H follows the following paths:

$$\begin{gathered} e + H_2 \to e + H_2^* \to e + H^* + H \\ e + H_2 \to 2e + H_2^+ \to 2e + H^* + H^+ \end{gathered} \tag{2.5}$$

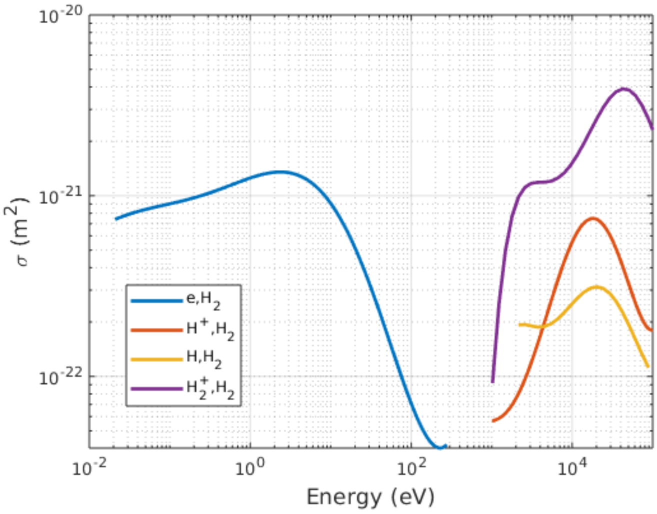

Figure 2.1: Cross section of target excitation due to impact of different species with background gas.

The first reaction produces an intermediate state with an excited hydrogen molecule. The unbound excited state which is formed at a potential energy of 30eV; in the case of dissociation to $H(1s) + H(3p)$, 16.5eV of such energy are required by the dissociative process, while the remaining energy is divided equally among the fragments, leaving with excited H with an average kinetic energy of 6eV, which corresponds to a Doppler shift of roughly 0.1nm.
Similarly, the second reaction may also produce excited neutrals with energies between 5 and 8eV.

It must be specified that since $3p$ electrons de-excite to the ground state with a branching ratio of 88%, most of the H_α radiation comes from electrons excited to $3s$ and $3d$ states.

2.2.2 Emission from fast neutrals

Fast excited neutrals are produced by selective state charge exchange or by excitation of fast H projectile:

$$\begin{array}{ll} H^+ + H_2 \rightarrow H* + H_2^+ & (1) \\ H_2^+ + H_2 \rightarrow H* + H + H_2^+ & (2) \\ H_3^+ + H_2 \rightarrow H* + H_2 + H_2^+ & (3) \end{array} \tag{2.6}$$

The kinetic energy of the parent ion is equally divided among its fragments, therefore H^* born from H_2^+ or H_3^+ will receive respectively half and one third of the parent ion energy; since however, their mass is respectively half and one third of the parent ion, their velocity is equal. The direction of the motion of the excited neutrals is considered to be the same of the impinging ion [28].
It must also be considered that H^+ , H_2^+ and H_3^+ ions are accelerated by the same potential, therefore reaching the same kinetic energy, which means that, due to the different mass, the velocity of the last mentioned species will be $1/\sqrt{2}$ and $1/\sqrt{3}$ of the velocity of H^+.
Combining all together, if all ions are born in the same position, we would expect to obtain 3 peaks shifted with respect to the central peak of the quantity $\Delta\lambda_{H^+}$, $\Delta\lambda_{H_2^+}$ and $\Delta\lambda_{H_3^+}$ such that:

$$\Delta\lambda_{H^+} = \sqrt{2}\Delta\lambda_{H_2^+} = \sqrt{3}\Delta\lambda_{H_3^+}$$

The cross sections of such reactions are in Fig.2.2 and they are all comparable.
Also in this case there is no distinction between the three possible excited states.

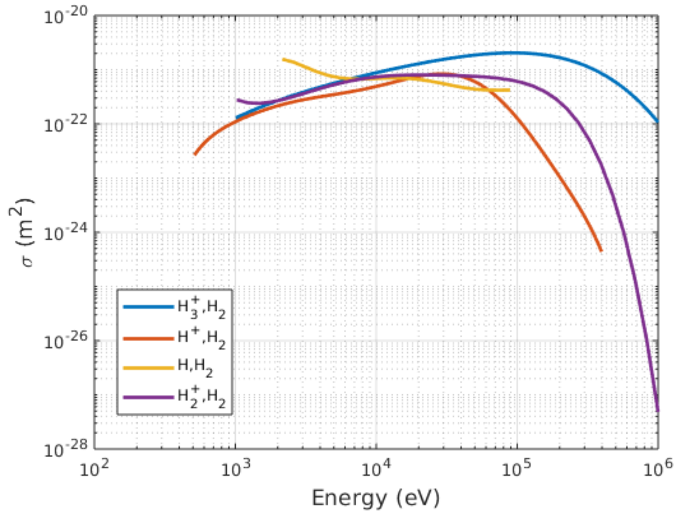

Figure 2.2: Cross sections for projectile excitation due to either charge exchange or excitation of H projectiles.

When measuring fast neutrals at a point in space, one must consider that such particles may have travelled before de-exciting. In the present case, considering an average kinetic energy of $2keV$ (which is taken from the following sections providing experimental results), an excited hydrogen atom may travel 20cm (3s), 2cm (3p) or 1cm (3d). If the aim is to link the information about neutral kinetic energy given by the spectra to the potential shape confining the ions, it must also be considered that the information given may be delayed by as much as 20cm.
On the other hand, as only part of the radiation comes from de-excitation from $3s$ state, it is expected that most of the contribution is given by neutrals formed close by.
The exact shape of the shoulders depends on both the direction along which particles are moving and their energy. In order to understand how both variables interact to create a given spectrum, let us consider a particle moving on a plane, therefore with null z component of velocity and let us consider the line of sight correspondent to the x-axis of such plane. The projection of the velocity along the line of sight will therefore be its x component.
First of all, let us consider a monoenergetic population of particles, moving isotropically in any direction; the resulting spectra is shown in Fig.2.3a. In order to build such spectrum, velocity was calculated from the fixed value of kinetic energy, while the angle was extracted from a uniform distribution.
The spectra display clear peaks correspondent to values symmetrically arranged around $\phi = 0$, which shift with change in energy. The shape of the spectra is due to the fact that even if the angle is extracted from a uniform distribution, the correspondent distribution of the cosine value is peaked around $cos(\phi) = 1$.
Fig.2.3b shows the effect of limiting the angle between 0 and 30°. As expected, the central part of the spectrum is no longer present.

Consider now particles with a uniform energy distribution; again, z component is set to 0, as we consider particles moving on a plane. Fig.2.4a shows how the spectrum would look like if particles with uniformly distributed energy moved isotropically, while Fig.2.4b shows the same spectra obtained assuming the direction of motion is limited to the interval $[0, 30°]$, while finally, Fig.2.4c shows the effect of the direction being distributed as a gaussian peaked at 45° with different standard deviations. The general trend shows that the less spread is the angle, the more the spectrum resembles velocity distribution (which is linear, if energy distribution is uniform.

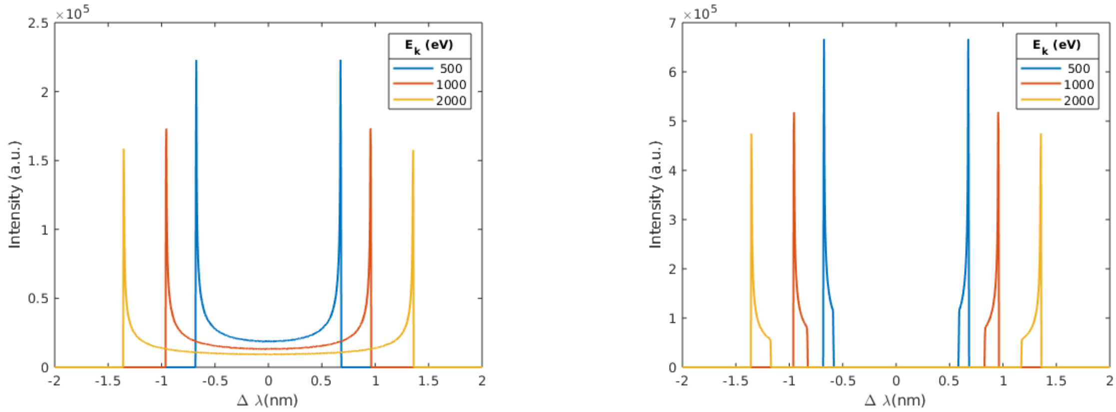

(a) Isotropic motion.

(b) Limited angle.

Figure 2.3: Spectra resulting from monoenergetic particles.

Adding gaussian spread to the angle distribution changes the shape of the tails.

A fixed value of the angle between the line of sight and the direction of motion would allow to know exactly the velocity distribution just by looking at the spectrum; however, in the very likely event of collecting light produced by particles moving in directions forming different angles with the line of sight, the spectrum conserves information about particle velocity distribution. Considering with care angular distribution is fundamental in order to convert correctly the value of $\Delta\lambda$ into the kinetic energy that is interesting in the present work. If the angular distribution is uniform, the peak shows up at $cos(\phi) = 1$, while in the other extreme case of fixed angle, the conversion must be done considering the specific angle. If the angle is selected from a fixed interval, then the peak shows up at the position correspondent to the highest value of the cosine, as shown in Fig.2.5 , where energy was extracted from a gaussian-like distribution peaked at 2keV. The dashed black curve represents the spectrum of isotropic particles. The experiment described in the thesis will exploit the star-mode regime of the fusor in order to produce radiation coming mostly from the microchannels, which have defined direction. Radiation from the background gas will be collected too, but will represent a minor contribution. Whether or not the collected signal is coming from a microchannel will be carefully investigated.

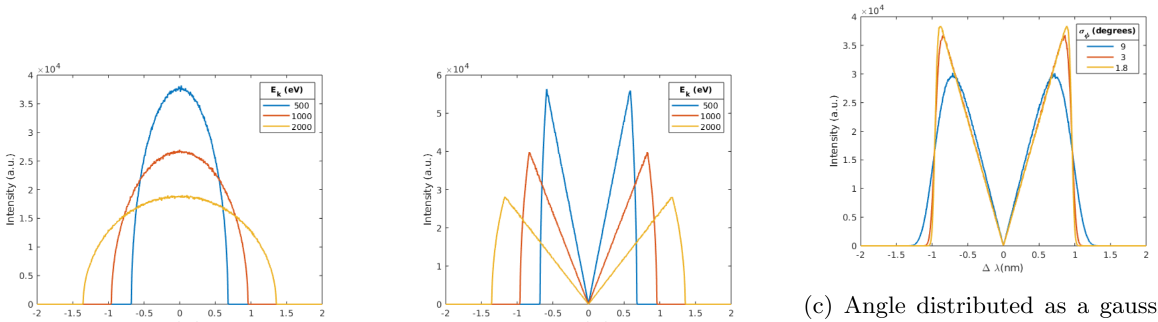

(a) Isotropic motion.

(b) Limited angle.

(c) Angle distributed as a gaussian (in this case σ of the distribution is varied).

Figure 2.4: Spectra resulting from particles having energy uniformly distributed.

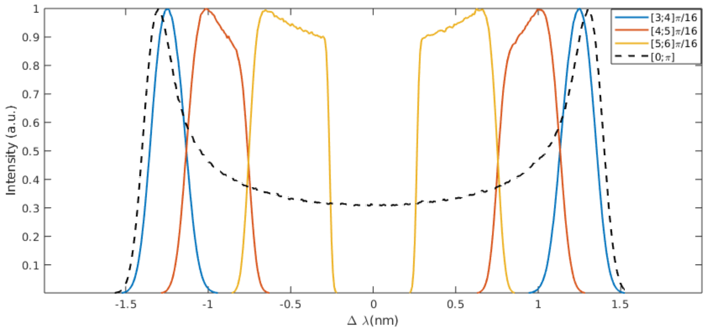

Figure 2.5: Transformation of the spectrum when changing angle interval.

2.3 Spectroscopy in an IEC device

Previous experiments conducted in order to characterize spectroscopically a spherical IEC device will be presented in this section.

2.3.1 Collisional radiative modelling

Collisional radiative models consist in writing down all the equations describing temporal evolution of a certain specie i evolution as follows:

$$\frac{dn_i(t)}{dt} = \sum_{j \neq i} (A_{ij} n_i + B_{ji} n_j + C_{ij} n_i n_j) \tag{2.7}$$

where the first two terms describe respectively de-excitation through spontaneous emission to any available state j or excitation to the state i from any state j, while the third term takes into account particle-particle reactions which might create the desired species. The summation is over a generic index j,which may be referring to an atom in a different excited state or to a different species.

A and B are Einstein coefficient, measuring the frequency of de-excitation and excitation, while C is expressed in units of $m^3 s^{-1}$ and is the reactivity of the selected reaction.

CR models are connected to radiation intensity through the relation $I_{i,j} \propto \nu_i A_{i,j} n_i$.

This model was applied in [25] to correlate the intensity of H_α produced by dissociative excitation induced by a monoenergetic electron beam to the energy of such electrons and was extended to the determination of fast ion energy ratios as described in the following [22, 26].

The equilibrium density of fast neutrals in the vessel is given by setting to zero $\frac{dn^*(n=3)}{dt}$:

$$\frac{dn_x^*(n,l)}{dt} = n_x^+ n_{bg} k_x - \sum_{(n,l)\rightarrow(n',l')} A_{(n,l)\rightarrow(n',l')} n_x^*(n,l) \tag{2.8}$$

where $x = 1, 2, 3$ according to which ion created the fast neutral, k is the charge exchange rate coefficient. The first term of Eq.2.8 represents the birth term of fast excited neutrals, while the second represents their death due to de-excitation (the sum runs over all possible final states). In the case of H_α emission, the starting state is $n = 3$, while final state may be either $i = 2$ or $i = 1$.

Imposing the steady state condition one finds that:

$$n_{H_x^+} = \frac{\sum_{n'=1}^{2} A_{3\rightarrow n'} n_x^*(n,l)}{n_{bg} k_x} \tag{2.9}$$

the H_α radiation intensity coming from such neutrals can be written as:

$$I_{H_x^+} = n_x^*(n=3)A_{n=3\rightarrow n=2}h\nu \tag{2.10}$$

Using Eq.2.10 to determine $n_x^*(n=3)$ and inserting it back into Eq.2.9 yields:

$$n_{H_x^+} = \frac{\sum_{n'=1}^{2} A_{3\rightarrow n'} I_{H_x^+}}{h\nu n_{bg} k_x} \tag{2.11}$$

If we wish to know only population fractions, density of H^+ can be taken as a reference, therefore:

$$\frac{n_{H_x^+}}{n_{H^+}} = \frac{k_1}{k_x}\frac{I_{H_x^+}}{I_{H^+}} \tag{2.12}$$

Now the difficulty is represented by the charge exchange rate coefficient, as it is defined as $k = \int dv'\sigma(v')f(v')v'$, v' being the relative velocity of the two colliding particles. Knowledge of ion velocity distribution is therefore required to solve the equation. Such information can be extracted by the PIC simulation carried out in Chap.4, but cannot be derived beforehand.
Considering a typical Doppler-shifted peak obtained from a fusor discharge. The contribution given by fast neutrals is contained in the blue-shifted shoulder. We can consider, as a first approximation, that such contribution has a gaussian, therefore yielding a peaked velocity distribution, as discussed above. As a first approximation, since it is not possible to deconvolve angular and velocity distribution, one can consider the ions as monoenergetic, having the velocity associated with the considered shifted peak, therefore:

$$\frac{n_{H_x^+}}{n_{H^+}} = \frac{\sigma_{cx,1}(v_1)v_1}{\sigma_{cx,x}(v_x)v_x}\frac{I_{H_x^+}}{I_{H^+}} \tag{2.13}$$

2.3.2 Fast ion motion

Kachan and Collins [22] conducted spectroscopic measurements on a spherical IEC device with an inner gridded cathode and a gridded external anode, thus producing converging ion motion and diverging electron motion. Fig. 2.6 from the study shows the shape of the spectra inside the cathode grid and their evolution as the applied voltage is increased. With the necessity of collecting light only from a selected channel, a second cathode with a double ring was employed. This allowed measurement of clearer peaks,such as the ones shown in Fig.2.8 and also deriving ion population, shown in Fig.2.7.

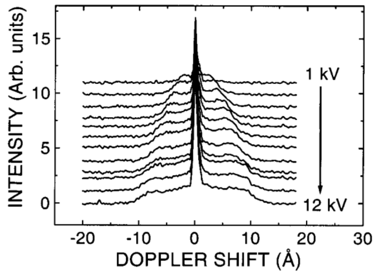

Figure 2.6: Changes in the spectrum as the applied voltage is increased. Figure taken from [22].

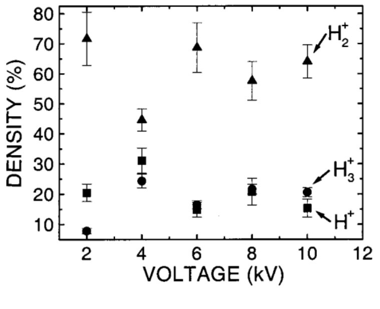

Figure 2.7: Fast ion population calculated from intensity of the detected shoulders. Figure taken from [22].

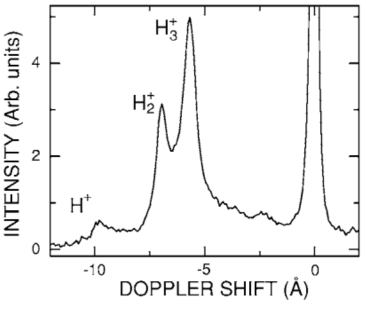

Figure 2.8: Shape of the shoulder detected along the channel. Figure taken from [22].

although the possibility of detecting shifts due to potential change was established, the study

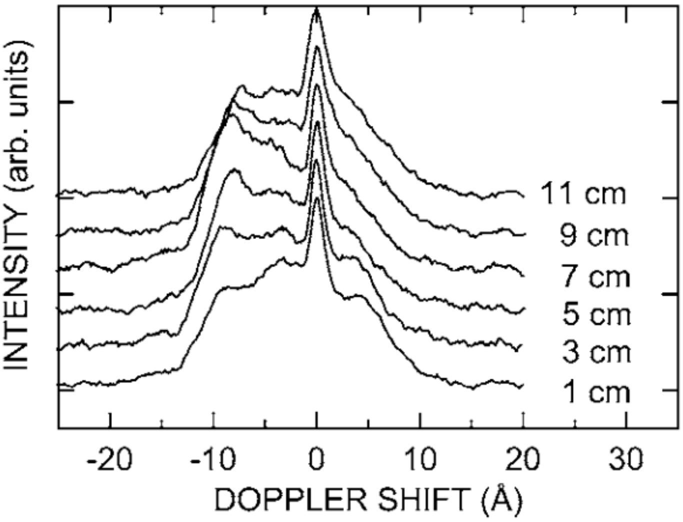

Figure 2.9: Evolution of the spectrum as the line of sight is moved further away from the cathode. Picture taken from [36] .

did not shed any light on the ion behaviour outside the cathode grid.

Shrier et al. developed a biconical cathode, capable of better focusing the radiating channel and were able to perform measurements at different distances from the centre [36]. The evolution of the spectrum as the line of sight is moved further from the cathode is shown in Fig.2.9.

It was observed that the most prominent feature of the spectra is the blue-shifted component. Reason for such predominance was sought in different mechanism. It seemed natural to first assume that such emitting neutrals were in fact formed on the other side of the cathode and then crossed undisturbed the central region in order to emit only after reaching the other side. If this were the case, then the only transition that could reasonably be responsible for the emission is the $3s - 2s$ one, which is the slowest one. However, this would mean that the intensity of the blue shifted side would decrease exponentially from the centre, while the opposite was observed. The possibility that such neutrals were formed in the centre was discarded, because this explanations would lead to a uniform measured kinetic energy of neutrals, while a sharp increase upon crossing the cathode grid was detected.

Since neutrals are born neither on the other side, nor in the centre, they must be born somewhere between the centre and the line of sight. The contribution cannot come from oscillating ions, as, if this were the case, a symmetric or at most a more red-shifted spectrum would be expected.

Value of estimated ion kinetic energy is shown in Fig.2.10 [21].

An interpretation of such behaviour is given by the Abnormal Hollow Cathode model [24]. The idea is that the fast excited neutrals are actually born from ions moving from the central region of the cathode, rolling off a virtual anode (potential hill inside that cathode, formed due to space charge accumulation) and undergo charge exchange.

Such ions are the ones born in the centre from electron-impact ionization. Since electrons are actually moving towards the outer anode the question of how they could manage to get inside the cathode at energy high enough to cause consistent ionization arises. The answer is given by the model considering the electrons which are emitted from cathode grid wires as they are hit by falling ions. The peculiar name of the model is given in analogy with the Hollow Cathode effect, where electrons emitted from the cathode surface oscillate within the electrode causing enhanced ionization; it was established [40] that the electric field within such electrode is directed towards its surface, as it seems to be the case of the present results.

Weaknesses of the model are related to the long electron-impact ionization mean free path at

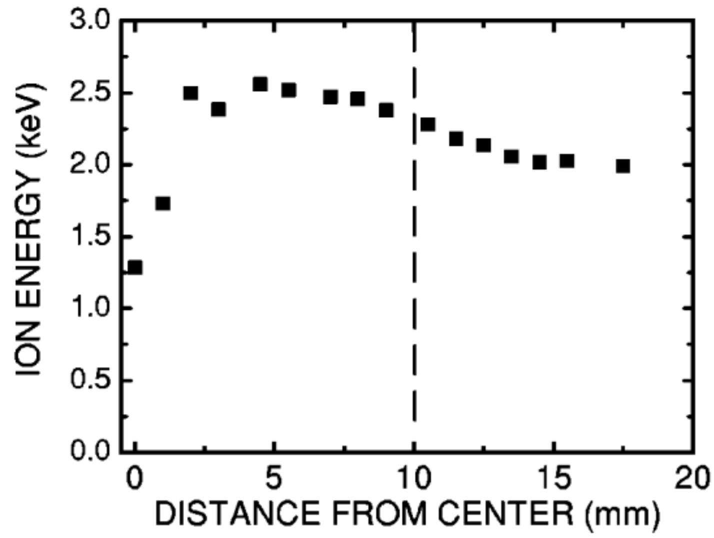

Figure 2.10: Estimated kinetic energy from the acquired spectra. Figure taken from [21].

the operating parameters, which is greater than the cathode dimension. Whether or not such reactions are relevant should be investigated.

Moreover, the region of space where diverging ions may undergo charge exchange is small and many of them may actually decelerate before producing a fast excited neutral.

2.4 Summary

In this chapter spectroscopic techniques applied to plasmas were introduced, with a particular emphasis on the detection of velocity distribution of fast ions via Doppler spectroscopy.

Various possible causes of line broadening were presented, concluding that the most relevant in the considered case is temperature broadening, if buried inside instrumental broadening.

Main reactions producing fast and slow excited H atoms were introduced, as well as the different possible excited states occupied by hydrogen only electrons, concentrating on their effect on spectral measurements.

Assuming different energy distributions and angular distributions of particles, different spectral shapes were obtained. Spectra resemble the velocity distribution stemming from the imposed energy distribution. Angular distribution (rather $cos(\theta)$ distribution) modifies the tails and generally the peak shape, though no peak can be present if no peak is present in the velocity distribution, unless particle are moving along a very sharply defined direction, which is not true in our experiment, despite the effort of shutting background radiation out.

Finally, a technique previously employed to determine discharge composition was presented , as well as experimental results showing expected peak shapes and their evolution.

Chapter 3

Experiment

The more basic goal of the experiment was designed is to collect data that can prove the presence of a virtual anode inside the cathode grid of the fusor.
The presence of a virtual anode would entail particles moving from the center of the grid outwards (diverging) and from the anode inwards (converging).
If it were possible to isolate only one direction of motion, such task would be much easier. This can be done by exploiting the fusor star-mode and the formation of microchannels along which ions preferentially move and therefore are excited, ionized, undergo charge-exchange.
If it is not feasible to observe directly the emission from excited ions, it's still possible to observe emission from ions that undergo charge-exchange and ultimately get de-excited. Since they are neutrals atoms and are not affected by the potential, they conserve the information on "how much" the parent ion was accelerated. How to link such information to the structure of the potential will be further investigated in Chap.4.
Observing how the spectrum behaves in different positions along a microchannel might disclose interesting information on the structure of the potential in the chamber.
We therefore come to the conclusion that what we require from our experimental setup is :

1. capability of recording optical spectrum;
2. capability of moving the line of sight;
3. capability of doing the above tasks in a reproducible way.

3.1 Experimental apparatus

The experimental apparatus is represented in Fig.3.1.

3.1.1 Anode and cathode

The anode of the fusor is the outer wall of the vessel. The spherical vessel is made of stainless steel and has a 20 cm radius. It presents a total of 4 accessible ports for diagnostics, two ports used for gas supply and removal and one port which can be used for installing an ion source.
The cathode is inserted inside the chamber from a port at the top of the spherical vessel; it is attached to a stalk shielded by an insulator. The connection is made mechanically, thanks to small hook-shaped holes built on the stalk itself.
The cathode grid is built using point-welding technique with titanium wires, with a diameter of 0.007mm. Other materials, like tungsten or nickel, proved in the past to be very hard to weld in a symmetric shape.
Moreover, titanium offers a lower sputtering yield than stainless steel, which was also proposed

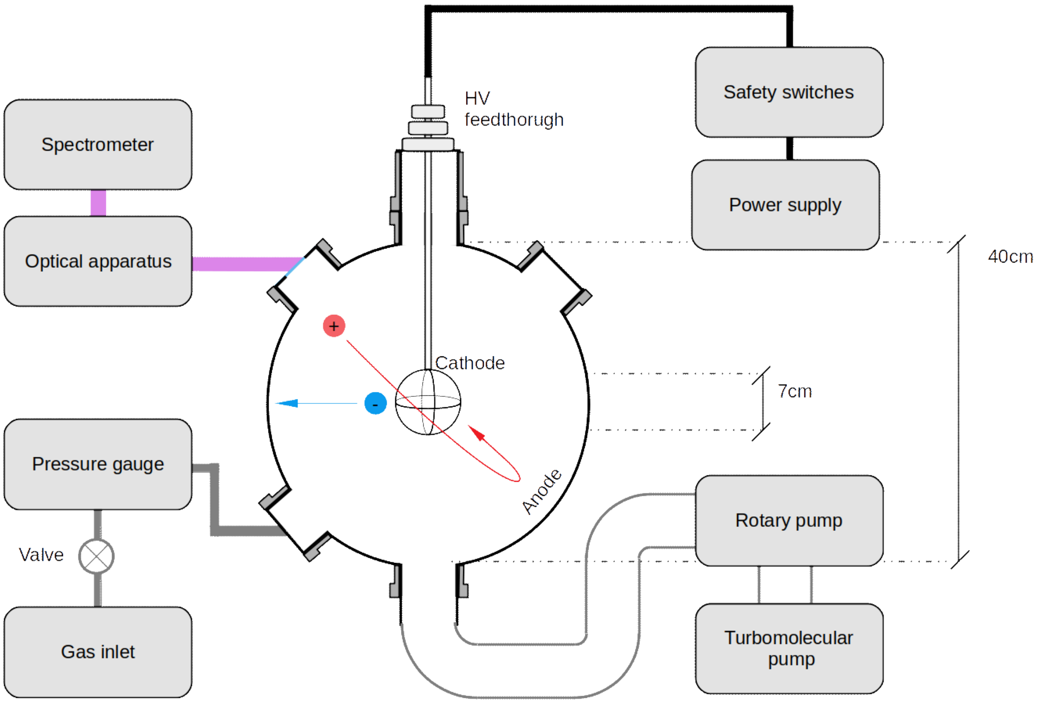

Figure 3.1: Experimental apparatus

as a constructing material. This is shown by Fig.3.3.
The grid has a diameter of 7cm; the geometry with three rings was suggested in order to be able to observe only one micro-channel at a time, as the previous grid, with 16 openings, could not guarantee that. Moreover, previous experiments have proven such geometry to be successful in micro-channel creation.

3.1.2 Power supply

The Heinzinger HNCs DC power supply is connected to the cathode via the stalk; such power supply can provide up to 120kV with 100mA current.
Due to high voltage safety requirements, the fusor is separated from the operating unit by a fence. Several switches must be closed in order for the power supply to be turned on. Firstly, on switch is positioned on a metal hook in front of the fence gate: in order to close it, a metal stalk must be positioned on it, so that the gate is impossible to open. Secondly, a switch must be activated to open a metallic hammer and lastly, another switch activates the actual power supply.
During the experimental campaign the switch activating the metallic hammer failed, requiring the substitution of a PCB.

3.1.3 Pressure control

The gas pressure control in the vessel is obtained using a combination of pressure gauges and valves.
Gas is let inside the chamber through the line highlighted in Fig.3.2b . Connected in parallel to the gas-inlet is a Pfeiffer IMR 265 process ion gauge which operates a Pirani and a hot-cathode detector depending on the pressure range. The hot cathode pressure gauge is automatically used for pressure below $0.05 mbar$ (5 Pa). Therefore, it is possible to know gas pressure just before it

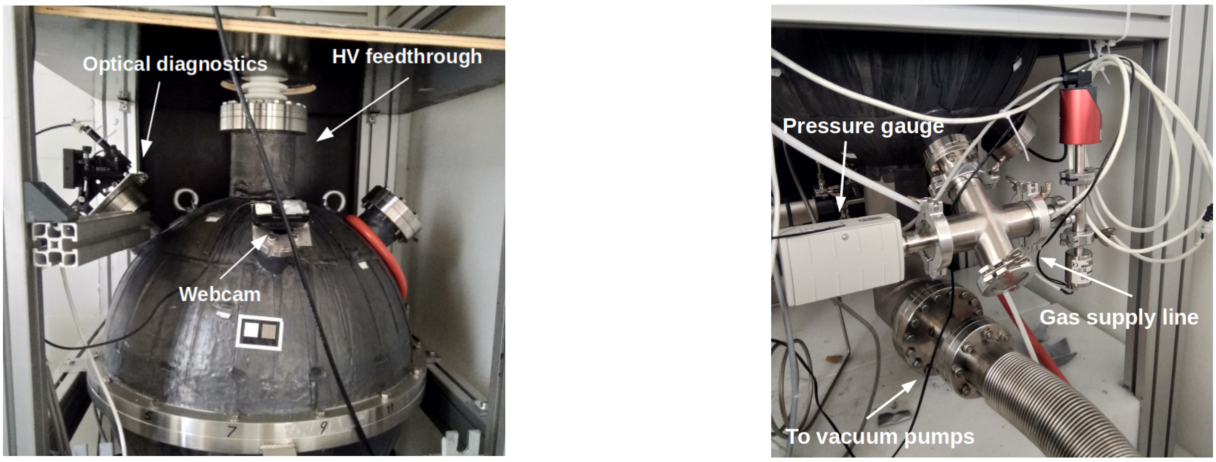

(a) Upper part of the sphere.

(b) Lower part of the sphere.

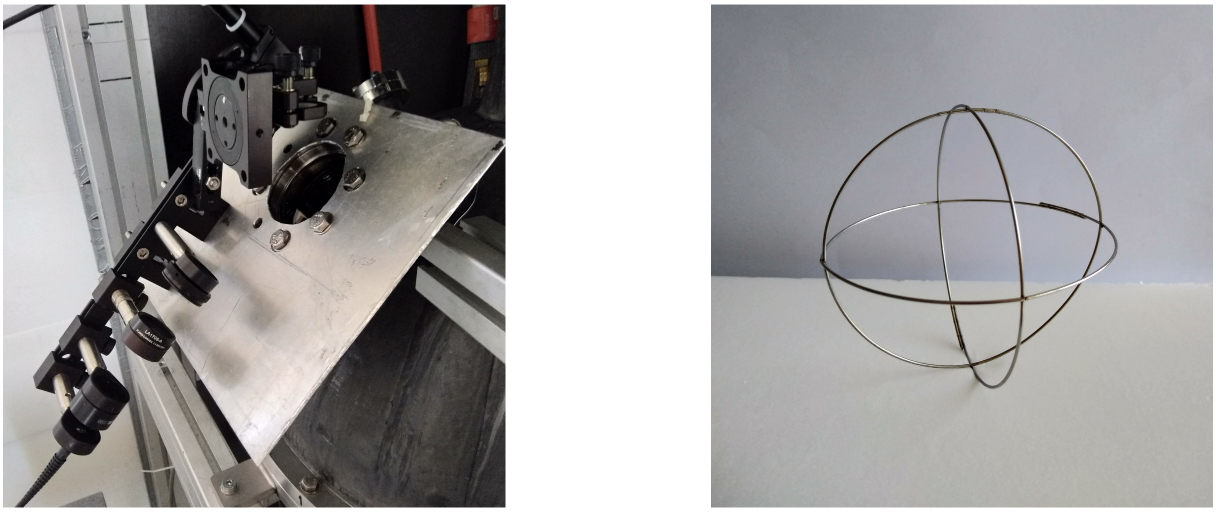

(c) Optical diagnostics.

(d) Cathode grid.

Figure 3.2: Real pictures of the experimental apparatus.

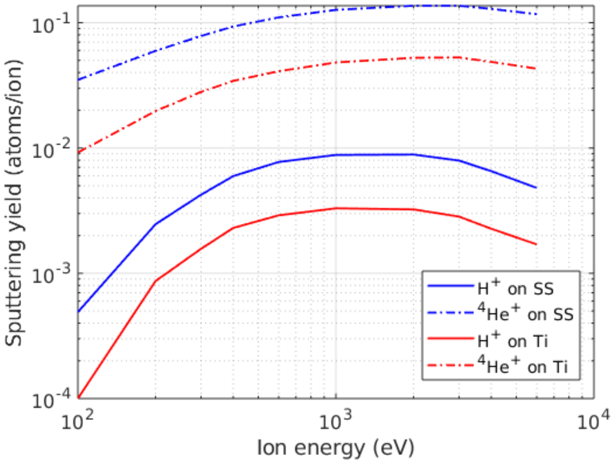

Figure 3.3: Sputtering yield of H^+ and $^4He^+$ on Titanium and Stainless Steel [27].

enters the vessel; this cannot provide an accurate value of the actual pressure in the vessel, but guarantees reproducibilty of the measurements.

The valve letting the gas in is regulated by a Pfeiffer IMR300 control unit, which reads the pressure measurements from the aforementioned gauge and regulates the opening of the valve consequently. The controller allows both manual and remote control. In the first case, a switch can be used to manually close or open the valve. In the latter case, the switch is positioned in the central position and the controller receives as an input the pressure value selected on a Matlab GUI, which also shows the measured pressure, the applied voltage and the current.
The gas is pumped out using a combination of a rotary pump and a Pfeiffer HiSpace 80 turbo pump, connected to the lower end of the vessel, as shown in Fig.3.2b.

3.1.4 Optical diagnostics

In order to measure the spectrum of the radiation emitted from the fusor,an Andor Shamrock 500i spectrometer was used.
Such spectrometer offers the possibility of choosing among three different gratings, with different resolutions. For the detailed spectra presented in this work a 1200 lines/mm was employed, with nominal resolution of 0.06nm. The slit opening was kept constant at 15μm. The signal reached the spectrometer aperture following the optical path shown in Fig.3.4. The lens-system is built to collimate the light coming from the desired spot inside the fusor and focus it on the optical fiber opening. The optical fiber that was used had a numerical aperture of 0.39, allowing light with an incidence angle of maximum $\sim 20°$ to be collected.

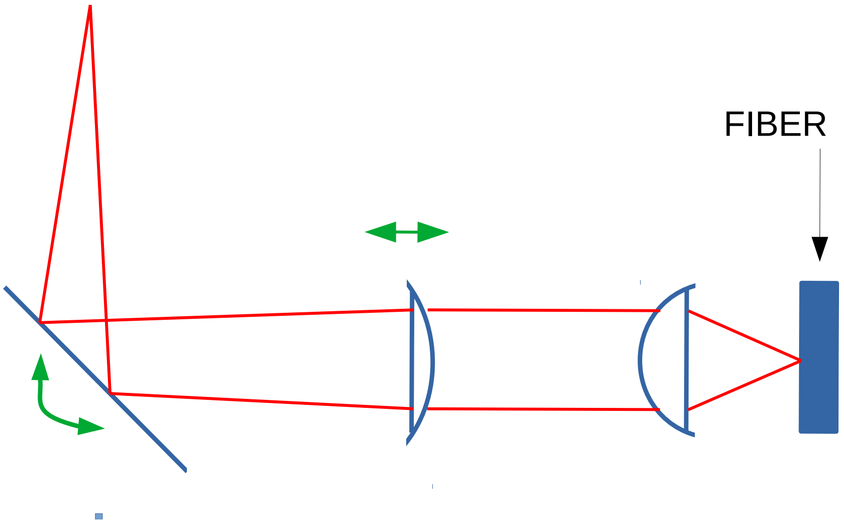

Figure 3.4: Optical path followed by the light exiting from the chamber.

In order to calibrate the spectrometer, a full spectrum of an He lamp was measured and the characteristic peaks of Helium were recognised. The calibrated spectrum is shown in Fig.3.7

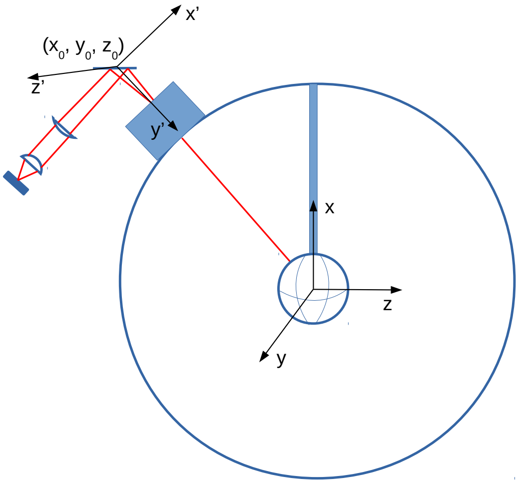

Figure 3.5: Sketch of the fusor and the optical apparatus.

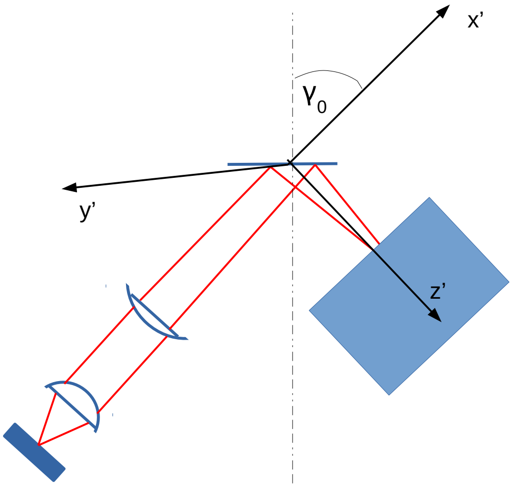

Figure 3.6: Close up on the optical system to clarify the selected reference frame.

The movement of the line of sight depends on the position of the mirror, so particular attention was devoted to improve the motion of such component.

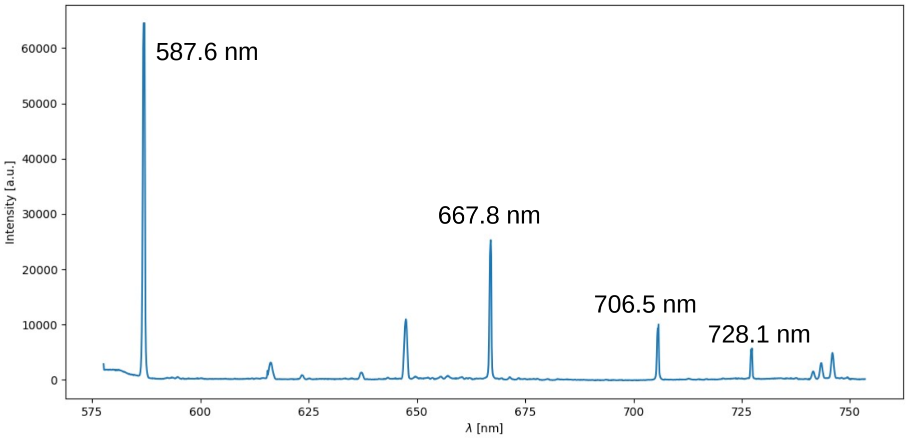

Figure 3.7: Helium spectrum used for calibration.

A manual rotating stage and a motorized rotating stage were combined in order to provide control on both of the mirror rotating angles.

The manual rotating stage provides a resolution of 1° on its rotation; the automated rotating stage is controlled by means of a software which guarantees reproducible movements only for motion greater than 0.3°.

In order to evaluate the spectral broadening introduced by the optical apparatus, a $656nm$ laser was pointed at the mirror, in order to follow the same optical path as the radiation from the fusor, and the corresponding spectrum was acquired.

Fig.3.8 shows the spectrum broadened by the optical apparatus. The full width at half maximum is equal to $(0.16 \pm 0.02)nm$. Both a gaussian and a lorentzian curve was fit to the acquired data. Both fitting curves exhibit issues in the modelling of the tails.

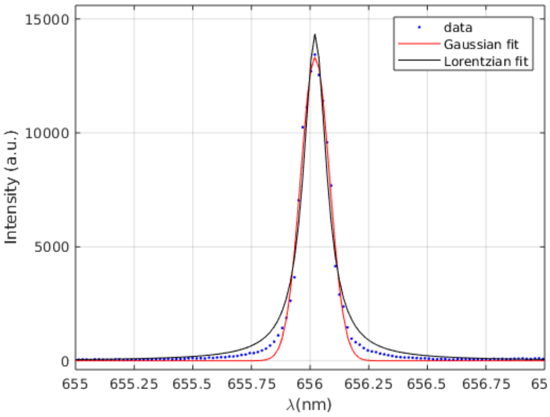

Figure 3.8: Peak broadened due to instrumental broadening.

3.1.5 Calibration of the moving system

Motion of the line of sight is obtained using a mirror attached to two circular rotating gears. Calibration of the system requires to convert angular position of the gears to line of sight inside the vacuum chamber. In order to do that it was necessary to highlight visually the light path from the optical fiber to the inside of the machine; for such purpose a red laser beam was shone through an optical fiber attached to the slit holding the spectrometer optical fiber.
Motion of the mirror by means of the two gears revealed that the motion was not perfectly cardanic, that is, the mirror did not rotate exactly around its axis and the laser spot was not perfectly centered on it. Restrain on apparatus geometry prevented perfect alignment with the mirror. This means that it is not straightforward to convert rotating angle to line of sight position; if the system was perfectly cardanic and aligned, it would have been possible to build a spherical frame of reference centered on the mirror and derive line of sight direction only by measuring the two angles. We will call ϕ the angle determined by the manual gear, while θ will be the one determined by the motorized rotating stage.
In absence of the necessary assumptions to build a spherical reference frame, a different approach was used. In particular, two cartesian reference frames were considered: one centered on the centre of the cathode grid, having the x direction along the stalk, and the other two directions as shown in Fig.3.5, and the second centered on the mirror and having x axis parallel to the metal support sustaining the optical apparatus, with z axis rotated accordingly, as shown in Fig.3.6.
The procedure consists in positioning the mirror at known angles and marking on a rigid support, parallel to the metallic support of the optical apparatus, the position of the laser beam spot; if the projection of the $x = 0, y = 0$ point is found on the rigid support, then every point will have known coordinates with the respect to the mirror reference system. Drawing the line that connects the mirror with the marked point and converting it to the frame of reference of the grid, will allow us to draw the line of sight inside the vessel. In order to do so the following steps must be taken.

1) Measure the position of the mirror with respect to the center of the vessel; in our case its coordinates are $(32, -26, 0)cm$.

2) Measure the angle formed by the metal support with the vertical; in our case $\gamma_0 = 46°$.

3) Position a rigid support on the metallic support. Calling (x',y',z') the coordinates of the mirror reference system, determine the y'=0 line by choosing a fixed value of ϕ rotating θ: if a sweep in theta draws a perfectly straight line, $y' = 0$ is found.

4) By keeping the $y' = 0$ position, choose some reference points on the inside of the chamber (in our case they were: lower end of the stalk, half of the frontal ring and bottom of the grid), point the laser at them and mark their position on the rigid support.

5) Rotate the two gears at significant positions that will be used for the measurements and mark the points as well.

In order to calculate the $x' = 0$ axis on the rigid support, consider the coordinates of the highlighted points in the grid reference frame, the lower part of the stalk is $(4, 0, 0)$, the second point is $(0, 0, 0)$, the bottom of the gird is $(-4, 0, 0)$; such coordinates were converted in the mirror reference frame as:

$$\begin{cases} x'_p & = (x - x_0)cos(\gamma_0) + (z - z_0)sin(\gamma_0) \\ y'_p & = 0 \\ z'_p & = -(x - x_0)sin(\gamma_0) + (z - z_0)cos(\gamma_0) \end{cases} \tag{3.1}$$

where (x_0, y_0, z_0) are the coordinates of the mirror.
Now it is possible to calculate the line connecting the mirror to the point and calculate the position of the intersection with the rigid support in the mirror reference system, simply by calculating:

$$\begin{cases} x'_i & = \frac{x'_p}{z'_p} d \\ y'_i & = 0 \\ z'_i & = d \end{cases} \tag{3.2}$$

where d is the distance of the rigid support from the mirror.
Finally, $x' = 0$ can be found by considering the point marked on the support and moving of the quantity $-x'_i$.
Using the coordinates of the marked point and the position of the mirror the line crossing both points can be calculated in the mirror reference frame and then converted in grid coordinates using the inverse of the transformation described by Eq.3.1. This method can give an idea of what positions we are scanning; however, we must consider now what are the uncertainties in the position determination. If we assume that all fixed parameters (x_0,y_0,z_0,γ_0,d) are determined correctly and we concentrate solely on the position determined on the rigid support, we can give a very optimistic estimate of the spatial error.
Determination of the marking position suffers an error of at least $0.5mm$; the possible correct position therefore lies in a $0.5mm$ radius circle at the distance from the mirror of $3.4cm$; such spot is then enlraged as z increases, abiding:

$$r \approx \frac{0.1}{3.4} z \tag{3.3}$$

Therefore, even only after crossing the length of the port, which is $\sim 15cm$, the spot already has a $4mm$ radius, after $25cm$, the error becomes $8mm$, therefore making it impossible to determine with a higher precision the position we are scanning.
On the other hand, such calibration, correlated with the geometry of microchannels, will help interpreting the spectra.

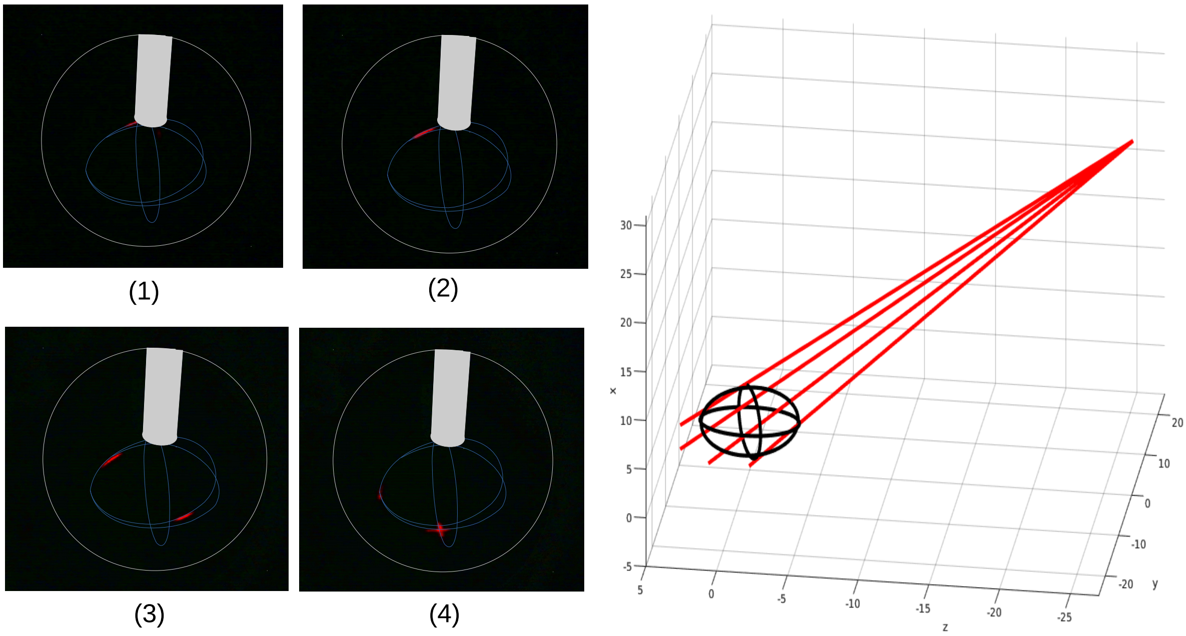
(1)
(2)
(3)
(4)

Figure 3.9: Photos of the laser signal on the grid, with the geometrical reconstruction.

3.2 Hydrogen discharges

3.2.1 Discharge carachteristics

An IEC device can work on three main operating regimes: star-mode, glow-mode or jet-mode. Since highly directioned ions are required to facilitate interpretation of Doppler spectra, the desired operating regime in our case is the star-mode operation, which was described in Chap.1 The characteristic voltage-current curves with hydrogen in the vessel are represented in Fig.3.10.

For pressure values above 1.5Pa, jet mode is visible, as it can be seen from Fig.3.11. Increase in current value causes a transformation in jet shape, changing from a defined channel to a wider burst at high currents.

Jet mode is observed also at higher pressure values; one could be interested in analyzing what

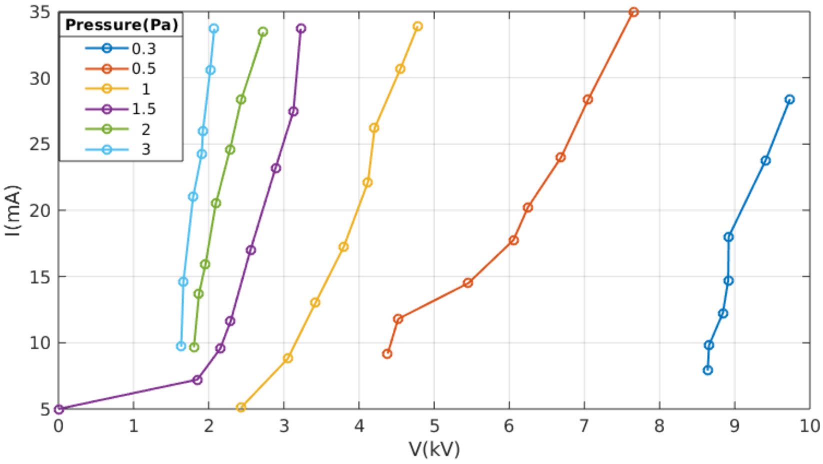

Figure 3.10: Current-voltage characteristics of Hydrogen discharges at different pressure values.

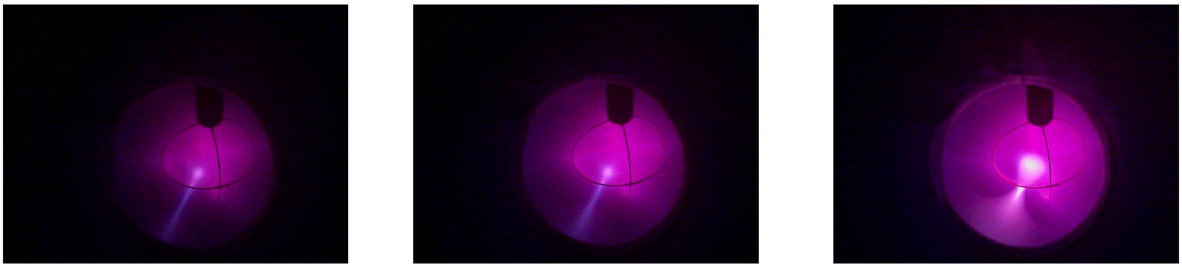

(a) 15 mA (b) 21 mA (c) 34 mA

Figure 3.11: Images of hydrogen discharges at p=3Pa.

effect causes the presence of the jet on the spectral shapes, and therefore try to align the line of sight so that it intersects the jet. However, its position depends on asymmetry in the cathode grid, which might be slightly deformed during the discharge; this causes a change in jet position. Such change can happen even if the discharge is shut down and then turned on again. This means that it would not be possible to shut off the discharge in order to reposition the line of sight,as the jet would not show up in the same position with certainty. As an example, Fig.3.12 shows two different positions of the jet at the same physical parameters. The change happened during the discharge.

Finally, Fig.3.13 shows how the discharge evolves decreasing pressure up to the star-mode operation. While p=1.5Pa does not show clear spikes and still presents a small visible jet, as the pressure is changed to 0.5Pa and 1Pa spikes passing through the grid aperture are visible. The effect of increasing current is shown in Fig.3.14; though the increase helps enhancing radiation coming from the micro-channels,it also increases cathode heating and glowing, as more ions hit its surface. For this reason at low pressure $I < 40mA$ is preferentially used.

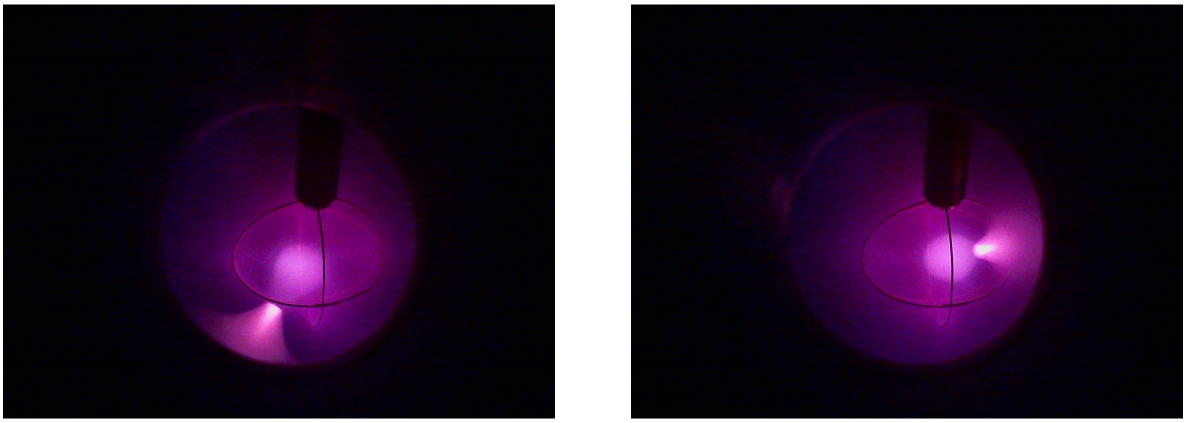

(a) Jet n.1. (b) Jet n.2.

Figure 3.12: Change in the jet position at p=4Pa, I=18mA, V=1.3kV.

During the discharge, the power supply allows choice of the current and regulates the applied voltage as a consequence. Consequently, stability of the current signal is better than stability of the applied voltage. Further investigations on the subject are necessary in order to access how much the applied voltage is oscillating in different operating conditions, as it certainty affects ion kinetic energy and therefore also the observed spectra.

Tab.3.1 shows the variance of current and voltage around the average value. For p<1.5Pa variance does not change significantly when current is increased at constant pressure; consequently, the percentage variation is lower at higher current. For p=1.5Pa, the opposite trend is detected for the value of current.

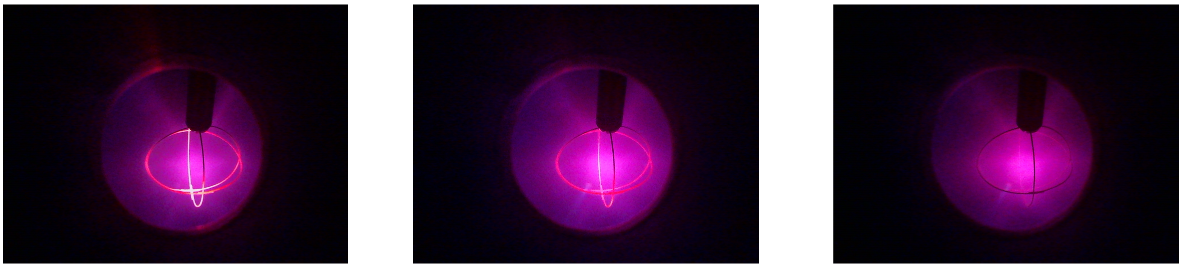

(a) p=0.5Pa, I=30mA. (b) p=1Pa, I=30mA. (c) p=1.5Pa, I=20mA.

Figure 3.13: Dischrages in star-mode at different parameters.

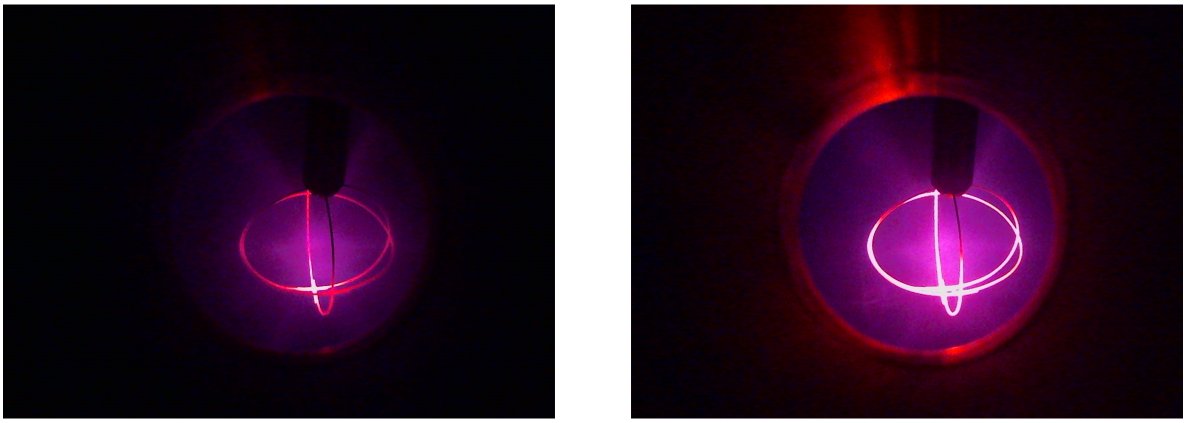

(a) 17 mA (b) 34 mA

Figure 3.14: Effect of increase of current at p=0.3Pa.

In all studied discharges the applied voltage oscillates with a maximum amplitude of $200V$. Let us suppose to detect the photon of an excited neutral with energy E_0, the detected wavelength would be:

$$\lambda_{Doppler,0} = \lambda_0 \left(1 + \frac{1}{c}\sqrt{\frac{2E_0}{m}} cos(\phi)\right) \tag{3.4}$$

if the energy is varied by a given quantity ΔE, then the new detected wavelength would be:

$$\lambda_{Doppler,1} = \lambda_0 \left(1 + \frac{1}{c}\sqrt{\frac{2(E_0+\Delta E)}{m}} cos(\phi)\right) \tag{3.5}$$

the variation in the detected wavelength can thus be written as:

$$\begin{aligned} \lambda_{Doppler,1} - \lambda_{Doppler,0} &= \lambda_0 \frac{cos(\phi)}{c}\sqrt{\frac{2E_0}{m}}\left(\sqrt{1+\frac{\Delta E}{E_0}} - 1\right) \\ &= (\lambda_{Doppler,0} - \lambda_0)\left(\sqrt{1+\frac{\Delta E}{E_0}} - 1\right) \end{aligned} \tag{3.6}$$

The first factor on the right hand side of Eq.3.6 represents the shift with respect to the central peak. As it will be clear in the following sections, such value is typically around $1nm$ for neutrals born from H_2^+ and $1.5nm$ for neutrals born from H^+. Moreover, the correspondent kinetic energy is around $3keV$.

Using this estimated value, it is possible to solve Eq.3.6 and obtain that the detected wavelength is shifted by $\sim 0.05nm$, which is anyway greater than the standard deviance of the fitting gaussian.

p Pa	**I** mA	$\sigma_{\mathbf{I}}$ mA	**V** kV	$\sigma_{\mathbf{V}}$ kV	$\%\sigma_{\mathbf{I}}$	$\%\sigma_{\mathbf{V}}$
1.50	18.37	0.09	8.3	0.2	0.50	2.25
1.50	28.1	0.2	10.2	0.1	0.80	1.33
0.50	20.2	0.2	11.4	0.2	1.14	1.32
0.50	28.1	0.2	13.4	0.1	0.60	1.10
0.30	17.5	0.2	13.0	0.2	1.03	1.35
0.30	26.1	0.2	14.6	0.1	0.76	1.00
0.30	34.1	0.2	16.6	0.1	0.50	0.86

Table 3.1: Average values of current and voltage for different pressures, with their respective statistical error. The last two columns show the percentage variation with respect to the mean value.

3.2.2 Spectral shape

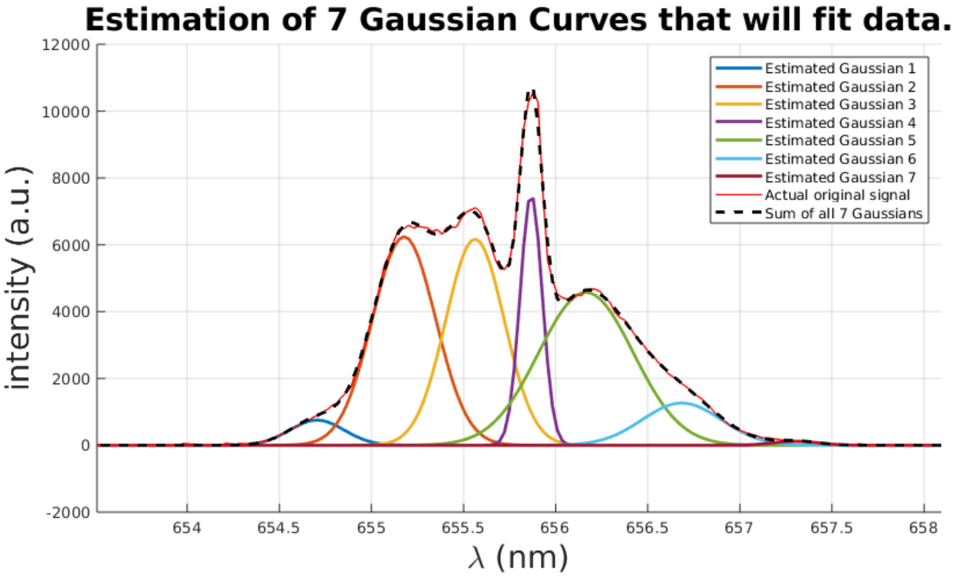

Figure 3.15: Gaussian fit on the signal.

A typical recorded spectrum is shown in Fig.3.15. The features that can be noticed about the spectrum (which will be present also in the following spectra) are:

- The most intense component of the spectra is the central peak (gaussian #4 in Fig.3.15, due to H_α emission of excited background hydrogen (either due to dissociative excitation or direct excitation of loose H atoms);
- The blue shifted part is composed of three evident peaks at different values of the shift;
- The red-shifted part shows clearly only a first inner peak, meaning that gaussian #6 of the fit is less intense;
- The blue-shifted component is more intense than the red shifted one;

Broadening effect due to electrons causes the broadening of the base [4], while the shoulders are a sign of the presence of directioned fast excited neutrals with a maximum velocity correspondent to where the outermost shoulder ends.
As it is presented, the spectrum provides the convolution of the neutrals' angular and velocity distributions. Trying to separate the two is difficult, but several steps can be made to facilitate the interpretation, intersecting only one microchannel being one, as it immediately will entail that most of the collected light comes from a fixed channel, with a defined direction.

p *Pa*	**V** *kV*	**I** *mA*	$\left(\frac{\mathbf{\Delta\lambda(H^+)}}{\mathbf{\Delta\lambda(H^+_{2.5})}}\right)^{\mathbf{2}}$	$\left(\frac{\mathbf{\Delta\lambda(H^+)}}{\mathbf{\Delta\lambda(3)}}\right)^{\mathbf{2}}$
0.3	9.54	26.0	2.4±0.5	14±1
0.3	9.90	37.3	2.4±0.4	14±1
0.3	8.50	13.3	2.4±0.5	14±1
0.5	7.00	26.0	2.3±0.4	15±1
0.5	7.44	36.0	2.3±0.4	15±1
0.5	8.00	40.0	2.4±0.5	16±2
0.7	5.54	26.0	2.5±0.6	16±1
0.7	5.83	31.8	2.3±0.6	15±2
0.7	5.81	35.7	2.4±0.5	15±2
1	4.18	20.2	2.5±0.7	11±3
1	4.34	26	2.4±0.6	11±3

Table 3.2: Ratio between wavelength shifts of the two outermost peaks in the spectrum, at different conditions of pressure and applied voltage.$\Delta\lambda(3)$ refers to the shift of Gaussian #3 with respect to the central one.

Still, the question remains on how information about particle kinetic energy can be extracted from the recorded spectra. It is reasonable to assume that fast neutrals are not mono-energetic, due to the processes that give birth to them and due to elastic collisions. The first reason refers to the fact that they are created from ions accelerated by the cathode potential, which could be born at any position in the vessel; therefore, if there is no preferential birth radius for ions, the energy distribution of neutrals coming in or out of the cathode grid cannot be mono-energetic. As it seems, however, there is a more intense peak correspondent to a defined wavelength. Such peak moves when applying different voltage or pressure, so it is not an effect of the experimental apparatus. The results from the simulated discharge show that the blue-shifted component of the radiation collected from a single microchannel is dominant, as observed. However, simulations, where a virtual anode is not formed inside the cathode grid, do not predicted the peak which is observed in the experiment.

In order to try and understand where all the peaks in the spectrum come from, it is necessary to assign some properties to them, such as position and intensity. In order to do so, a fit with multiple gaussians was employed; though the peak is properly reproduced, it is not explained physically why such peaks should be gaussians.

Difficulties of the fit are:

- The outermost blue-shifted shoulder is often too low in intensity to be properly fit;
- The red-shifted component of the spectrum does not present a clear peak, resulting in a less precise fit.

Nevertheless, the information about the shift of the peak has made clear that the two outermost shoulders are created by H^+ and $H^+_{2.5}$ ions undergoing charge exchange. H_3^+ and H_2^+ are considered to be part of the same peak, as they cannot be distinguished.

Tab.3.2 shows evidence that the two outermost peaks actually correspond to the previously mentioned ions, as the ratio between the two wavelength shift is always between $\sqrt{2}$ and $\sqrt{3}$; since the square of such ratio corresponds to the ratio between the energies, and therefore the ratio between particles masses, which is more intuitive to understand, the displayed result is therefore $\left(\frac{\Delta\lambda(H^+)}{\Delta\lambda(H^+_{2.5})}\right)^2$.

The innermost peak, which also presents its red-shifted counterpart, cannot be explained in terms of another ionic specie creating a fast excited neutral via charge exchange; moreover, the ratio between its shift and the shift of the $H_{2.5}^{+}$ peak changes with pressure, while the effect of the applied voltage is negligible if present. If the innermost peak belonged to another micro-channel, then such microchannel would form an angle θ' with the line of sight such that $cos(\theta')/cos(\theta)$ is equal to approximately one third of the value on the last column of Tab.3.2. Since a variation of such an angle with changing physical parameters is not expected, the change in the ratio cannot be explained using geometrical interpretation. Moreover, if really such contribution comes from a different micro-channel, vertical sweeps done in the following section would reveal a variation in its intensity as the line of sight is moved. We therefore postpone its interpretation to the next section.

3.2.3 Error on kinetic energy value

Once the Doppler wavelength shift is estimated using gaussian fits, it is possible to calculate the velocity of the particle responsible for emitting a photon with $\lambda = \lambda_0 \pm \Delta\lambda_{Doppler}$ according to:

$$v = c\frac{\lambda_{Doppler} - \lambda_0}{\lambda_0 cos(\phi)} \tag{3.7}$$

consequently, the error on the calculated velocity value depends on the error in determining the angle between the line of sight and the channel, the error on the calculated λ_0 and on the calculated $\lambda_{Doppler}$. The latter two values are correlated, since they are found from the same interpolation.

The error on the angle ϕ is linked to the geometrical reconstruction of the lines of sight and the channel, which suffers from many systematic errors. Therefore, such error will be treated as a systematic error. Moreover, since the main interest is determining how the kinetic energy of particles varies with the scanned position and not its absolute value, error on ϕ is of little interest in the present measurements, as it affects in the same way all calculated E_k.

As for the error on $\lambda_{Doppler}$ and λ_0, it must be taken into consideration that the proposed fit is not explained physically, therefore there is no reason why we should use only one value of the wavelength shift to calculate the corresponding kinetic energy, but rather an interval corresponding to the width of the fitting gaussians. From now on, values of energy will presented in terms of possible intervals, rather than absolute values.

Finally, energy suffers from systematic errors independent from the measurements and correlated to the non-stable nature of the discharge, introducing an oscillation of the order of 200eV as calculated in Sec.3.2.1.

3.2.4 Effect of pressure and voltage

Applied cathode voltage is expected to change the spectral shape by widening or narrowing the Doppler-shifted shoulders if the voltage is increased or decreased respectively. In order to study such behaviour, the position of the line of sight was kept constant throughout a series of measurements with varying applied voltage.

It is necessary to remember that after the initiation of the discharge, very small variations in applied potential cause major variations in current value; in particular, it was not possible to increase current up to values above $40mA$, as the cathode grid would start glowing and shaking.

Fig.3.16 through 3.18 shows the spectra evolution as the applied voltage is changed at different pressure values. The choice of using exclusively the blue-shifted components is due both to the more reliable fit allowed by the intense peaks and the easier interpretation of the outermost peaks as linked to H^+ and $H_{2.5}^{+}$. In the examined case, the variation of kinetic energy associated with the varying applied voltage is barely distinguishable; in the case of H^+ (blue curve), the interval of possible kinetic energy is shifted so that it always overlaps with the previous ones, therefore

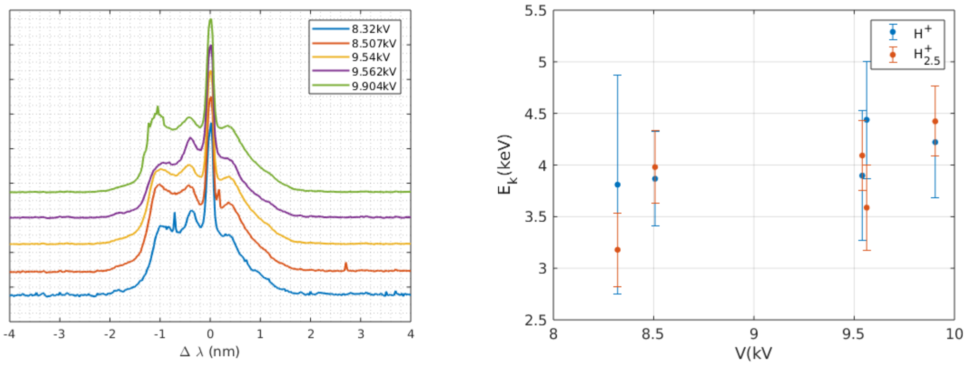

(a) Spectra at varying applied voltage.
(b) Calculated kinetic energy of H^+ and $H^+_{2.5}$.

Figure 3.16: Analysis on spectra at p=0.3Pa and varying applied cathode voltage.

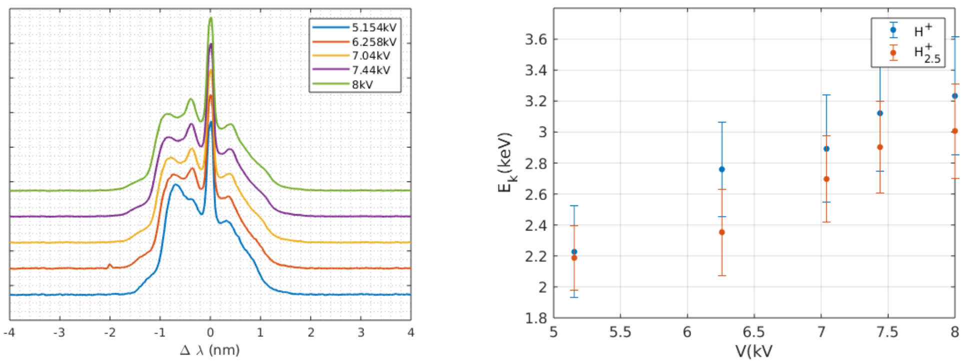

(a) Spectra at varying applied voltage.
(b) Calculated kinetic energy of H^+ and $H^+_{2.5}$.

Figure 3.17: Analysis on spectra at p=0.5Pa and varying applied cathode voltage.

not allowing a clear interpretation in terms of increasing kinetic energy. $H^+_{2.5}$, on the other hand, draws a clearer line, though this interpretation is heavily dependent on the point further left. At higher pressure, the dependence is detected more easily. Linear interpolation of the data reveals an increase in energy related to the increase in voltage by $\Delta E_k(keV) \sim 0.45\Delta V(kV)$. At p=0.5Pa $\Delta E_k(keV) \sim 0.31\Delta V(kV)$, while at p=0.7Pa $\Delta E_k(keV) \sim 0.35\Delta V(kV)$.
Finally it is interesting to calculate the ratio between the ion kinetic energy and the applied voltage value. The calculated ratios for all the measurements presented above are shown in Fig.3.19. All previous evaluations were made at an outer position, where the radiation produced by the microchannel is dominant and the shifted peak is easy to detect. However, it is also interesting to analyze the behaviour at a central position.
Results are shown in Fig.3.20. In this case, since the red-shifted shoulder is intense enough to provide valid results from the fit, both blue and red-shifted components are shown. In both cases the shift tends to increase as a function of applied voltage; however, the trend is still within the energy error.

3.2.5 Vertical sweeps

Exact position of micro-channel depends on grid geometry and symmetry, as their formation relies heavily on the position of the grid wires. Moreover, the presence of the stalk perturbes the potential in such a way that may affect the ion motion and the position of the channel.
Since it is analytically not efficient to try to determine the coordinates of the desired line of

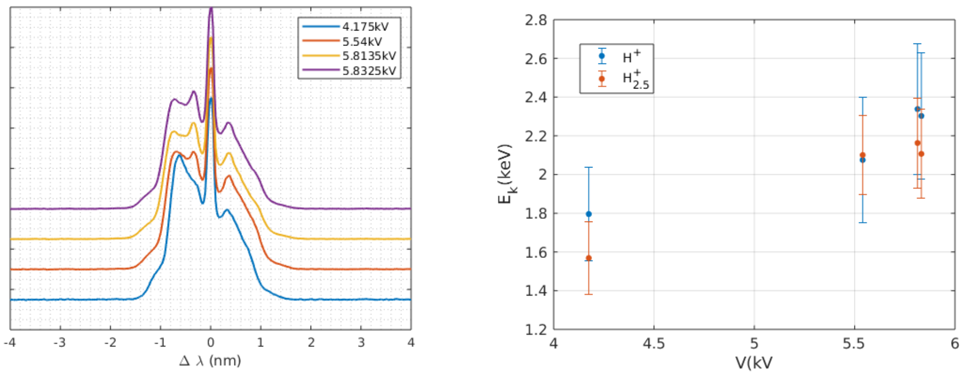

(a) Spectra at varying applied voltage.

(b) Calculated kinetic energy of H^+ and $H^+_{2.5}$.

Figure 3.18: Analysis on spectra at p=0.7Pa and varying applied cathode voltage.

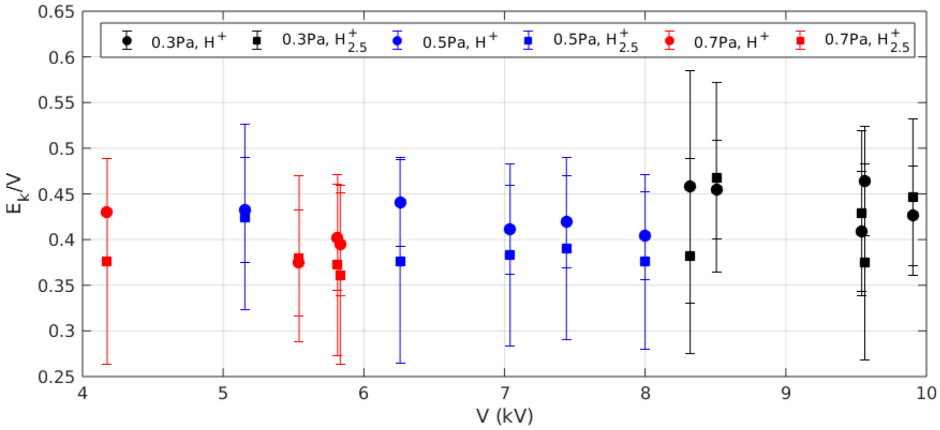

Figure 3.19: Ratio between ion kinetic energy and applied voltage as a function of applied voltage for different pressure values.

sight an empirical method was elaborated.
For each position in the horizontal direction, the full vertical sweep is completed, moving the remotely controlled rotating stage without interrupting the discharge.
The measurements are taken for each horizontal position and at different values of pressure. The aim of the procedure is to detect the radiation coming from the microchannel and to determine whether or not different pressure entails different microchannel dimension.

Fig.3.21 and 3.22 show the evolution of the recorded spectra with hydrogen as the vertical movement is performed.
Firstly, the blue-shifted component is analyzed. The horizontal position chose is such that only one microchannel will give a dominant blue-shifted component, while the others will give a dominant red-shifted component. This is due to the fact that the spectrum is expected to be predominantly blue-shifted, due to the contribution given by fast neutrals, which are more abundant in the diverging population, as shown both by previous experiments and by the numerical simulations.
Consequently, the showing up of a strong blue-shifted shoulder is a symptom of the intersection with the selected microchannel. This happens only around certain position. In the selected case $98.20 \sim 98.22$. On the other hand, as the line of sight is moved further down, the red-shifted wing starts to grow as well, though not as much as the blue-shifted one. This is due to the intersection of the line of sight with a second microchannel 3.24, with particles moving in the opposite direction with respect to the line sight compared to the previous case. The geometrical

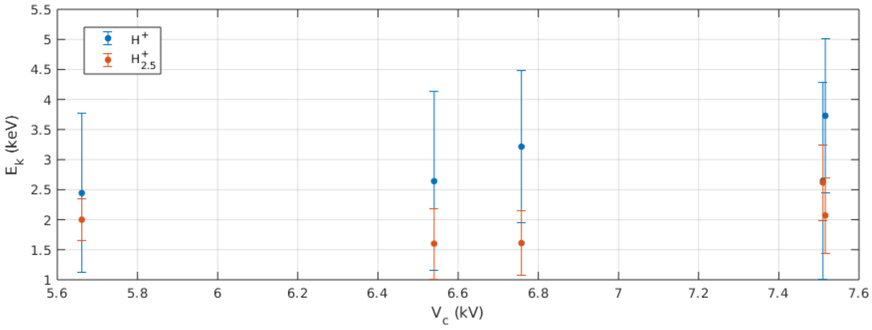

(a) Blue-shifted shoulder.

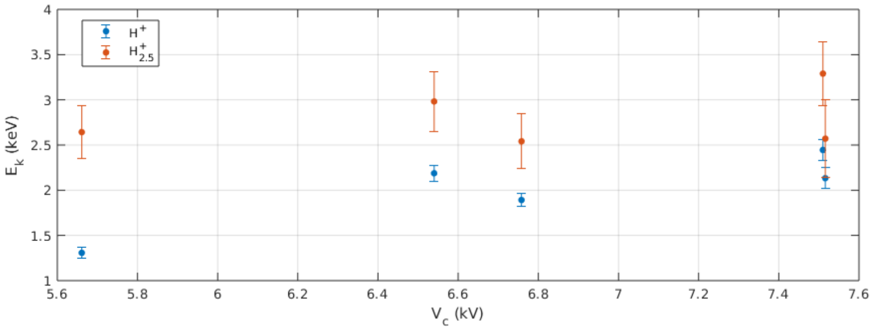

(b) Red-shifted shoulder.

Figure 3.20: Calculated kinetic energy of H^+ and $H^+_{2.5}$, as a function of applied voltage at p=0.5Pa, calculated from spectra acquired in a central position.

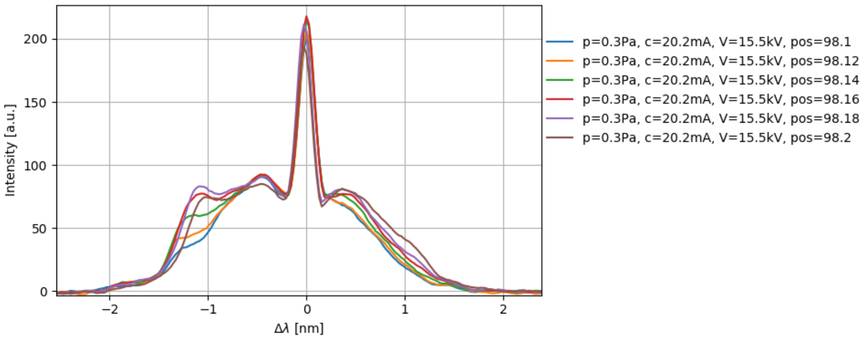

Figure 3.21: First part of the vertical sweep at position 100 in the horizontal direction.

reconstruction built using the calibration shows how the lowering of the line of sight causes the intersection with a second microchannel; this is shown in Fig.3.24. According to the geometrical reconstruction, the line of sight forms with such channel an angle comparable with the one formed with the previous channel. This explains why the emerging shoulder appears at a comparable value of $\Delta\lambda$. Moreover, the lower intensity is due to the fact that the second microchannel is intersected at a position further away from the cathode grid, where particle density is falling for each species and therefore the contribution to emitted radiation is lower.

In order to quantitatively determine the optimal position for the line of sight in order to detect the proper microchannel, the spectrum was fit with multiple gaussian peaks, as described previously.

The parameters that gives a more direct indication of the relevance of a particular peak is its

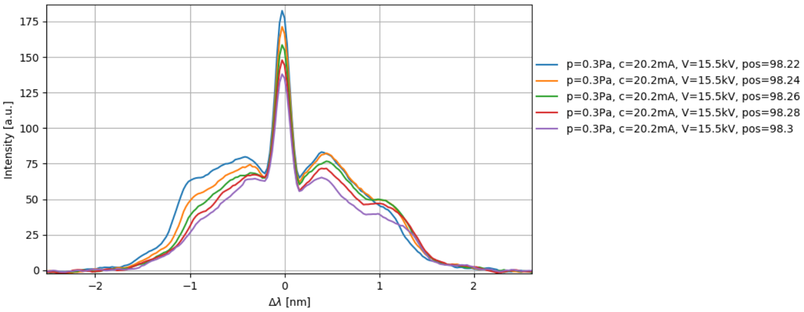

Figure 3.22: Second part of the vertical sweep at position 100 in the horizontal direction.

maximum intensity; its variation during a vertical shift is depicted in Fig.3.25 at different positions in the horizontal direction. The error on peak intensity is given by Poisson distribution and its equal to $\sqrt{N}$, where N is the number of counts of a single wavelength bin.
All plots show that peak (3) reaches a maximum at a certain vertical position, which varies as the line of sight is moved closer to the cathode grid. The same behaviour is followed by the amplitude of the central peak (peak (4)). In principle, this method could be applied to the determination of micro-channel width as a function of horizontal position also in different physical conditions. In order to do so, a finer interval of angles should be investigated.
Moreover, while in the pressure range $p < 1Pa$ the effect of the presence of a microchannel is evident, when pressure is increased, like at $4Pa$, shoulders cease to exist as defined as they are in the low pressure star-mode regime. Fig.3.23 shows such evolution.

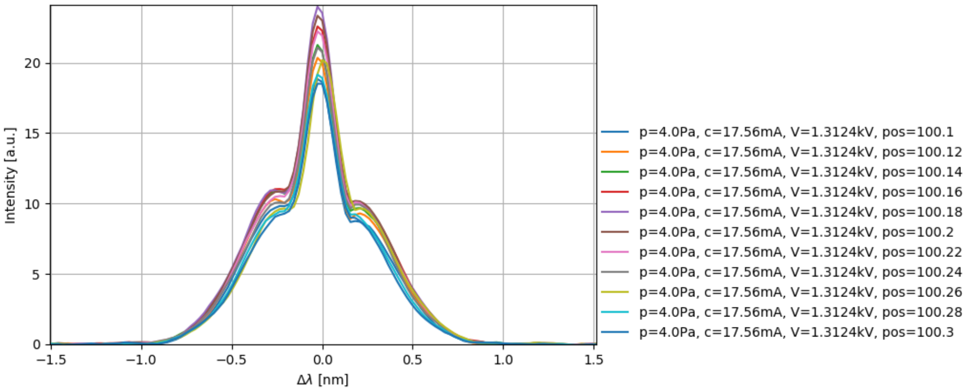

Figure 3.23: Evolution of the spectra during a vertical sweep at p=4Pa.

3.2.6 Horizontal sweeps

In the previous sections we have established what is the variation in kinetic energy that we are capable of detecting and what are the correct coordinates required to intersect the selected microchannel.
In the following measurements done at such positions are presented. Fig.3.26 and 3.27 show the spectra evolution as the line of sight is moved closer to the center (which is located at the position 93). On the right hand side the conversion of the wavelength shift into kinetic energy is shown. Only the shoulders identified as the diverging neutrals born either from $H_{2.5}^{+}$ and H^{+} is converted into kinetic energy, as they are the only ones that can be easily associated with a given particle and therefore a given mass. The red shifted peak which should mirror the blue-shifted

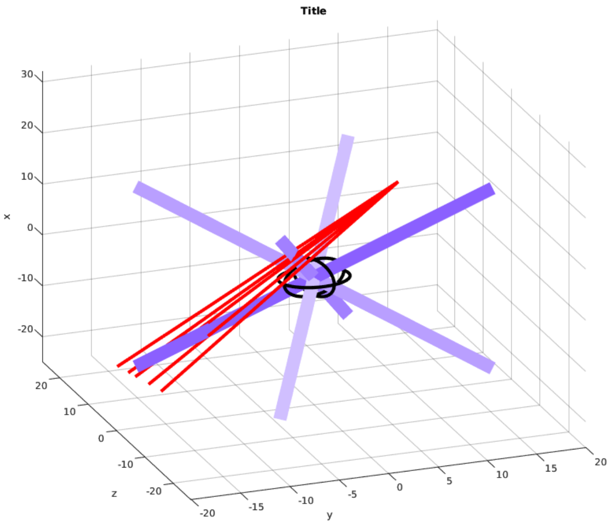

Figure 3.24: Geometrical reconstruction of lines of sight during a vertical sweep.

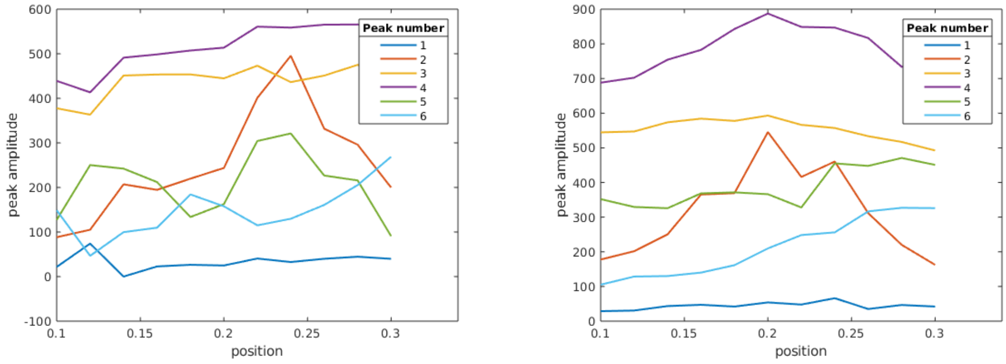

(a) Position 102.

(b) Position 100.

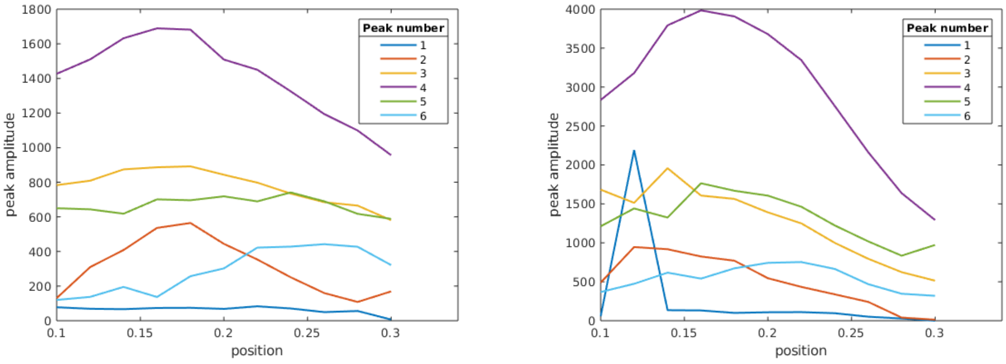

(c) Position 98.

(d) Position 95.

Figure 3.25: Peak intensity evolution during vertical sweep at different horizontal positions.

one is less evident, which caused the fitting algorithm to struggle in positioning it; therefore, the kinetic energy value associated with such term tend to oscillate without following a clear behaviour. This is more due to the fitting algorithm than to the actual physics that causes its presence. Moreover, the innermost peaks, both on the blue-shifted side and on the red-shifted side will be analyzed on their own in a separate section.
From the aforementioned plot, a clear decrease in detected kinetic energy is shown as the line of

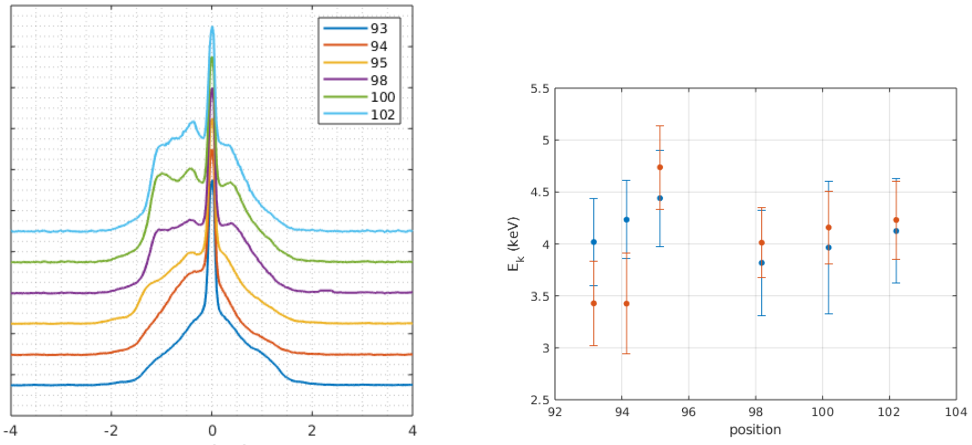

(a) Spectra at different horizontal positions.

(b) Calculated kinetic energy of H^+ (blue) and $H^+_{2.5}$ (orange).

Figure 3.26: Analysis on spectra at p=0.3Pa,V=9.5kV,I=26mA.

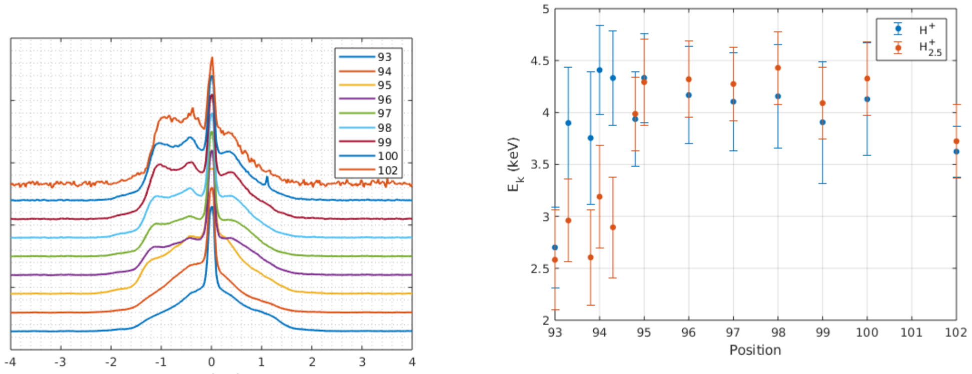

(a) Spectra at different horizontal positions.

(b) Calculated kinetic energy of H^+ (blue) and $H^+_{2.5}$ (orange).

Figure 3.27: Analysis on spectra at p=0.3Pa,V=8.8kV,I=20mA.

sight is moved towards the cathode (cathode is crossed at position ~ 95). In the case of Fig.3.27 such decrease is clearer, as finer measurements inside the cathodic region were conducted.

Analysis of peaks inside the cathode region is made difficult by the fact that it is possible that more micro-channels are intersected at that point and the angular distribution of fast excited neutrals is less peaked around a defined value. This causes an enlargement of the peak; moreover, symmetry in peak shape is reached at around ~ 93, which means that the central core is interesected at such position.

Similar measurements conducted at higher pressure, are shown in Fig.3.28,3.29,3.30 and 3.31. The same decreasing trend inside the cathode is found. Moreover, the estimation for kinetic energy outside the cathode stays almost constant as the line of sight is moved outwards. This behaviour could be due to the fact that fast neutrals, whose kinetic energy is not affected by the potential, contribute heavily to the spectrum.

On the other hand, keeping constant pressure and changing current and voltage does not seem to affect significantly the observed evolution of kinetic energy.

Intensity of the blue-shifted shoulder with respect to the other components of the peaks increases as the line of sight is moved outwards.

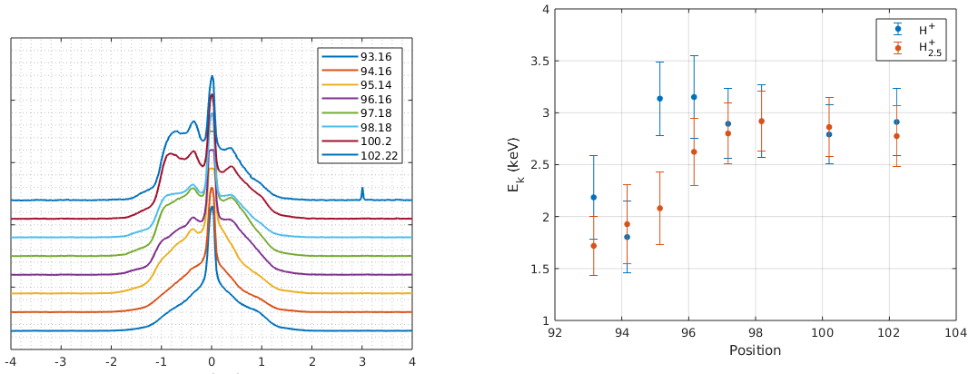

(a) Spectra at different horizontal positions.

(b) Calculated kinetic energy of H^+ (blue) and $H_{2.5}^+$ (orange).

Figure 3.28: Analysis on spectra at p=0.3Pa,V=6.5kV,I=26mA.

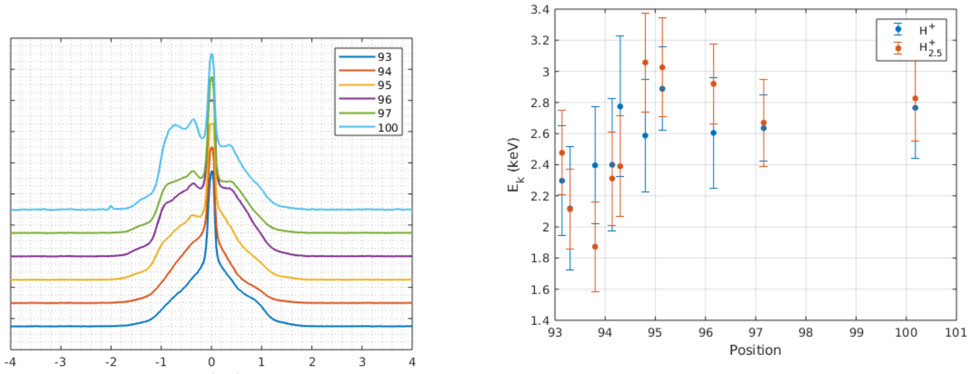

(a) Spectra at different horizontal positions.

(b) Calculated kinetic energy of H^+ (blue) and $H_{2.5}^+$ (orange).

Figure 3.29: Analysis on spectra at p=0.5Pa,V=6.2kV,I=20mA.

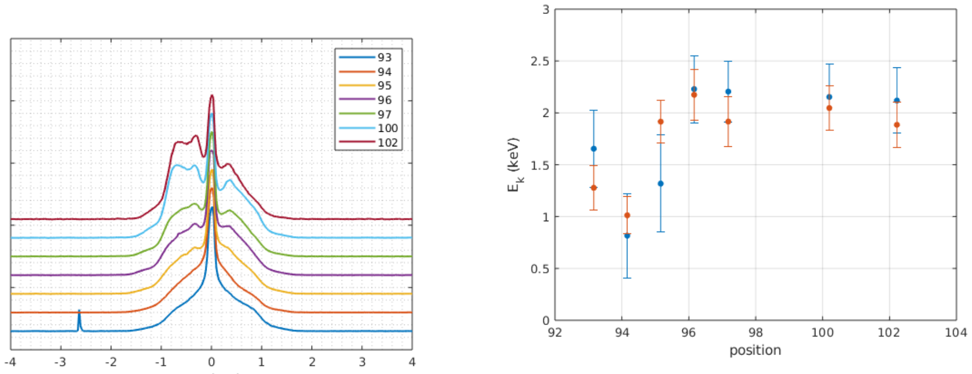

(a) Spectra at different horizontal positions.

(b) Calculated kinetic energy of H^+ (blue) and $H_{2.5}^+$ (orange).

Figure 3.30: Analysis on spectra at p=0.7Pa,V=5.5kV,I=26mA..

As pressure is increased to $1Pa$ and $1.5Pa$, the resulting spectra show a more noisy behaviour when it comes to the determination of kinetic energy, though a decrease when the line of sight is moved inwards can still be observed.

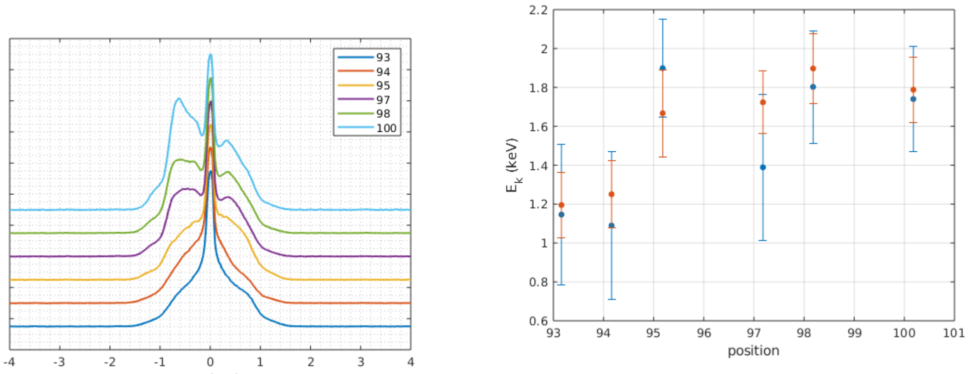

(a) Spectra at different horizontal positions.

(b) Calculated kinetic energy of H^+ (blue) and $H^+_{2.5}$ (orange).

Figure 3.31: Analysis on spectra at p=0.7Pa,V=4.6kV,I=15mA.

It is important to observe that the behaviour shown by H^+ is not in accord with the one shown by $H^+_{2.5}$, as their kinetic energy is not evidently shifted. Again, the low intensity of the peak might have affected the accuracy of the fit.

Furthermore, in all examined cases, the intensity of the blue-shifted shoulder increases as the line of sight is moved outwards, meaning that fast ions moving outwards constitute most of the de-exciting particles in such regions.

Finally, measurements conducted at p=4Pa are analyzed. It was already determined that at such pressure no microchannel is detectable, as the vertical sweeps do not show the same spectra evolution that was obtained at lower pressure. Therefore, the angular distribution of the excited neutral contributing to the collected radiation is not peaked around a defined angle. If the plane where both the centre of the vessel and the line of sight lay is considered, something similar to Fig.3.34 is obtained. The dashed lines represent the possible particle trajectories that may intersect the line of sight; the geometry of the problem reveals that though there is no preferred direction with respect to the line of sight, only a fixed interval of angles is detected, provided that particles move radially.

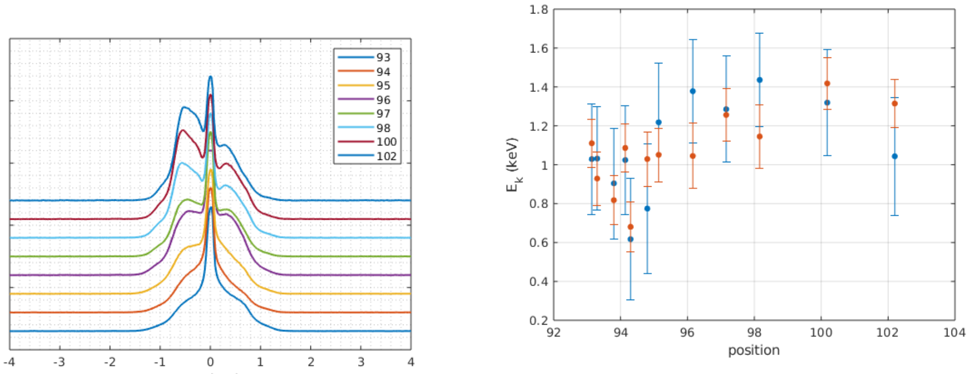

(a) Spectra at different horizontal positions.

(b) Calculated kinetic energy of H^+ (blue) and $H^+_{2.5}$ (orange).

Figure 3.32: Analysis on spectra at p=1Pa.

The spectra coming from such measurements were fit with only three gaussians: one for the blue-shifted shoulder, one for the central peak and one for the red-shifted shoulder. The results are plot in Fig.3.35; $\Delta\lambda$ for the blue and red-shifted shoulder appears to vary within the error, therefore no conclusion on whether the kinetic energy is actually increasing or decreasing can

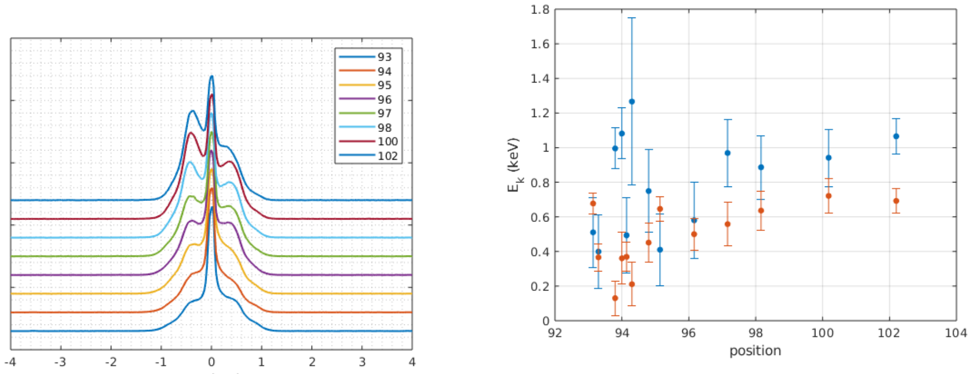

(a) Spectra at different horizontal positions.

(b) Calculated kinetic energy of H^+ (blue) and $H_{2.5}^+$ (orange).

Figure 3.33: Analysis on spectra at p=1.5Pa.

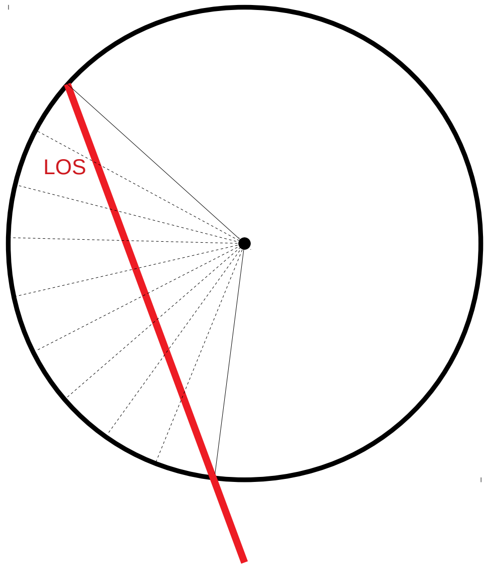

Figure 3.34: Geometrical reconstruction of the line of sight for measurements at p=4Pa.

be drawn.

In the following evolution of the red-shifted shoulder will be considered. Due to the lack of definition of such peak, only low pressure measurements will be used.
The analysis of red shifted shoulders (Fig.3.36 ,3.37,3.38) shows that ion kinetic energy does not show a behaviour as clear as the one highlighted by the blue-shifted curve, but rather looks constant within the error.
If the red shifted shoulder is produced by particles moving inwards, the results shows that at any position the neutrals are born from ions having roughly the same kinetic energy. Even though inward moving ions could be born at any of the positions at a radius greater than the point of the measurement, therefore indicating the possibility of having any possible energy, the mean free path for charge exchange is determined by pressure, therefore before undergoing such reaction, ions travel a fixed amount of space, thus gaining a fixed amount of kinetic energy.
If this were the case, then lowering the pressure would cause increase in the fraction of the potential that is accelerating the particles, while the fraction is in all cases $\sim 35\%$, slightly lower than the one which will be calculated for diverging ions.

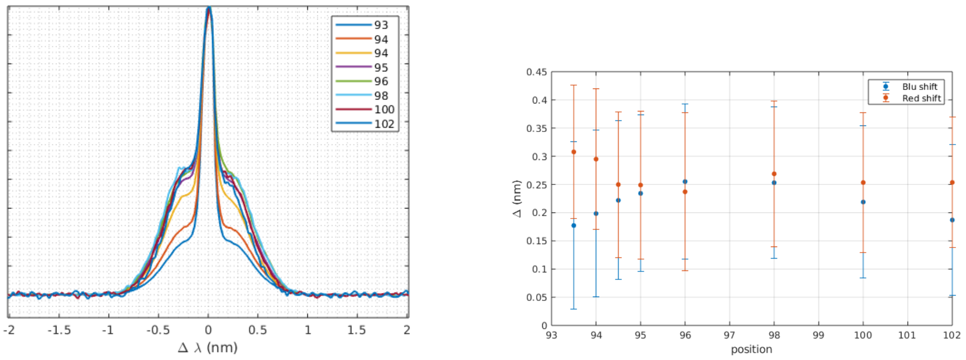

(a) Spectra at different horizontal positions.

(b) Blue and red shift.

Figure 3.35: Analysis on spectra at p=4Pa.

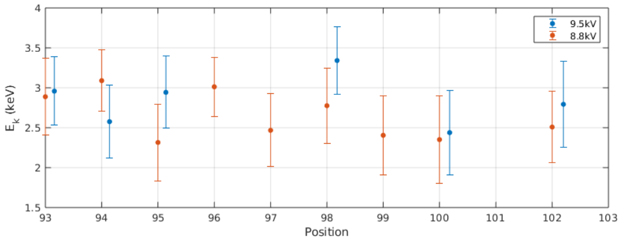

Figure 3.36: Kinetic energy associated to the red-shifted $H^+_{2.5}$ peak as a function of position, at 0.3Pa.

Explaining them as ions oscillating back wouldn't be possible, as the mean free path for charge exchange is too short, and any ion would have turned into a fast neutral by the time it crossed the centre.

3.2.7 Kinetic energy outside the cathode

As observed before, the kinetic energy calculated for particles moving outwards outside the cathode keeps an almost constant value, which lead to believe that fast neutrals are actually responsible for such peak.
In order to see if there is a significant difference with respect to the operating pressure, the ratio between the average kinetic energy outside the cathode and the applied voltage is calculated; results are displayed in Tab.3.3.

Results show that the ratio between the estimated kinetic energy value and the applied voltage decreases as pressure is increased. This means that ions are accelerated by a smaller fraction of

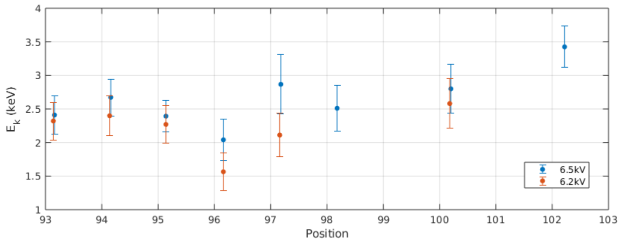

Figure 3.37: Kinetic energy associated to the red-shifted $H^+_{2.5}$ peak as a function of position, at 0.5Pa.

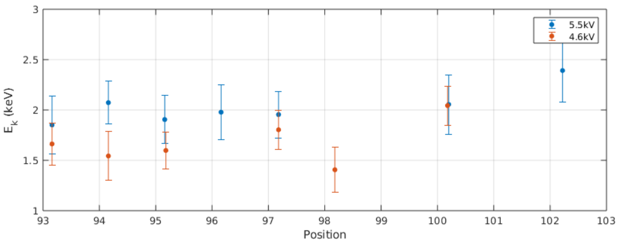

Figure 3.38: Kinetic energy associated to the red-shifted $H_{2.5}^{+}$ peak as a function of position, at 0.7Pa.

p *Pa*	**V** *kV*	**I** *mA*	$\mathbf{E}_k$ *keV*	$\mathbf{E_k/V}$
0.3	9.5	26	4.3 ± 0.3	0.45 ± 0.03
0.3	8.8	20	4.2 ± 0.2	0.48 ± 0.03
0.5	6.5	26	2.7 ± 0.2	0.41 ± 0.03
0.5	6.2	20	2.6 ± 0.2	0.42 ± 0.03
0.7	5.5	26	2.0 ± 0.1	0.36 ±0.02
0.7	4.6	15	1.8 ± 0.1	0.38 ± 0.02
1	3.8	20	1.2 ± 0.2	0.32 ± 0.04
1.5	2.9	20	0.6 ± 0.1	0.22 ± 0.03

Table 3.3: Average value of kinetic energy outside the cathode region divided by the applied voltage.

the potential at higher pressure, which can be explained considering the decrease of mean free path.

3.2.8 Kinetic energy in the centre

From the above analysis it seems that particle are decelerating as they get closer to the centre. In order to determine how this effect is related to pressure and applied voltage and current, we will consider, for every set presented above, a mean value of kinetic energy associated to the central position, and compare it to the applied voltage.
Tab.3.4 presents all such values.
Though the error on the ratio value is in some cases $> 20\%$, a general decreasing trend of the ratio with pressure is detected, though separating the dependence of the applied voltage is complicated.
In fact, this behaviour could be related to the potential in the centre itself. As the analysis of the simulation results in Chap.4 showed, the central value of the potential increases with respect to the applied voltage as pressure and current are increased.

3.2.9 Study of the mysterious peak

Until now, only the peaks associated with H^+ or $H_{2.5}^{+}$ were taken into consideration for energy calculations, as the nature of the innermost peak was not known. In this section we will consider its behaviour.
Fig.3.39, 3.40 and 3.41 show how the peak on the red-shifted side and on the blue-shifted side behave a function of applied voltage. Such figures show a constant shift within the error; increased pressure causes decrease in the shift.

p	**V**	**I**	**E_k/V**
Pa	*kV*	*mA*	
0.3	9.5	26	0.36±0.04
0.3	8.8	20	0.32±0.07
0.5	6.5	26	0.29±0.08
0.5	6.2	20	0.26±0.08
0.7	5.5	26	0.23±0.04
0.7	4.6	15	0.27±0.04
1	3.8	20	0.24±0.08
1.5	2.9	20	0.10±0.07

Table 3.4: Values of the ratio between applied voltage and average kinetic energy in the centre at different pressures.

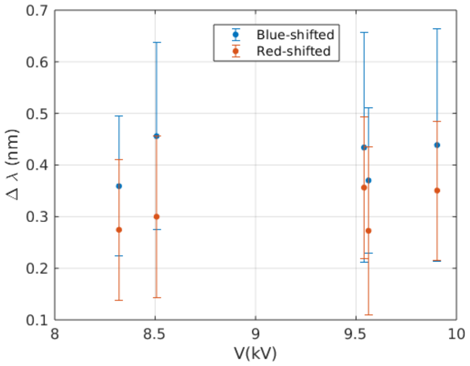

Figure 3.39: Doppler shift as a function of applied voltage, at p=0.3Pa.

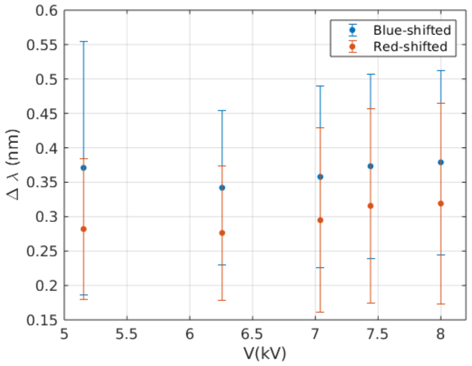

Figure 3.40: Doppler shift as a function of applied voltage, at p=0.5Pa.

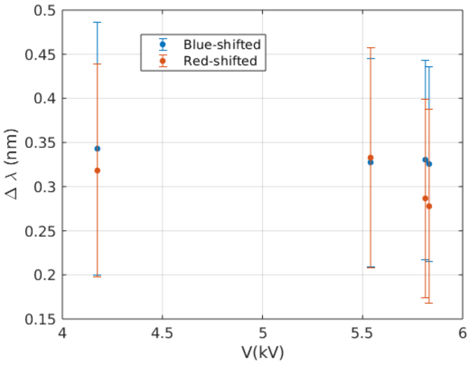

Figure 3.41: Doppler shift as a function of applied voltage, at p=0.7Pa.

Further analysis also on the horizontal sweeps reveals that the shift evolves in the same way as the ones already pictured, as an example, Fig.3.42 and 3.43 show the evolution at the two lower values of pressure.

This leads to believe that the two peaks are related to the observed microchannel and therefore are linked to ions that are moving along it.

The two peaks which are considered are n.(3) and n.(5) depicted in the section regarding vertical sweeps. Their intensity does not change as much as the outer one, identified as $H^+_{2.5}$.

Previous studies have identified the contribution as another population of $H^+_{2.5}$ having lower kinetic energy, however there is no evident reason why there should be another ion population. Moreover, the results in Tab.3.2 show that the particle responsible for the peak should have a mass that is ≈ 14 times the one of hydrogen. Since the closer the peak to the center, the

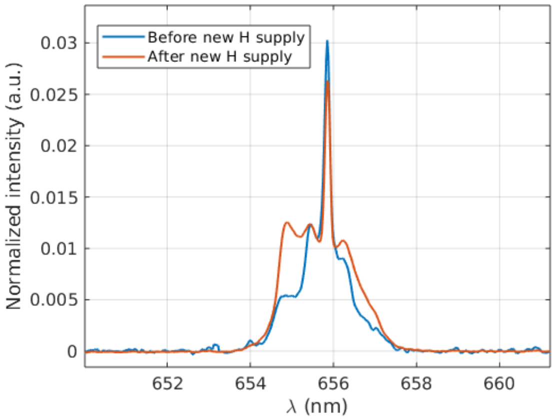

Figure 3.44: Spectra acquired before and after changing the hydrogen supply, at p=0.3Pa and similar applied voltage.

more it is affected from positioning errors of the fitting algorithm, if we assume such value as an indication of order of magnitude, the mass could refer the presence of water vapour impurities, in particular OH^- (m=16amu) ions.

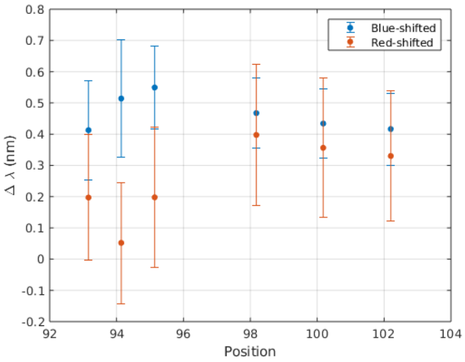

Figure 3.42: Doppler shift as a function of postion, at p=0.3Pa.

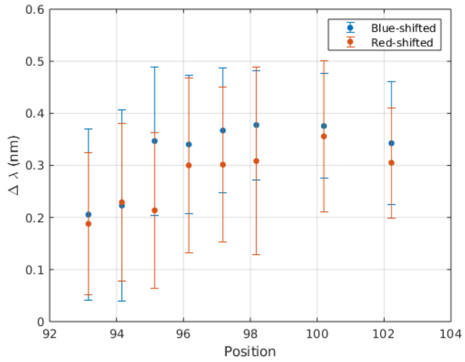

Figure 3.43: Doppler shift as a function of position, at p=0.5Pa.

Moreover, Fig.3.44 shows the transformation of the spectrum before and after changing the hydrogen supply, showing a consistent increase in what is believed to belong to fast H_2^+ radiation. Fig.3.17 and 3.18 show an increase of such shoulder when the applied voltage is decreased: this is however due to the fact that the outermost shoulder is closer to the innermost one.

3.2.10 Central peak evolution

The broadening of the central peak is consistent with the calculated instrumental broadening; broadening caused by room-temperature excited atoms would be two orders of magnitude lower than the broadening caused by the apparatus, therefore its contribution is negligible in our measurement.

Furthermore, intensity of the central peak is investigated as a function of applied voltage at constant pressure and constant position. This is done to establish the accord with previous measurements.

3.2.11 Discharge composition

Sec.2 introduced a method previously applied to the analysis of the spectroscopic analysis of the fusor discharge in order to determine the composition of the discharge.
This method was applied to all the spectra measured before. Results at constant pressure, but increasing applied voltage are shown in Fig.3.45. Analysis of the discharges at 1Pa and 1.5Pa returns an average composition of $80\% - 20\%$, that is an increase of fast H^+ on the population with respect to higher pressure valuse.

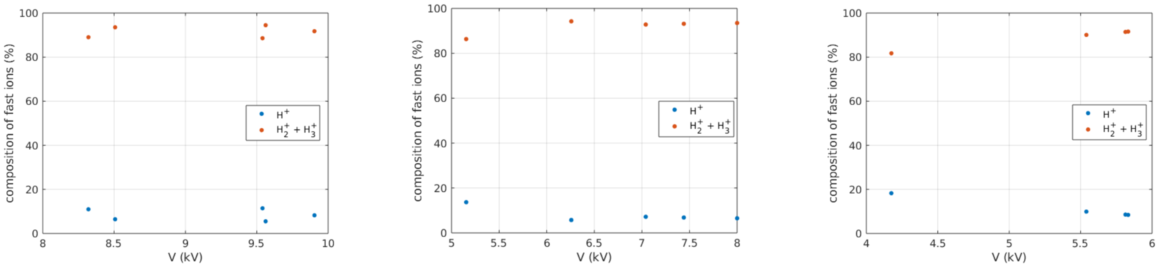

(a) 0.3 Pa. (b) 0.5 Pa. (c) 0.7 Pa.

Figure 3.45: Composition of the fast ion population at different pressures.

The accuracy of the calculated value depends on many factors, among the most relevant are: the fact that the ions are actually not monoenergetic, the low accuracy of cross sections, the fact that it is not possible to distinguish H_2^+ and H_3^+ peaks and that therefore the cross section is calculated as an average between the one of the two different charge exchange reactions. Order of magnitude of the discharge composition is nevertheless reproduced.
Finally, the degree of dissociation of the background gas can be extimated as the ratio between the area of the Balmer$_\gamma$ peak and the integral of the Fulcher band, which is due to molecular hydrogen [10].
Since the Balmer$_\gamma$ peak is expected to suffer from the presence of a fast neutral contribution, reproducing the spectrum requires a combination of gaussians in order to extrapolate the contribution due only to background hydrogen atoms.
Fig.3.46 shows a comparison between the obtained Fulcher band at 0.5Pa, at the centre of the discharge and previous results. The spectra agree very well. Considering the whole peak of Balmer$_\gamma$ emission, the fraction of dissociated hydrogen corresponds to $\sim 15\%$ of the total background particles.
If, however, fast particles are exluded from the computation, the fraction falls to $\sim 5\%$.

3.3 Helium discharges

Measurements using helium were conducted, due to shortage of hydrogen supply.
The most intense spectral line found in He spectrum is the one at $\sim 587nm$; the transition consists in the transition form level 1s3d (^3D) to level 1s2p (^0P), characterized by a transition rate of $\sim 1 \times 10^8\ s^{-1}$.
Fast neutrals excited to the 1s3d level are born from collisions of He^+ with background He causing selective electron capture to the specified level. According to ALADDIN database [1], the most probable outcome is a neutral with an electron in level $1s3d$, which justifies the choice that was made.
The experimental procedure consisted in keeping fixed the angle ϕ, while varying θ with a remote controller provided by ThorLabs, in order to scan in the vertical direction without shutting down the discharge. The angle ϕ is the varied and another vertical sweep is conducted. This

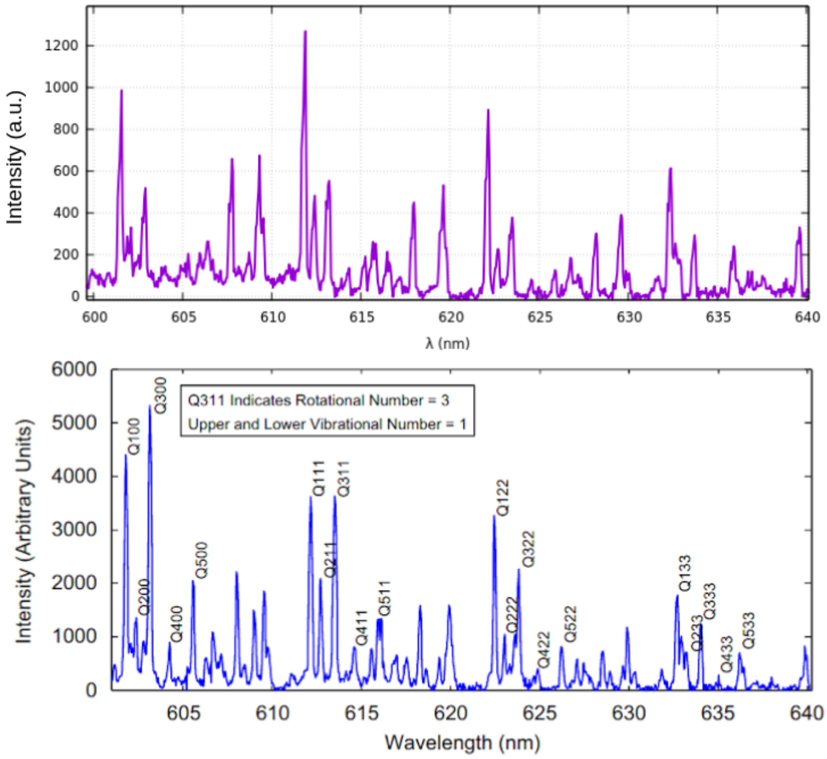

Figure 3.46: Experimental Fulcher band (top) compared to previous results (bottom) [11].

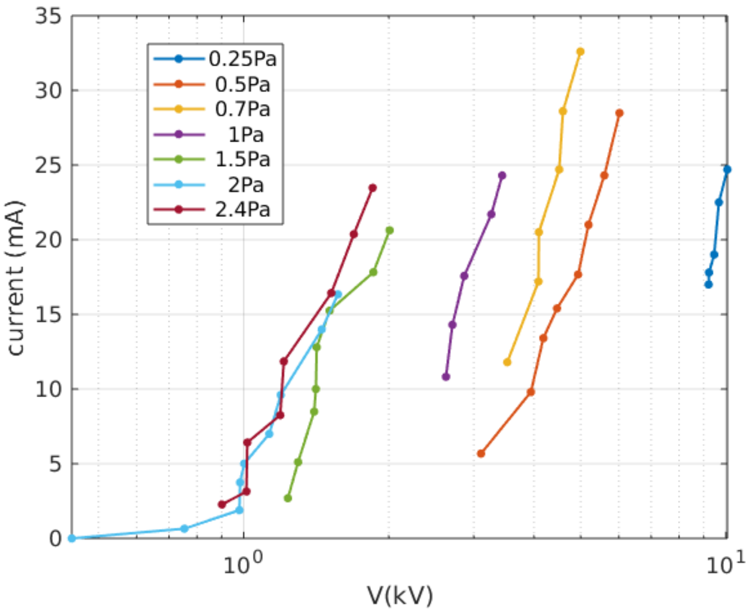

Figure 3.47: Current-voltage curves for helium discharges.

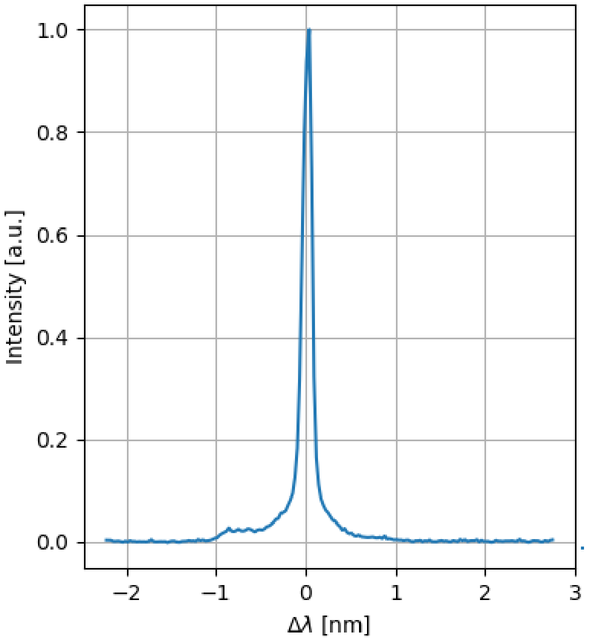

Figure 3.48: Typical He spectrum acquired during the discharge.

was done for several values of ϕ.
Moreover,the composition of helium discharges does not involve molecular species, therefore simplifying spectra interpretation.

3.3.1 Spectral shape

The typical spectrum acquired from a helium discharge is shown in Fig.3.48. The tails that contain useful information about fast ions are roughly 2% of the central peak intensity. Fitting the peak with gaussians is challenging due to the low intensity and to the lack of a proper peaked shoulder as the one presented by hydrogen spectra.
It seems therefore more sensible to consider in this case the outer limit of the evident shoulder as a reference value in order to give an estimate of maximum kinetic energy of ions.

3.3.2 Effect of pressure and voltage

Despite being particularly weak in intensity (approximately 2% of the central peak), Doppler shifted shoulders in helium spectra visibly vary when a different voltage is applied.

Fig.3.49 shows the tails of He spectra acquired at three different values of pressure and with different applied voltages; the position where the line of sight was pointed at is a central one. While the effect of the change in applied voltage within the explored values affects very little the shape and width of the tails, increasing the pressure results in a clear narrowing of the peak. This is due both to the fact that the lower mean free path prevents the ions from accelerating for long distances and to the fact that lower pressure allows for lower applied voltage.
In particular, in order to give a quantitative evaluation of such variation, since fitting the peak with gaussians does not yield satisfactory results, we can consider as a reference the point where

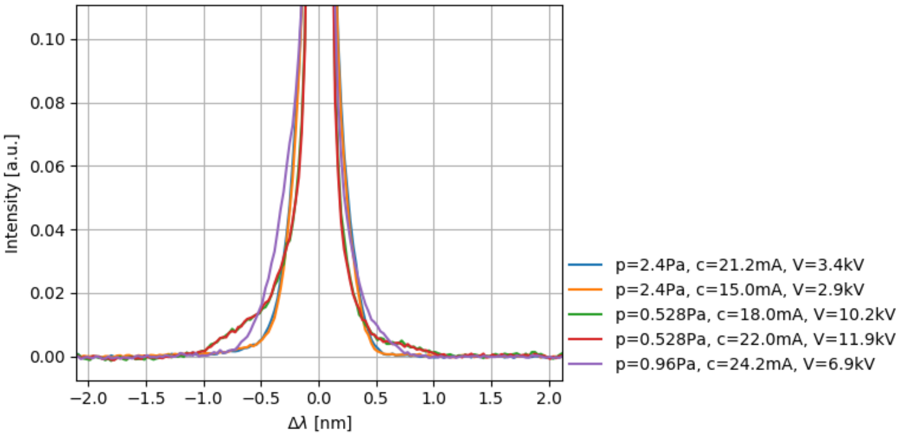

Figure 3.49: Helium spectra acquired in a central position, for different operation parametrs.

signal derivative starts rising. The obtained energy values are:

$$E_k(p = 0.53Pa) \approx 6keV \tag{3.8}$$
$$E_k(p = 0.96Pa) \approx 3keV \tag{3.9}$$
$$E_k(p = 0.2.4Pa) \approx 1.6keV \tag{3.10}$$
$$\tag{3.11}$$

All three cases show that the detected kinetic energy corresponds to $\sim 50\%$ of the applied voltage. It is therefore not possible to detect a change in behaviour due to pressure increase or decrease at this level of accuracy.

3.3.3 Vertical sweeps

The same procedure applied to hydrogen discharges was employed in this case in order to observe the presence of a microchannel in a helium discharge. Fig.3.50 shows the evolution during a vertical sweep at a very outer horizontal position. Features that can be noticed are:

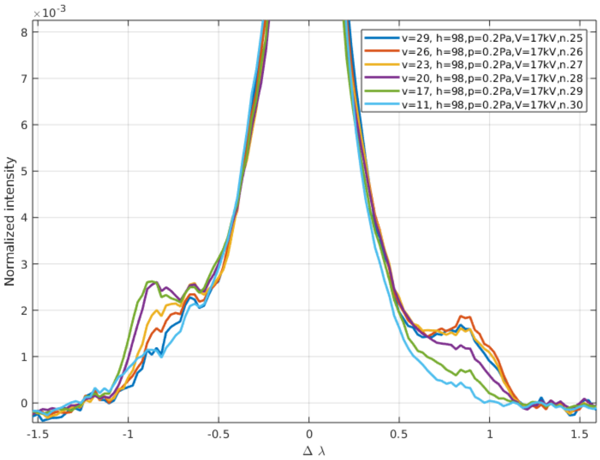

Figure 3.50: Vertical sweep for a 0.2Pa discharge.

- Blue-shifted and red-shifted shoulders are roughly symmetric with respect to the central peak;

- As the vertical position is decreased (called v in plot legend), the red-shifted component is significantly reduced.
- The same happens for the blue-shifted component as higher vertical positions are reached.

The first observation entails that particle that are moving further away from the line of sight have the same kinetic energy as the ones moving towards it.
The fact that the shifted Doppler peak seems to pass from the red-shifted side to the blue-shifted side moving in the vertical direction is an indication that the line of sight is looking at two different things. The hypothesis that is made is that such two different objects are in fact two different microchannels, as already observed with hydrogen.
The presence of growing shoulder is not detected in the same sweep done at p=2.4Pa, therefore showing that at this pressure range in helium,operating regime is no longer the star mode.

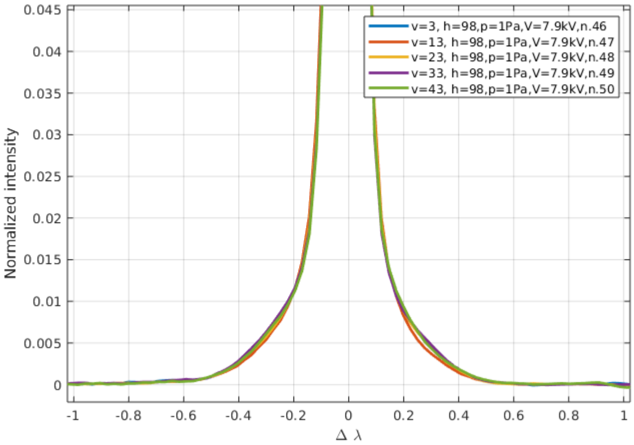

Figure 3.51: Vertical sweet on a 1Pa discharge. No shoulder is visibly present.

3.3.4 Horizontal sweeps

Having established the soundness of geometrical interpretation, it is worthwhile looking into the spectra corresponding to a movement along a microchannel. The same software that provided Fig.3.24 can calculate the angle between LOS and microchannel and the distance from the centre.
Fig.3.52 shows the evolution of the spectrum as the line of sight is moved outwards; the spectra are normalized, so that it is easier to compare the growth of the shifted component. As it was already observed with hydrogen discharges, the further from the cathode grid, the more intense is the Doppler-shifted shoulder, at both operation parameters. Moreover, once again the peak becomes narrower as the line of sight is moved inwards, although more refined measurements in the centre are not provided.
As discussed before, the impossibility to fit properly the peak does not allowan accurate enough determination of the particle kinetic energy to show the narrowing of the peak, therefore the present section will close with just a qualitative reproduction of the same trend as shown for hydrogen.

3.4 Summary

An optical apparatus was built, able to provide control on the angular position within 1° and 0.3° for the vertical and horizontal position respectively.
Calibration and identification of microchannels in star-mode operation with hydrogen was ac-

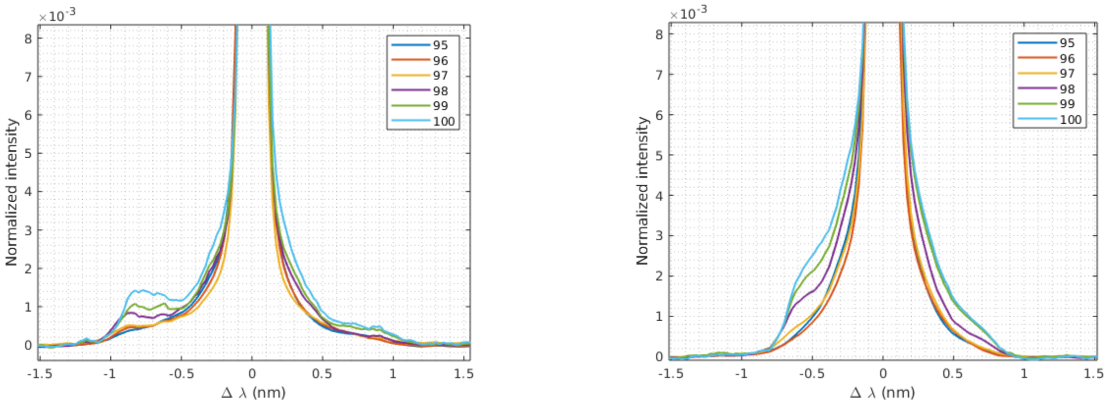

(a) Helium spectra acquired at different horizontal positions, at p=0.48Pa, V=12.7kV,I=20.2mA.

(b) Helium spectra acquired at different horizontal positions, at p=0.72Pa, V=7.8kV,I=20.2mA.

Figure 3.52: Horizontal sweeps in an helium discharge at two different sets of operation parameters.

complished in a range of pressure between 0.3 and 1.5 Pa. Measurements at higher pressure showed glow-like behaviour, not showing any relevant Doppler-shoulder.

The relationship between the calculated kinetic energy of ions and applied potential was determined, showing that kinetic energy is $\sim 40\%$ of the applied voltage (Fig.3.19).

The same analysis conducted at a central position shows a less clear behaviour.

Evolution of the ion kinetic energy with the line of sight closer to the centre showed a clear decrease of such quantity inside the cathode grid, though spatial resolution did not allow to present finer measurements. The most prominent feature of the peaks far away from the cathode was the blue-shifted shoulder. The energy of neutrals in such region was almost constant and $\sim 40\%$ of the applied potential, though at higher pressure, such fraction lowers to $\sim 30\%$. Conversely, kinetic energy detected in the centre was $\sim 30\%$ for low pressures and decreases as such parameter is increased.

Fast ion composition $(H_{2.5}^{+} - H^{+})$ was determined to be $\sim 90\% - 10\%$ agreeing with previous studies.

The fraction of dissociated hydrogen in the discharge was estimated as the ratio between the number of collected photon in the Fulcher band and the number of collected photons in the Balmer-γ peak. The dissociated fraction was $\sim 5\%$.

The feature that must be explained are the decrease in kinetic energy in the centre, the almost constant value outside and the prominent blue-shifted component.

It is perfectly possible for a neutral atom to move outwards, as it is not constrained by the potential. If such neutral has a kinetic energy of the order of several keV, then it must be born through a charge exchange of ions with the background gas. Thus, if they are moving outwards and there is no potential hill inside the cathode, they must be born from ions moving inwards on the opposite side of the cathode grid, which undergo charge exchange before crossing the centre. Let it be supposed that such neutral is born in an excited state: for us to detect its photon as far as 12cm from the cathode centre, it is necessary that it survives for such a long distance without de-exciting.

From Chap.2 it is known that the longer lifetime belongs to electrons excited to the $3s$ state. The radiative lifetime of the $3s \rightarrow 2s$ is roughly 160ns. For neutrals having energy as great as $2keV$, as in our case, the distance travelled would be of roughly 20cm: although this could justify their presence on the measured position, the associated component would not display a well-visible peaked velocity, nor it would exhibit increase in relative intensity with moving the line of sight at outer positions, also considering that $3s - 2s$ transition is only one of the three possible channels that produce H_α emission.

Another reaction that must be taken into account is the possibility for fast H to be excited due to collision with the background gas, as measured by Williams et al.[46]. In this case, however,their energy would be distributed from a minimum of 0 and a maximum related to the applied potential.

Let us now make the hypothesis the a potential hill is present inside the cathode; in this case, fast ions with a kinetic energy higher than such potential will keep ionizing background gas inside the cathode, as shown by the simulation. Most of ions in the core will be room-temperature ions. The ions that are travelling with a lower kinetic energy will be bounced back by the barrier. If those were the only ones responsible for the blue-shifted shoulders,then still, there is no reason to believe that the emission should show a peak, as they will have any value of kinetic energy between the potential of the position they were born in and the lower value of potential. There is, however, the possibility that slow room-temperature ions in the core diffuse out of the central region and roll down the potential. They start from a very specific position, therefore considering the charge-exchange mean free path, they are, for the most part, accelerated for a fixed distance, therefore reaching a peaked velocity before creating a fast H^*. This could explain the peaked spectra and also the fact that the kinetic energy associated to such shift does not change with the movement of the line of sight. The mean free path for charge exchange at the operating parameters is 4cm, which is in accord with the given explanation.

The magnitude of the virtual anode capable of causing such behaviour must be at least equal to the calculated kinetic energy, therefore in the present case, that would be $\sim 40\%$ of the applied voltage. Significant variation due to current increase cannot be established,as the change in virtual anode height is within the statistical error. More relevant change is detected with pressure variations: higher pressure, but constant current cause decrease in virtual anode height (with respect to the actual applied voltage).

What about the red-shifted component? Outside the cathode grid,it is expected for the red-shifted shoulder to narrow down as the line of sight is moved at further positions; inside the cathode, the potential hill will slow down inward moving particles,therefore narrowing once again the spectrum. However, one must consider that, unlike diverging ions, which have a very specific region of creation, according to the Abnormal Hollow Cathode model, inward moving ions are born at any position in the vessel, therefore they may acquire any value of kinetic energy before undergoing charge exchange. The observed result is constant kinetic energy for converging ions, which cannot be explained by considering the mean free path for charge exchange, as such assumption would lead to decrease in the acceleration with an increase of pressure, which is not observed.

The fact that they are accelerated by $\sim 35\%$ of the potential could link them to the possiblity that another microchannel is observed and therefore contributes to the creation of the bump which is fitted with the gaussian function; in fact, previous studies did not try to acquire information from such component and though the blue-shifted peak shape is in accord with what was found from this work, the red-shifted shoulder seems somehow off. Vertical sweep show the growth of such contribution as the line of sight is moved vertically, therefore indicating that such possibility cannot be excluded. Moreover, the fact that the red-shifted shoulder does not manifest the same jump in kinetic energy could be due to the imprecise fit linked to the low intensity of such contribution. In fact, changing the initial parameters of the fit algorithm leads to shifts in the position of such peak.

The innermost peak showed by the spectra behaves as being part of the same population creating the rest of the shoulder, as its intensity and position varies accordingly.

Measurements with helium do not show such a variety of peaks as hydrogen, although, since it was not possible to fit the spectrum with 3 gaussian components, it is possible that the identified innermost peak in hydrogen discharges is actually part of the extended shoulder. Overall, despite the simplicity in modelling it, helium did not simplify the experimental analysis, but rather made it harder due to the low intensity of the Doppler shifted shoulders.

The ratio between the shift of the innermost peaks of the hydrogen spectra and the peak associated with H^+ showed that the mass could be compatible with OH^- impurities. How such impurity may lead to shifted H_α emission is not clear. The fact that the peak shows increasing kinetic energy as the line of sight is moved away from the centre could be an indication that the particle is negatively charged, while its presence in the 4Pa discharge entails that the process is not related to microchannel formation.

Summarizing, the simulation will have to answer at least the question: is it possible to get a spectrum similar to the experimental one without the hypothesis of a virtual anode? The features of the spectrum that must be reproduced are the presence of a peaked velocity, the decreasing of kinetic energy in the centre and the dominance of diverging fast neutrals.

Secondly, it will be necessary to establish the physical mechanism behind virtual anode formation.

Chapter 4

PIC simulation

With the aim of understanding what the shape of the measured spectrum depends on, it has been necessary to simulate the evolution and stabilization of the discharge in the spherical fusor. In order to simulate the discharge, a Particle-In-Cell code was used.
The aim of the simulation is at least to provide the density profiles of the different species in use and derive self-consistently the shape of the potential.
Since the studied system contains a very large number of particles, following the motion of every single particle is computationally not efficient.
Particle-In-Cell simulations are constituted of 5 basics steps:

1. Charge of particles is projected onto the mesh.
2. Electric potential is calculated from integration of Poisson's equation.
3. Electric field is calculated from the potential in order to derive Lorentz forces.
4. Particles are moved under the action of Lorentz force.
5. Particle collisions are processed.

The geometry used for the present work is 2D, exhibiting a circle with $r = 20cm$, with a grid spacing $\Delta X = \Delta y = 0.05mm$, chosen in order to satisfy $\Delta x \leq \lambda_D$, where λ_D is the Debye length. The chosen time step is $100ps$ and was imposed to get $\Delta t < \omega_{pe}^{-1}$, where ω_{pe} is the plasma frequency.
The inner grid was modelled with six square regions arranged on a circle of $r = 2.5cm$.

4.0.1 Charge projection

When using a Particle-In-Cell simulation, every macroparticle can occupy any position in space. On the other hand, fields are calculated on discrete mesh points. Since electrostatic potential can be calculated only if the charge space density is known, the necessity of mapping charge density on the mesh from macroparticle position emerges.
The method that was used for the PIC code employed in this thesis is the Cloud In Cell (CIC) scheme. Referring to Fig.4.1, one can understand the idea behind the CIC method; consider a macroparticle placed in between four mesh points: it represents N real particles, so the challenge is to determine what fraction of such N particles will contribute to the charge density in point A,B,C or D respectively. CIC estimates such fraction as proportional to the areas in which the square grid element is divided into.

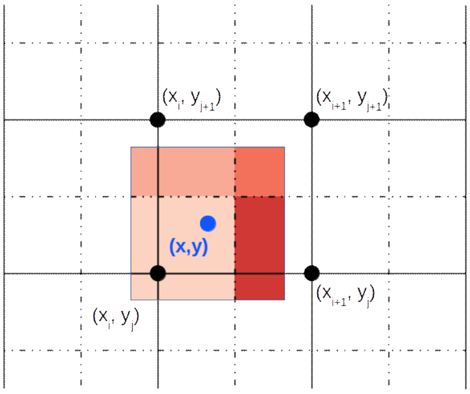

Figure 4.1: Depiction of the Cloud-In-Cell method.

In formulas:

$$\begin{cases} \rho_{i,j} & = q\frac{(x_{i+1}-x)(y_{j+1}-y)}{\Delta x \Delta y} \\ \rho_{i+1,j} & = q\frac{(x-x_i)(y_{j+1}-y)}{\Delta x \Delta y} \\ \rho_{i,j+1} & = q\frac{(x-x_i)(y-y_j)}{\Delta x \Delta y} \\ \rho_{i+1,j+1} & = q\frac{(x_{i+1}-x)(y-y_j)}{\Delta x \Delta y} \end{cases} \tag{4.1}$$

Where (x_i, y_j) are the coordinates of the mesh points and (x, y) are the particle coordinates; q is the macro particle charge (its weight multiplied by the electric charge of the particle it represents) and $\Delta x \Delta y$ is the area of the cell.

4.0.2 Solution of Poisson's equation

The value of electrostatic potential in the machine is calculated by solving the Poisson's equation on the discrete mesh points. The discretized version of Poisson's equation has the form:

$$\frac{\Delta^2 \phi_{i,j}}{\Delta^2 x} + \frac{\Delta^2 \phi_{i,j}}{\Delta^2 y} = -\frac{\rho_{i,j}}{\epsilon_0} \tag{4.2}$$

where the following definitions were used:

$$\begin{cases} \frac{\Delta \phi_{i,j}}{\Delta x^2} & = \frac{\phi_{i+1,j} - 2\phi_{i,j} + \phi_{i-1,j}}{\Delta x^2} \\ \frac{\Delta \phi_{i,j}}{\Delta y^2} & = \frac{\phi_{i,j+1} - 2\phi_{i,j} + \phi_{i,j-1}}{\Delta y^2} \end{cases} \tag{4.3}$$

Assuming that grid spacing is the same in all directions, Poisson's equation can be rewritten as:

$$4\phi_{i,j} - \phi_{i+1,j} - \phi_{i+1,j} - \phi_{i+1,j} - \phi_{i+1,j} = \frac{\rho_{i,j}\Delta x^2}{\epsilon_0} = b_{i,j} \tag{4.4}$$

(4.4) can be cast in matrix form as:

$$\mathbf{A}\mathbf{x} = \mathbf{b} \tag{4.5}$$

where $\mathbf{x}$ and $\mathbf{b}$ are defined as:

$$\mathbf{x} = \begin{pmatrix} \phi_{1,1} \\ \phi 1, 2 \\ \vdots \\ \phi 1, n \\ \vdots \\ \phi m, n \end{pmatrix}, \qquad \mathbf{b} = \begin{pmatrix} \phi_{1,1} \\ \phi 1, 2 \\ \vdots \\ \phi 1, n \\ \vdots \\ \phi m, n \end{pmatrix} \tag{4.6}$$

In order to solve (4.5), generalized minimum residual (GMRES) iterative method was used, which solves the system by minimizing the function:

$$f(\mathbf{x}) = \frac{1}{2}|\mathbf{Ax} - \mathbf{b}|^2 \tag{4.7}$$

4.0.3 Electric field

The electric field can be calculated by solving the discretized form of

$$\vec{E} = -\nabla\phi \tag{4.8}$$

As in our case the potential does not vary along z direction, the only components of the electric field are along x and y direction:

$$\begin{cases} E_{x,i,j} = \frac{\phi_{i+1,j}-\phi_{i-1,j}}{2\Delta x} \\ E_{y,i,j} = \frac{\phi_{i,j+1}-\phi_{i,j-1}}{2\Delta y} \end{cases} \tag{4.9}$$

The electric field calculated from Eq.4.9 represents its value on a single node. In order to know the exact value of the electric field on the single particle, it is necessary to interpolate it to the exact position of the particle, using the electric field on the surrounding nodes. In particular, bilinear interpolation was used:

$$\begin{cases} E_x = E_{x,i,j}\frac{(x_{i+1}-x)(y_{j+1}-y)}{\Delta x\Delta y} + E_{x,i+1,j}\frac{(x-x_i)(y_{j+1}-y)}{\Delta x\Delta y} + \\ \qquad E_{x,i,j+1}\frac{(x_{i+1}-x)(y-y_i)}{\Delta x\Delta y} + E_{x,i+1,j+1}\frac{(x-x_i)(y-y_i)}{\Delta x\Delta y} \\ E_y = E_{y,i,j}\frac{(x_{i+1}-x)(y_{j+1}-y)}{\Delta x\Delta y} + E_{y,i+1,j}\frac{(x-x_i)(y_{j+1}-y)}{\Delta x\Delta y} + \\ \qquad E_{y,i,j+1}\frac{(x_{i+1}-x)(y-y_i)}{\Delta x\Delta y} + E_{y,i+1,j+1}\frac{(x-x_i)(y-y_i)}{\Delta x\Delta y} \end{cases} \tag{4.10}$$

4.0.4 Particle motion

Particles are moved discretely by exploiting the leap-frog method.

$$\begin{cases} \vec{v}_{i+1/2} = \vec{v}(t + \frac{1}{2}\Delta t) \\ \vec{x}_{i+1} = \vec{x}_i + \vec{v}_{i+1/2}\Delta t) \\ \vec{v}_{i+3/2} = \vec{v}_{i+1/2} + \frac{q}{m}\vec{E}\Delta t \end{cases} \tag{4.11}$$

4.0.5 Collisions

When simulating a system of moving particles it is natural to include interactions between such particles. Dealing with collisions is computationally expensive and it is therefore necessary to limit as much as possible the number of included reactions, choosing only the most probable/relevant ones for the phenomena that are interesting to observe.

Another way of reducing the cost of collision processing in a PIC simulation is to use a Monte Carlo Collision scheme, which avoids dealing with binary collisions.

MCC consists in evaluating the probability for each particle to undergo a certain reaction and rejecting or accepting such collision by extracting a random number.

Usually, the collisions a certain particle can undergo are more than one, let us say they are N; if the particle energy is:

$$E_i = \frac{1}{2}m(v_{ix}^2 + v_{iy}^2 + v_{iz}^2) \tag{4.12}$$

then the total collision cross section is given by

$$\sigma_T(E_i) = \sigma_1(E_i) + ... + \sigma_N(E_i) \tag{4.13}$$

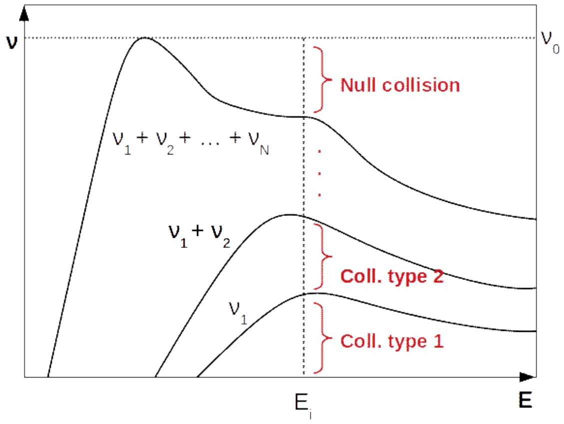

Figure 4.2: The addition of the null collision process results in a constant collision frequency over all energies [45].

The probability for the $i-th$ particle to collide with the target species must be proportional to the distance that such particle has travelled according to the formula:

$$P_i = 1 - exp(-v_i \sigma_T(E_i) n_t(x_i) \Delta t) \tag{4.14}$$

where $n_t(x_i)$ is the local density of the target species; if the target species is also the background gas, then the density can be considered as uniform in space.
Once P_i is determined, a random number uniformly distributed in the interval $[0, 1]$ is extracted and if such number is less than P_i, the collision takes place; another extraction is then necessary to determine which of the processes is happening.
Up to now it is still necessary to calculate P_i for every particle, even for those not taking part in any collision: this is computationally a waste of time. As suggested by Vahedi [45], it is possible, however, to avoid such step by introducing the so called *null collision*, with a frequency ν_0 such that

$$\nu_0 = n_t \max_E(\sigma_T v) \tag{4.15}$$

In practice, a process was added such that at each value of energy, the probability of undergoing a collision is equal to 1; in other terms, a fake reaction was added that allows for the total collision frequency to be equal to its maximum at every value of energy. Fig.4.2 makes the concept visually clearer.
The particles that will be tested for the type of collision are then a fraction of the total number equal to

$$P_{null} = 1 - exp(-\nu_0 \Delta t) \tag{4.16}$$

Once they are chosen, a random number, R, is extracted and the type of collision is selected in the following way

$$R \leq \nu_1(E_i)/\nu_0 \qquad \text{Collision type 1} \tag{4.17}$$

$$\nu_1(E_i)/\nu_0 < R \leq \nu_1(E_i)/\nu_0 + \nu_2(E_i)/\nu_0 \qquad \text{Collision type 2} \tag{4.18}$$

$$\vdots \tag{4.19}$$

$$\sum_{j=1}^{N} \nu_j(E_i)/\nu_0 < R \qquad \text{Null collision} \tag{4.20}$$

4.1 Collisions

Choice of included reactions is crucial to achieve stable operation conditions, as they make up the equilibrium between sources and losses of particles.

Ions can be created through several channels.

Background gas ionization due to impact of electrons, other ions or fast neutrals is the main source of H_2^+ atoms; as a reference, Fig.4.19 shows the contribution to the source function of several reaction channels as a function of the distance from the centre. On the other hand, birth of H^+ can be caused by dissociative ionization of background gas (due to electron impact) or by double electron detachment from H^- anions, the former being the most relevant process. Moreover, adding also the 5% of atomic hydrogen to the background, H^+ can also be created by direct ionization due to impact of electrons or other ions. Fast neutrals, referring both to H_2 and H are the product of charge exchange reactions between ions and background gas. They are relevant in the overall balance, as they contribute to ionization reactions; not taking them into account would result in an energy sink in the model, leading to discharge fading out.

Finally, electrons are born from ionization reactions. Multiplication of the number of electrons is provided by electron-impact ionization or dissociative ionization of background gas. They are also emitted from the cathode surface as secondary electrons due to ion impact.

Losses of particles are caused both by reactions and by boundary conditions. The latter meaning that any particle that reaches the outer wall or the inner cathode structure is lost. As for the losses due to particle collisions, ions may be lost through charge exchange reactions, which are considered to be a major problem in fusors, limiting the confinement of fast ions.

Ion-electron pairs are lost through recombination reactions; since they are binary reactions, they were implemented using a different kernel with respect to the previously mentioned collisions.

Cross section for particle-background collisions are shown in Appendix A. The choice of the reactions was inspired by previous computational works [34] [35] and by the collisions contained in ALADDIN Database [1] and in Barnett's Red Book [5].

Ionization due to electron impact Ionization due to electron impact causes scattering of primary electron, birth of secondary electron and birth of an ion.

Energy of incident electron is given by:

$$E_{e,scat} = E_{e,inc} - E_{ion} - E_{e,ej} \tag{4.21}$$

according to energy conservation. It is reasonable to assume that the newborn ion is born at room temperature, therefore the target neutral energy is not modified by electron impact.

Ionization due to ion impact Ionization due to ion impact produces one electron and one ion. The ion is produced at room temperature, while energy of the ejected electron depends on the projectile energy according to Rudd distribution [39].

Given the incident proton energy E_p, the secondary electron energy W, the number of electrons in the target atom N and the electron binding energy I, it is possible to express the energy distribution of the ejected electron as a function of the normalized electron energy $w = W/I$ and of the reduced projectile velocity $v = \sqrt{T/I}$ ($T = E_p m_e/m_p$):

$$\sigma(w) = \frac{S}{I}\frac{F_1 + F_2 w}{(1+w)^3\left[1 + e^{\alpha(w-w_0)/v}\right]} \tag{4.22}$$

where $S = 4\pi a_0^2 N(R/I)^2$, with a_0 being Bohr radius and R is the Rydberg energy.

All the parameters in Eq.4.22 depend on v and on the target atom.

The direction of the emitted electron is given by Vahedi [45]:

$$\vec{v}_{scat} = \vec{v}_{inc} cos(\chi) + \vec{v}_{inc} \times \hat{i}\frac{sin(\chi)sin(\phi)}{sin(\theta)} + \vec{v}_{inc} \times (\hat{i} \times \vec{v}_{inc})\frac{sin(\chi)cos(\phi)}{sin(\theta)} \tag{4.23}$$

where θ is determined as $cos(\theta) = \vec{v}_{inc} \cdot \hat{i}$, ϕ is uniformly distributed in $[0, 2\pi]$ and is chosen randomly, while

$$cos(\chi) = \frac{2 + E_{inc} - 2(1 + E_{inc})^R}{E_{inc}} \tag{4.24}$$

Dissociative collisions Dissociative collisions allow production of hydrogen ions and atoms. They may happen due to either electron or heavy particle impact with molecular hydrogen.
Any dissociation reaction causes as an intermediate step the formation of molecule excitation to unbound states. The case of electron impact dissociation was already treated in Chap.2 in the particular case of production of H in an excited state. As observed by Higo [17], atoms produced by dissociation due to electron impact, present a translational energy peaked at 0 and 8eV; such peaked energies are caused by direct dissociation or pre-dissociation through the ${}^2\Sigma_g^+(1s\sigma_g)$ of H_2^+ (0 peaked energies) or ${}^2\Sigma_u^+(2p\sigma_u)$ (8eV peaked energies).
Similarly, dissociative ionization of the hydrogen molecules results in the fragments sharing equally the excess energy after the reaction; Kieffer [23] showed a peaked distribution around 8eV, considering predissociation through the ${}^2\Sigma_u^+$ state to be the major contribution.
The electrons resulting from electron-impact dissociative ionization of H_2 share the excess energy $E_0 - E_i$; calling W_1 and W_2 their kinetic energies, one expects that the energy distribution of the single electron is symmetric around $(E_0 - E_i)/2$, as shown by Cristophorou [7].
Summarizing, fragment energy in the simulation is sampled around 8eV, while electron energy is sampled from the distribtuion proposed by Cristophorou.

4.1.1 Secondary emission from cathode grid

Modelling of the secondary emission was necessary, as electron sources are vital for the discharge. Secondary electrons are emitted from a solid surface under impinging of heavy ions through two processes.
Potential secondary emission occurs if the potential energy of the heavy ion is at least twice the work function of the surface material and consists in the emission of an electron by resonance neutralization, followed by Auger deexcitation or bu Auger neutralization [16]. Secondary emission coefficient for potential emission is given by:

$$\gamma = 0.032(0.78E_i - 2\phi) \tag{4.25}$$

where ϕ is the material work function, while E_i is the ion kinetic energy.
If emitted electrons are excited inside the solid by transfer of kinetic energy from the impinging ion, the process is called *kinetic electron emission*. Modelling the secondary emission coefficient in this case was done considering [2] and [16], which show evidence that such coefficient generally depends linearly on projectile velocity. Kinetic electron emission is a threshold process; as Baragiola argues, using the free-electron model for metals, due to the strong mismatch of electron and ion mass, the maximum transferred energy is obtained when en electron moving at the Fermi velocity antiparallel with respect to the impinging ion is scattered to a state with momentum parallel to the projectile; such energy is given by $E_{max} = 2mv(v - v_F)$ where v is the final energy , m the mass of the electron and v_F the Fermi velocity. The minimum projectile velocity that could cause the electron emission corresponds to the case where $E_{max} = \phi$, where ϕ is the metal work function. The threshold velocity is therefore:

$$v_{th} = \frac{1}{2} v_F \left[\sqrt{1 + \frac{\phi}{E_F}} - 1 \right] \tag{4.26}$$

The secondary electron yield is predicted to vary with respect to the impact angle as:

$$\gamma(\theta) = \frac{\gamma(0)}{cos(\theta)} \tag{4.27}$$

where $\gamma(0)$ is the emission coefficient at normal incidence.
The ejected electron energy was modelled to follow the general behaviour showed by Hasselkamp [16] for H^+ impact on different metals and it is stated that secondary electron energy distribution is not significantly affected by projectile energy for light ions; energies of emitted electrons span from $0eV$ to $\sim 20eV$. The exact distribution function is not gaussian, but energies were sampled using such distribution, because it is assumed that minor mistakes in such choice would not affect the simulation in an evident way. The maximum of the distribution is set at 3.4eV and the FWHM was set at 11eV, according to the data shown in [16] for impact of H^+ on Ti.

4.1.2 Recombination

What was clear from first simulations is that a very high density of low energy electrons builds up inside the cathode grid. Such electrons are found to move inside such region, rarely exiting. This produces two effects: build-up of negative charge inside the cathode grid prevents the virtual anode from showing, since such charge density neutralizes positive charge density due to oscillating ions and a reduced rate of electron-impact ionization of background gas outside cathode grid.
On the other hand many slow ions accumulate in the center as well, making a neutralization process necessary. The neutralization process is :

$$e + H_2^+ \rightarrow H_2(slow) \tag{4.28}$$

The cross section for such reaction is shown in Fig.4.3. The reaction cannot be implemented

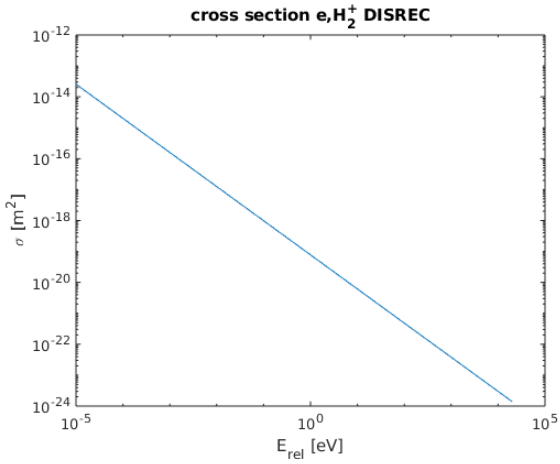

Figure 4.3: Recombination cross section.

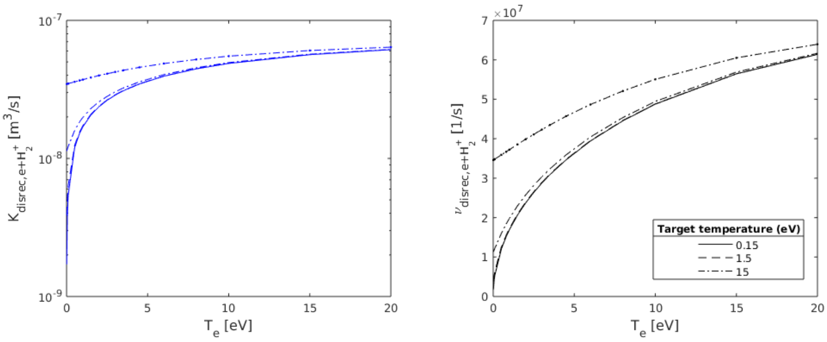

Figure 4.4: Recombination reactivity and rate.

in the Monte-Carlo scheme for reactions in the PIC code; the idea is to neglect one of the two particles' velocity, calculate the rate coefficient, assuming gaussian distribution for the projectile energy and then evaluate the probability of such reaction by multiplying the rate coefficient by the dt of the simulation. The rate coefficient is calculated as:

$$K_{e,H_2^+} = \frac{1}{\sigma v_e n_{H_2^+}} \tag{4.29}$$

in Eq. 4.29 it is implicit that the target is considered to be H_2^+. This is done because for low values of electron temperature, the target velocity does not affect the rate coefficient significantly. At each time-step the probability for the selected electron to undergo neutralization is calculated as $K_{e,H_2^+}dt$; if the extracted random number r is smaller than such probability, the electrons is considered to be neutralized, while a random H_2^+ in the same cell was selected to be eliminated. Another process that should be inserted in the simulation to limit the accumulation of electrons inside the cathode grid is energy transfer from fast electron to slow accumulated electrons. Fast electrons may come as secondary electrons from cathode wires: in fact, they may gain enough kinetic energy due to the potential structure near the wire.

4.2 Diagnostics

4.2.1 Spectrum

In order to acquire an artificial emission spectrum from the chamber it is necessary to determine which particles can emit photons, what wavelength to concentrate on, where such photon will be emitted and at what velocity will the particle emit it.
Excited H that emit the collected light may be either fast or slow, therefore producing a Doppler-shifted spectrum. Detailed description of the reactions creating fast and slow excited hydrogen atoms is contained in Sec.2.
The reactions in [46] indicate the relevance of excitation of H projectiles, which was also added to the reactions producing excited H.
Every time a neutral $H*$ is born, it is saved in a list along with its position and velocity.
Considering the spectroscopic measurements are done with an exposure time of tens of seconds, the lists from many time steps are merged together.
In order to build the spectrum, a line of sight is decided and the particles inside such line of sight are selected. The emitted wavelength is then calculated using Eq. 2.2. In our case, we consider the line of sight as lying on the same plane as the simulation, therefore z component of velocity will not have any projection on the line of sight.

4.2.2 Current

The current collected by the cathode grid structure can be obtained upon counting how many electrons are emitted (N_e) and how many ions are collected ($N_{i,x}$) in a time step and converting the measure using the macro-particle weight (MPW=$2 \cdot 10^6$) in the following way:

$$I = \frac{MPW \cdot (N_e + \sum_{x=1,2,3} N_{i,x})e}{\Delta t} \tag{4.30}$$

Now, it must be considered that such current may be compared to the one obtained experimentally only using a conversion factor equal to the ratio between the volume occupied by the cathode grid in reality and the volume occupied by the simulated wires. Such conversion factor in the present case is 0.011.

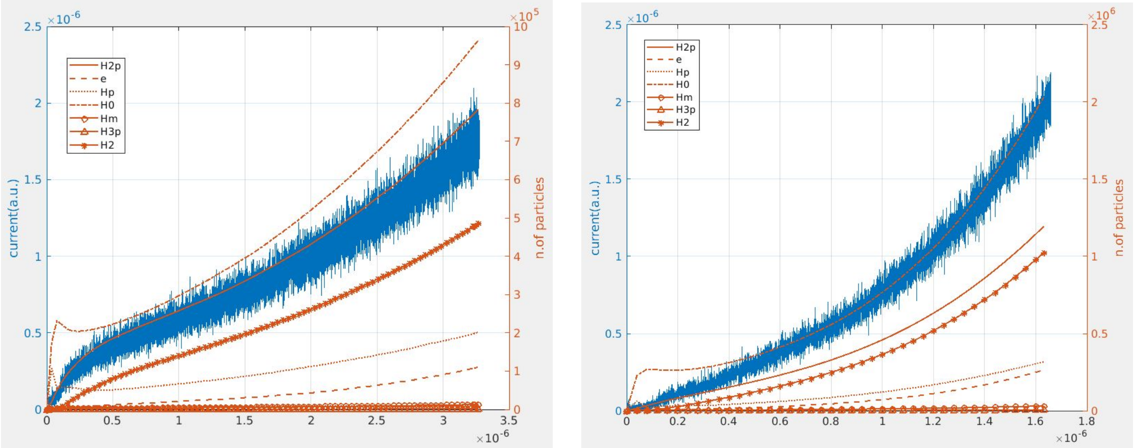

(a) p=0.5Pa, V=80kV.

(b) p=1Pa, V=50kV.

Figure 4.5: First microseconds of two discharges at different pressure and applied voltage.

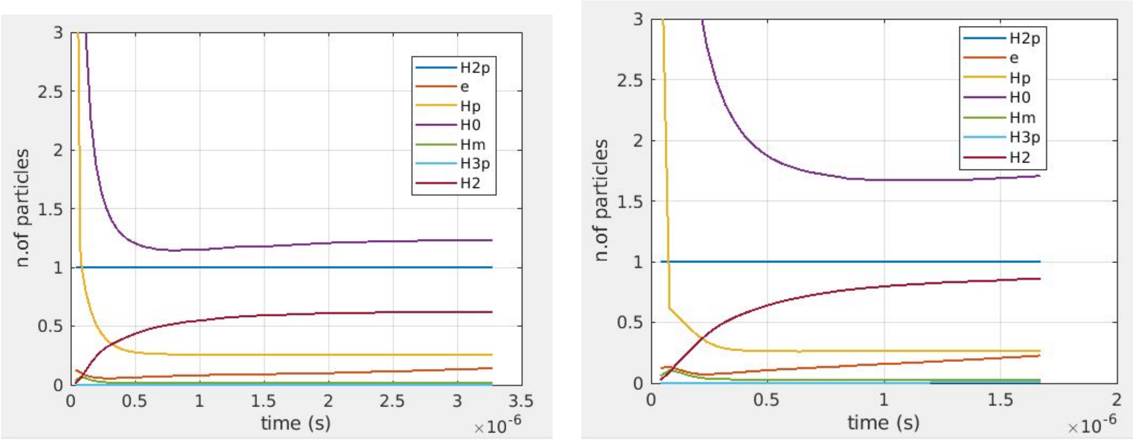

(a) p=0.5Pa, V=80kV.

(b) p=1Pa, V=50kV.

Figure 4.6: Ratio between particle number and number of H_2^+ ions.

4.3 Results

4.3.1 Discharge initiation and current

Fig.4.5 shows how number of particle and current evolve in the first instants of the discharge. The first thing that can be noticed is that the discharge at higher pressure exhibits a higher growth rate of both current and particle number; this was also shown by Osawa et al.[35] and is due to the lower ionization probability due to lower target density.

Secondly, as shown by Fig.4.6, the fraction of fast H_2 and H with respect to the H_2^+ population is clearly increased as the pressure is increased. Since fast neutrals are born from charge exchange reactions with background gas, if background density is significantly increased, it is natural that the number of fast neutrals would increase.

Another relevant feature of the first instants is the fact that the growth of both particle number and current is exponential, as an avalanche multiplication mechanism sets in. In an experimental discharge such increase is limited by the presence of a ballast resistor. In order to achieve a stationary condition, a virtual ballast was therefore inserted in the simulation.

In practice, the current is averaged over 100 time steps, then its value is used to regulate the

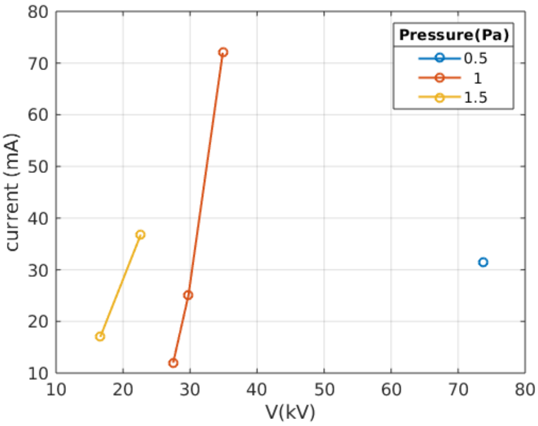

Figure 4.7: Current-voltage characteristics of simulated discharges.

potential on the cathode wire using the relation:

$$V_{wire} = V_0 - RI \tag{4.31}$$

where V_0 is the reference value initially applied (experimentally, that would be the voltage provided by the power supply), V_{wire} is the voltage on the cathode wire (after the fall on the resistor) and R is the resistance value of the ballast resistor, in the present case $R = 210k\Omega$.
Fig.4.7 shows the current-voltage characteristic curves extracted from the simulation compared to measured values. The simulated points may be compared to the experimental ones in Fig.3.10; in order to obtain the same current at the same pressure, simulated discharges require an applied potential which is $\sim$ 10 times higher. One reason could be related to the fact that secondary emission does not account for the different angles of incidence of the ions, which can increase the average number of secondary electrons by a factor 10.
In order to experiment secondary emission effect on current, the $amplification$ (which will be called a from now on) factor in secondary emission formula was increased up to $\sim$ 5. Since current is made up of two terms, and only one of them is increased by $\sim$ 5, the current is expected to increase by the quantity $(a_2 - a_1)e/dt \cdot N_{ions}$, since the number of ions falling into the grid is roughly the same and assuming that for every ion, exactly a electrons are ejected. This leads to a maximum variation of current at 1Pa equal to $\sim 18mA$. A more realistic situation is shown in Fig.4.8a, current is increased by $8mA$ at 1Pa of pressure.The increase in current is a direct effect of increase of secondary emission amplification, but the total number of electrons in the vessel does not increase relevantly. This is due to the fact that most electrons are actually produced due to ionization reactions in the vessel and, as it will be shown in the next subsection, most ionization reactions occur due to heavy-particle impact, therefore increasing the emitted electrons does very little in terms of changing overall particle population.
Another modification of the code consists in adding also atomic H background. Such feature allows direct ionization of H atoms, whose cross section is one order of magnitude higher than the electron-impact ionization and dissociative ionization of molecular hydrogen. In fact, the presence of atomic hydrogen in the background gas allows a significant increase in current,due to the increased number of H^+ ions in the vessel; this is shown for a p=0.5Pa discharge in Fig.4.8b.

As shown by Fig.4.10 the current-voltage relation is definitely closer to experimental behaviour when atomic H background is introduced, as ionization of H is one order of magnitude more probable than H_2^+ ionization. Though the curves are not coincident, still the evolution with respect to pressure is reproduced.

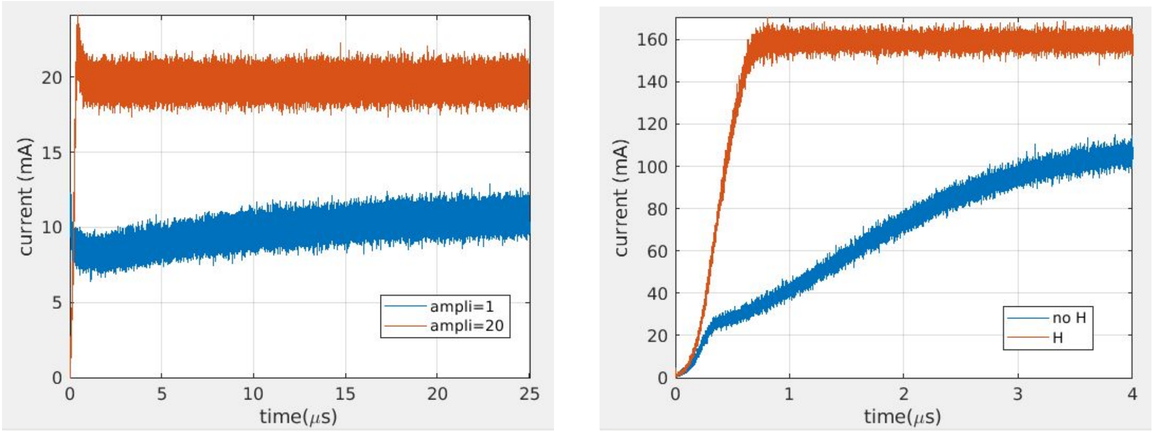

(a) Amplification.

(b) Atomic H.

Figure 4.8: Effect on current of the two different modifications.

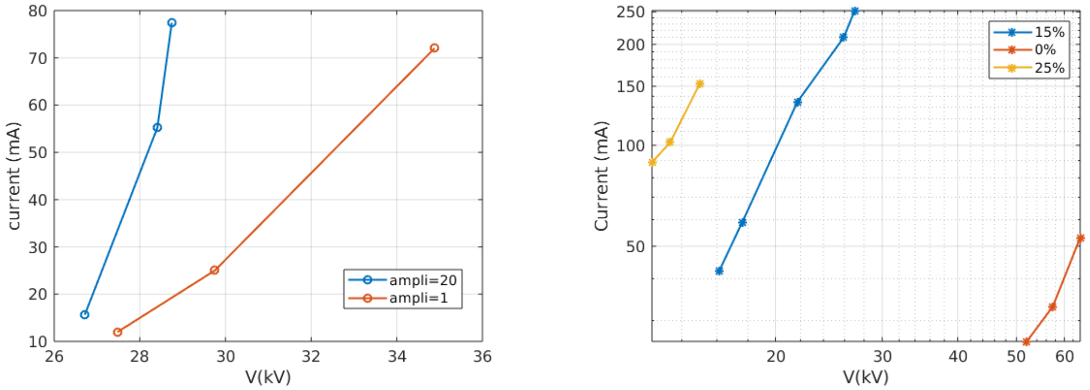

(a) Amplification variation (p=1Pa).

(b) Adding H (p=0.5Pa).

Figure 4.9: Effect on current-voltage curves of the two applied modification to the code.

Summary of the subsection Ignition and stabilization of the discharge have been achieved, the latter with the insertion of a virtual ballast regulating the applied voltage.

Difference in population was detected especially with respect to neutrals population at different pressure.

The effect of secondary emission amplification was investigated on the discharges in order to reproduce experimental results. The effect, even for unphysical values of amplification, is not as relevant as hoped, due to the dominance of ion and neutral-impact ionization rather than electron-impact ionization.

The effect of an H component to the background gas was investigated for the same reason as before and produced results closer to experimental ones. This was explained with the generally higher cross sections when it comes to H ionization rather than H_2 ionization.

Though the values are not exactly reproduced it must be noted that even in experiments, different geometry of the inner cathode grid causes different current-voltage characteristics.

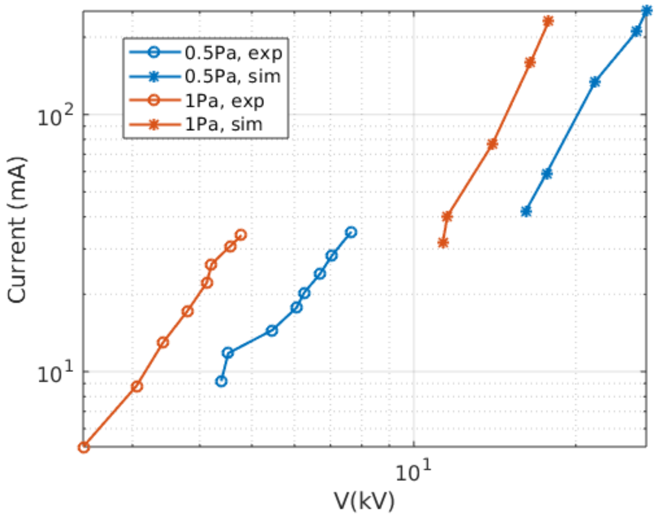

Figure 4.10: Comparison between the I-V curves obtained experimentally and the ones obtained from the simulation (with atomic hydrogen).

4.3.2 Ionization reactions

The discharge in the fusor is kept alive thanks to ionization reactions providing the source of ions and electron.

In this section the role of different reactions in the discharge is investigated. In particular, electron and H_2^+ production will be take into consideration, as H_2^+ is the most abundant species in the fusor.

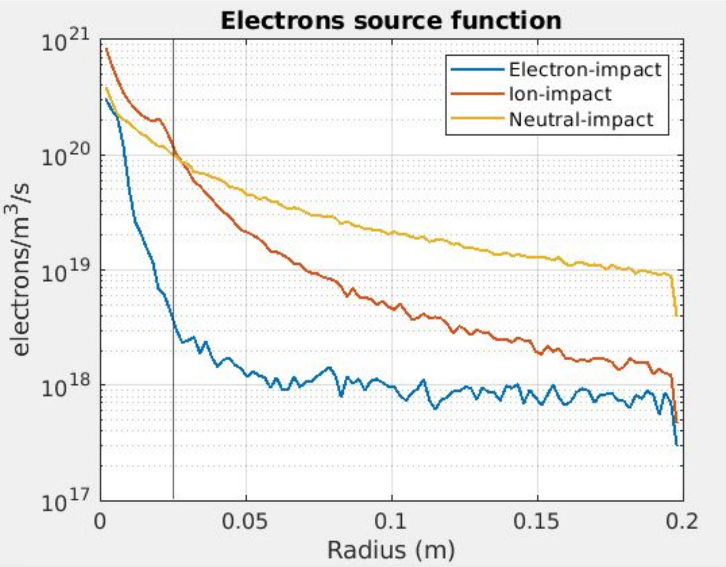

Figure 4.11: Electrons born per unit time and unit volume as a function of the distance from centre.

With respect to cathode grid position, it's possible to define two regions: one inside it and one outside it.

According to Fig.4.11 most electrons are born inside the cathode grid; this could be expected, because:

- Most particles are concentrated in the centre, where density is highest;

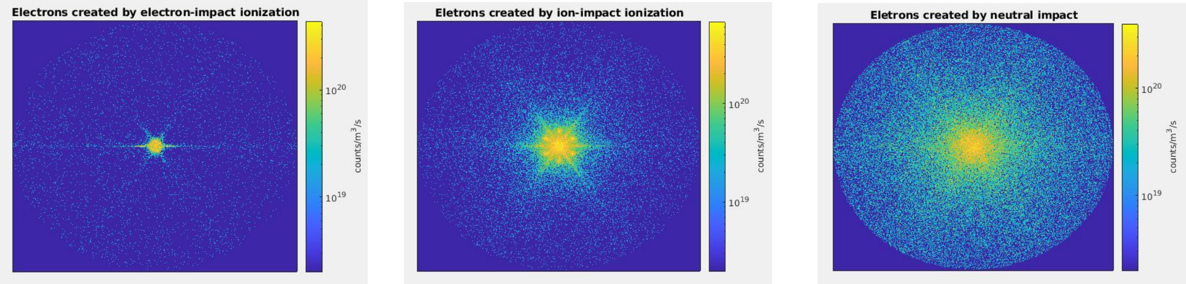

(a) Electron impact. (b) Ion impact. (c) Neutral impact.

Figure 4.12: Source generation of electrons due to different kinds of reactions, at p=1Pa and V=18kV.

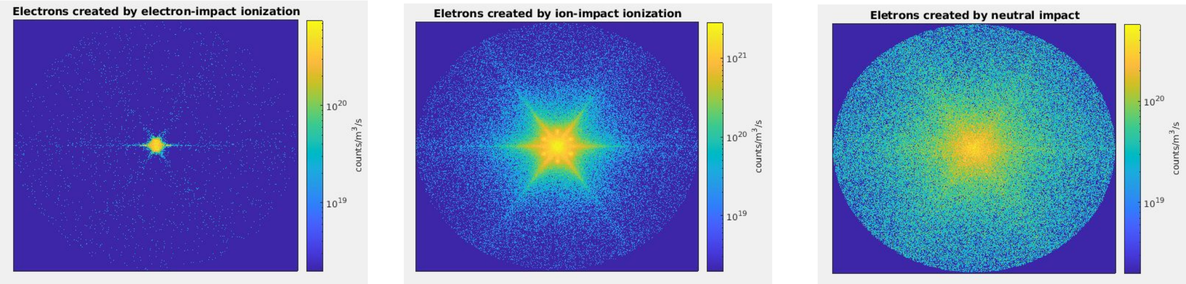

(a) Electron impact. (b) Ion impact. (c) Neutral impact.

Figure 4.13: Source generation of electrons due to different kinds of reactions, at p=0.5Pa and V=25kV.

- Most energetic particles are found in the centre, as they are accelerated by the potential well;

Ionization due to electron-impact with background gas decreases steeply outside the cathode grid; as it will be seen later, electrons in the centre have mainly energies below $500eV$, which is anyway enough to cause ionization. Since electrons born from heavy particle impact on molecular hydrogen are emitted with energy extracted from Rudd distribution (which entails energies typically below $\sim 50eV$), the only reaction which could possibly created energetic electrons is electron-impact ionization; also secondary emission from cathode wires causes electrons to the ejected towards the centre by the potential well formed around the wire.
Ionization due to ion-impact decreases less steeply with increasing radius; it diminishes due both to possible charge exchange reactions, which reduce the number of ions outside the cathode grid and due to to the decrease in kinetic energy of ions as they travel towards the walls.
Since neutrals do not suffer from the latter, neutral-impact collisions are the most relevant outside the central region, highlighting the importance of fast neutrals population for the discharge. Moreover, comparison with a discharge made at lower pressure (and necessarily higher voltage), which is represented in Fig.4.13, shows the presence of preferential channels of ionization, due to ions. This is both due to the higher applied voltage and to the higher mean free path, allowing ions to oscillate for longer trajectories inside the potential well.
Molecular hydrogen ions are the most abundant species; they are born due to ionization and charge exchange, see Fig.4.14-4.19.

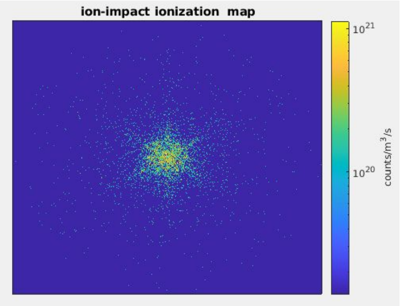

Figure 4.14: Map of ion-impact ionization on background gas.

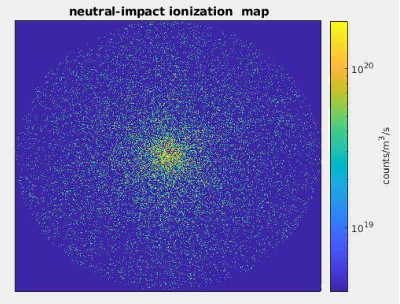

Figure 4.15: Map of neutral-impact ionization on background gas.

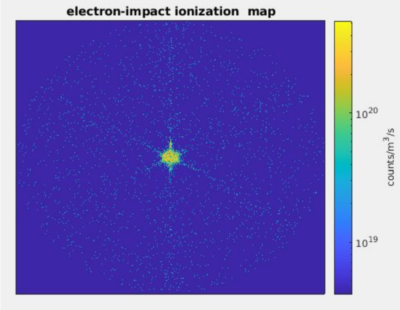

Figure 4.16: Map of electron-impact ionization on background gas.

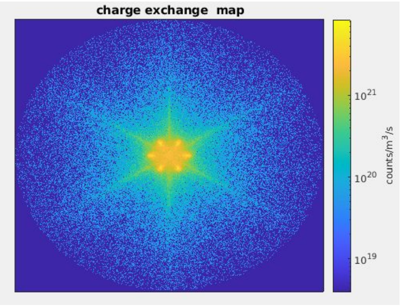

Figure 4.17: Map of charge exchange reactions.

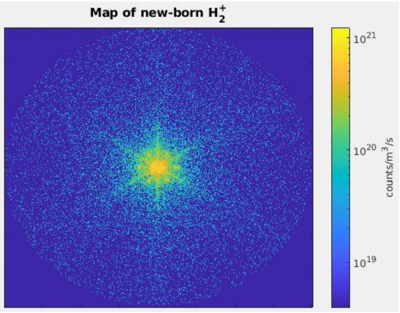

Figure 4.18: Total map of new-born H_2^+

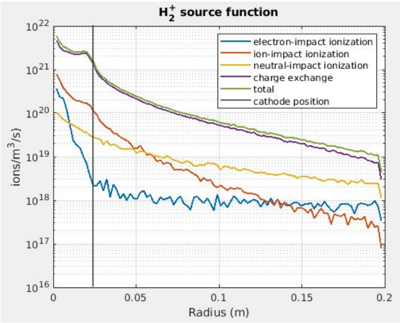

Figure 4.19: Source function for H_2^+

Most of H_2^+ ions are born inside the cathodic region, mostly due to electron and ion impact ionization reactions. Charge exchange reactions are shown, but are not relevant in the overall balance, since fast ions were born from ions, so their returning to be ions gives no net balance in favour of ion population.

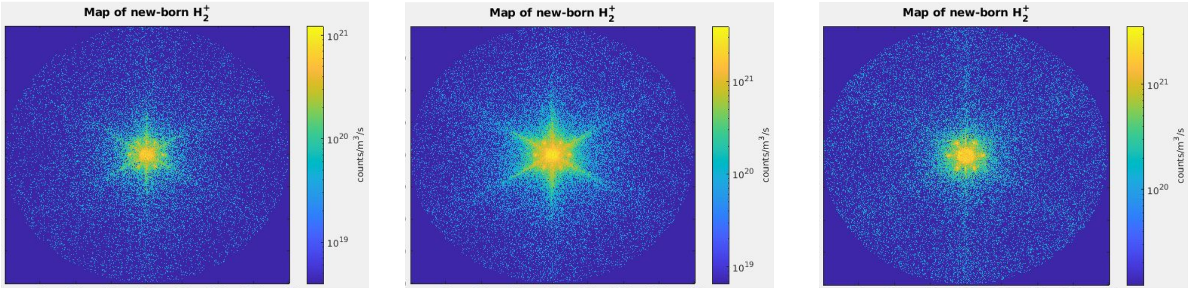

(a) p=1Pa, V=18kV.

(b) p=0.5Pa, V=25kV.

(c) p=1.5Pa, V=12kV.

Figure 4.20: Map of total new-born H_2^+ at different conditions.

As previously noted for electrons, also H_2^+ are born prevalently in the central region, where ions converge and where electrons born from other ionization reactions are trapped due to the approximately flat potential.

Both in the case of electron creation and H_2^+ creation, neutral-impact ionization shows less localization in the central area; this happens because many fast neutrals survive also outside, unlike ions, which are decelerated as they travel towards the wall.

Let us now see the effect of a variation of applied voltage on the source function for ions.

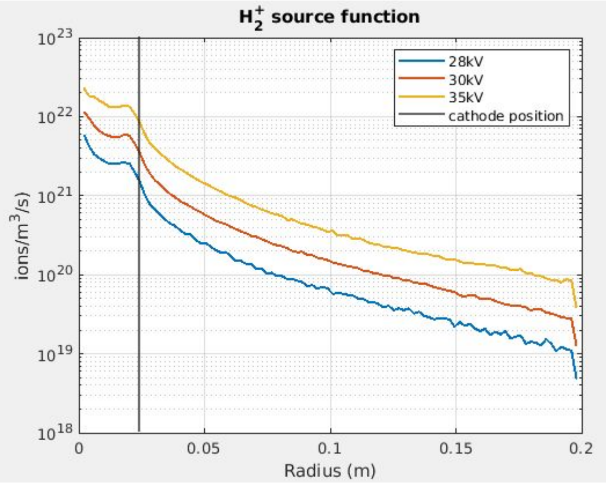

Figure 4.21: Source function at different applied voltages.

As expected, Fig.4.21 shows an increase in the number of particles born on unit volume and unit time as voltage is increased, due to the higher number of particles reaching energy high enough to cause ionization. Comparison between maps at different pressure is harder, as simulation at lower pressure necessarily require higher applied voltages and the final wire voltage is the result of the regulation due to the virtual ballast, making it harder to control its value.
With the aim of determining what makes a discharge look as a star-mode operating fusor, the map of molecular hydrogen ions born per unit time and unit volume is presented in three different conditions in Fig.4.20. Once again, spikes are present in the case of lower pressure, but this could be linked also to the higher voltage. For p=1.5Pa the birth position of ions is strongly localized in the centre.

The presence of atomic hydrogen in the background changes essentially only the neutral-impact ionization pattern, which shows a more *starry* behaviour.

Summary of the subsection Both ions and electrons are created preferentially in the central area.
Decrease of pressure and increase of applied voltage cause the ionization regions to resemble the one expected for microchannels. Previous simulation carried out by Osawa et al. [35] show electron-impact ionization to be relevant in the centre only above $1.5Pa$; this could be due to the fact that the cathode grid used to simulate the discharge in that case had smaller openings. Nevertheless, the presence of spikes is reproduced.
Increase in applied voltage increases the number of ions created in unit time, unit volume.
The fact that there is no preferential ion birth radius outside the cathode grid means that also energies of ions reaching the centre are distributed over a wide interval, as will be shown later.

4.3.3 Particle density and energy

As initial condition, the space inside the simulated vessel is filled with electron-ion pairs, so the first instants of the discharge result in the almost complete loss of electrons towards the outer wall. In the next time-steps, density of H_2^+ increases in the centre; electron density soon follows, but initially exhibits a more localized birth-region,probably due to the fact that electrons tend to escape the central region faster than ions (because of lower inertia) and are then accelerated outwards. Fig.4.3.3 shows the evolution of particle density showing the radial density profile at different time steps; clearly there is an initial accumulation of H, which results from charge exchange reactions of initial H^+ ions; the central region is soon depleted of neutrals, which cannot

be confined by the potential and both H_2^+ ions and electrons start growing in density more or less at the same rate, because of ionization of background gas. Also fast H_2 density grows inside the cathode grid as a result of growing H_2^+ and therefore increase in charge exchange with the background gas.
What is also interesting to notice is that density of neutral particles appears as a lorentzian shape, in contrast with charged particle density; this difference is due to the shape of the potential, which influences charged particles' density by confining them, but cannot affect neutrals density.

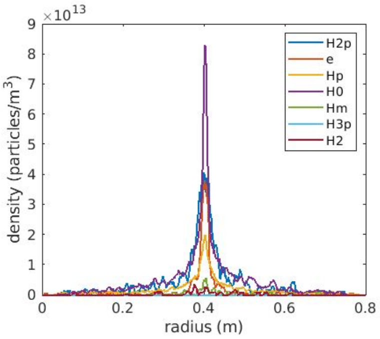

Figure 4.22: Density at $0.01 \mu s$

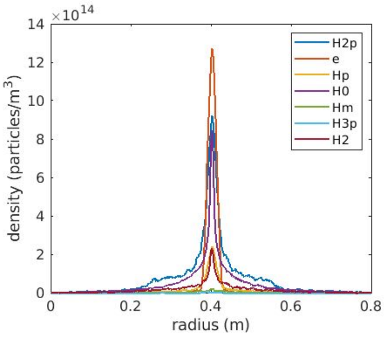

Figure 4.23: Density at $0.1 \mu s$

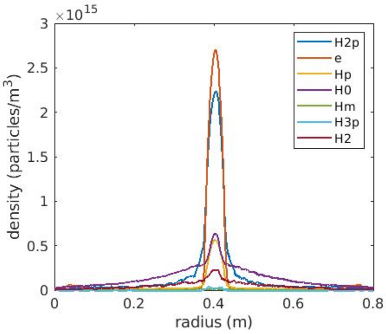

Figure 4.24: Density at $1 \mu s$

The most abundant species in the central region are the aforementioned electrons and H_2^+, followed by neutral atomic hydrogen and H_3^+.
Particle density inside the cathode grid is expected to increase with increasing applied voltage and pressure, because of the higher probability of both ionization and charge exchange reactions. This is shown in Fig. 4.28.
Now, density outside the central region both inside and outside the microchannels should depend on applied voltage as well. Regardless of where ions and neutrals accumulate, it is also relevant to know their energy. In particular, Fig.4.25,4.26 and 4.27 show the density of electrons H_2^+ and H^+ ions according to the energy interval they belong to. As it can be easily be seen, the central region of the cathode is occupied by both low-energy and high-energy ions.
Another interesting feature is represented by high energy electrons in the inner-cathode region: since the potential is flat in such region, electrons are expected to be formed at energy $< 20eV$, diffuse towards the aperture of the grid and be thrusted outwards towards the wall. The presence of high energy electrons is due to secondary emission from cathode wires and to electron detachment reactions; this can also be seen at $E_k > 10keV$: in the centre strangely-shaped density formation show up, which can be explained by considering them formed by electrons emitted from the wires.
Moreover, high energy ions and electrons seem to be present on well defined spikes converging towards the centre.

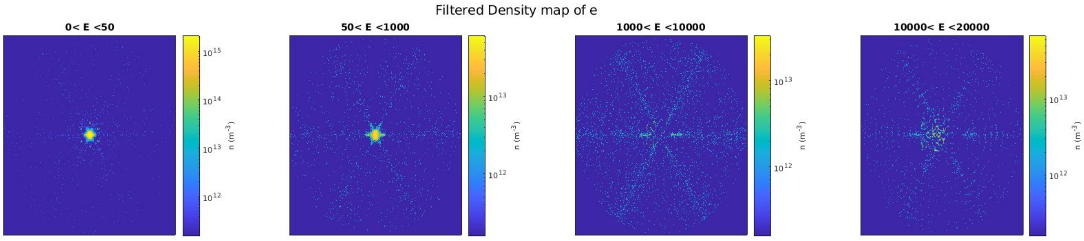

Figure 4.25: Density of electrons filtered according to energy interval (in eV).

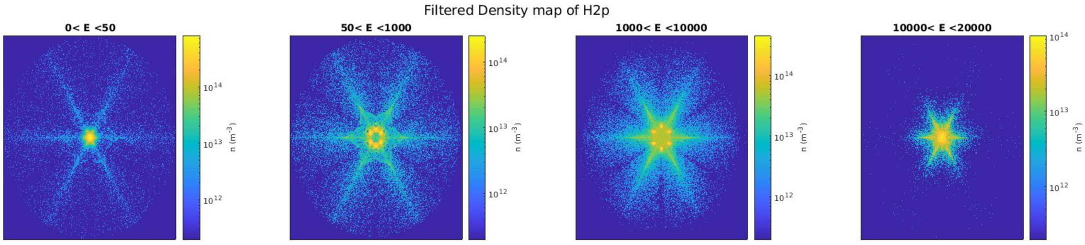

Figure 4.26: Density of H_2^+ ions filtered according to energy interval (in eV).

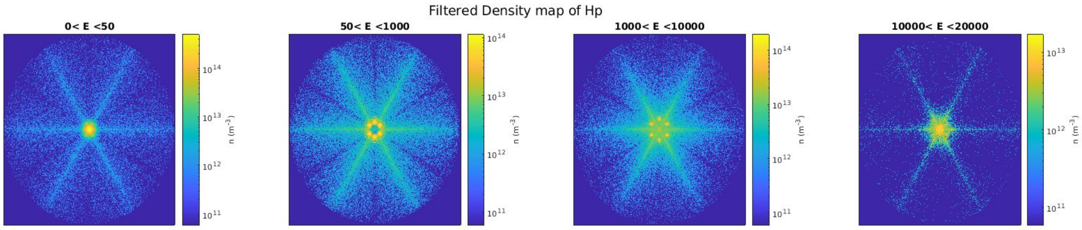

Figure 4.27: Density of H^+ ions filtered according to energy interval (in eV).

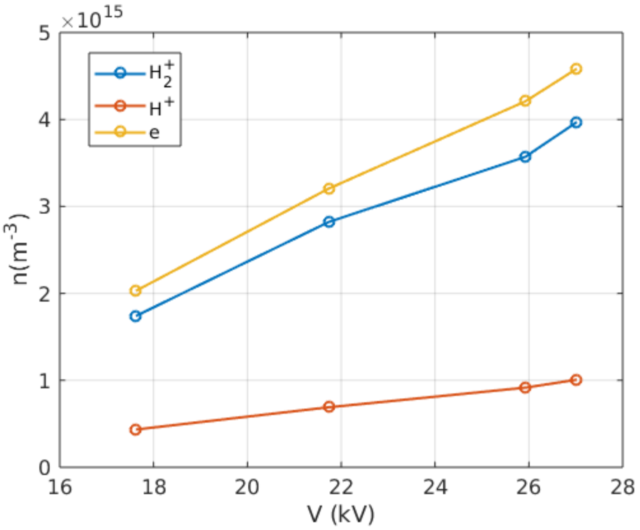

Figure 4.28: Density at the center for each particle species as a function of applied voltage.

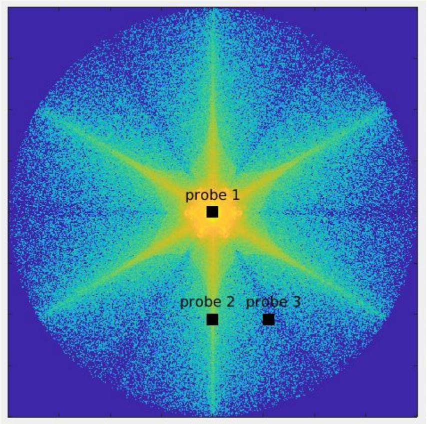

Figure 4.29: Probe position referring to density measurements in Fig.4.30.

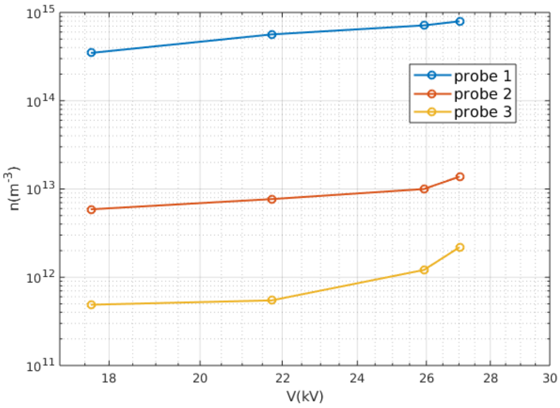

Figure 4.30: Density of H_2^+ at different voltages, from the three probes in Fig.4.29.

The filtered energy plots, as indicated before, show the presence of two ion populations in the centre. The energy distribution function of such species in the centre was calculated (Fig.4.31 and 4.32); as expected, ions exhibit a non-Maxwellian distribution, showing also particles with energies up to 80% of the applied cathode voltage. On the other hand, electrons exhibit energies mostly below $100eV$, except for a small contribution at higher energies. Due to the charge exchange reactions of H with H_2^+ hydrogen anions with the same velocity as the parent neutral are created. Since charge exchange cross section increases with increasing impact energy, high energy anions are expected. High energy electrons, on the other hand, are the product of electron detachment from such anions, which is the dominant process for H^-.
Despite the clear presence of fast ions in the central region, it is clear that the majority of particles accumulated in the centre has energy below $100eV$; this could be inferred by the previous section regarding particle creation, which highlighted that most ions are created in the centre by charge exchange and ionization.

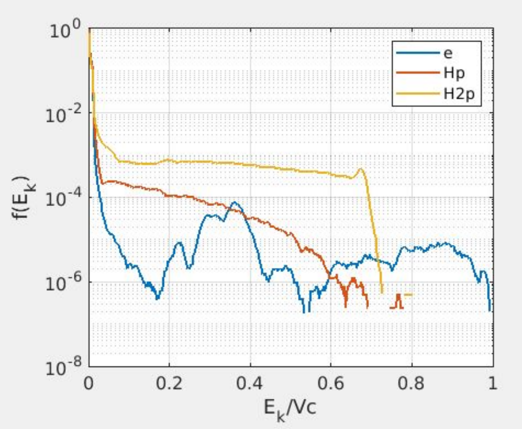

Figure 4.31: Energy distribution function at p=1Pa.

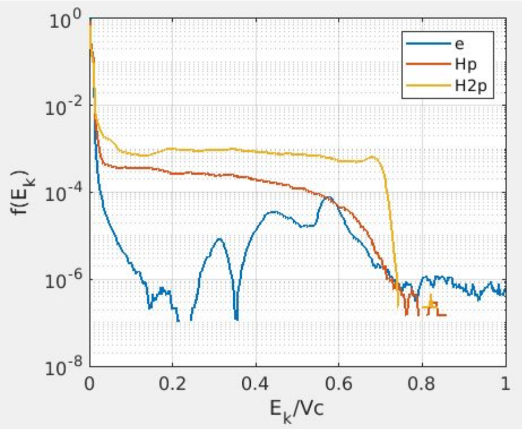

Figure 4.32: Energy distribution function at p=0.5Pa.

It was argued by previous studies, that microchannels are characterized by an enhanced fast ion population. In order to confirm such statement, a portion of a microchannel was considered and the corresponding histogram of kinetic energy was obtained.

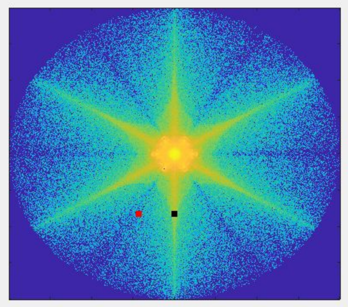

Figure 4.33: Density of H_2^+ at p=0.5Pa, with marked the two spots used to determine energy histogram.

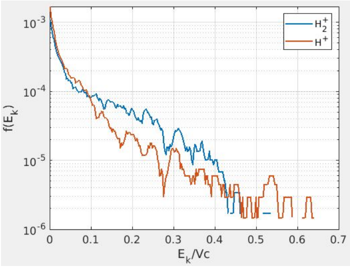

Figure 4.34: Energy histogram (normalized) corresponding to the black spot.

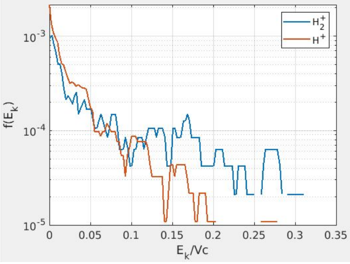

Figure 4.35: Energy histogram (normalized) corresponding to the red spot.

Ion population along a microchannel is composed $\sim 75\%$ of H_2^+ and H_3^+, and $\sim 25\%$ of H^+, which is different from the estimated density using experimental results; however, it must be

considered that such estimation referred to fast ions.
It was argued before that the ion population in a microchannel is composed for the most part of fast energetic particles. Fig.4.34 shows the energy distribution for particles belonging to a region within a microchannel, while Fig.4.35 shows the energy distribution of ions outside a microchannel. Both quantity are normalized to the total area. The histogram representing particles belonging to a microchannel clearly shows more statistics (less noisy) and a more significant population of H_2^+ and H^+ at higher energy.
The presence of a microchannel is also highlighted by the particular shape of ion density.

Summary of the subsection Energy distribution function of ions in the centre was determined and the dominance of slow ions was established. This was also visible in the maps of ion density filtered according to energy, where fast ion density is clearly one order of magnitude lower than slow ion energy.
The presence of microchannels is clearly detected at low pressure ($p < 1Pa$) both by considerations on density of charged particles and energy distribution function calculated inside and outside a microchannel.
Moreover, evolution of density in the centre and in the microchannel with respect to applied voltage was determined.

4.3.4 Secondary emission

The abnormal hollow cathode model proposed in [24] in order to explain the observed spectra, assumes that most ions and electrons are created in the centre (which is also observed by the present work) and that electron-impact ionization in the centre is due to the presence of secondary electrons emitted inwards from the cathode grid wires.
Secondary emission from cathode grid depends on the amount of ions hitting the cathode grid and their energy, so that an increase in secondary electrons emitted from grid is due to both an increase in the number of ions and an increase in their energy (or better, velocity, as described before).
Fig.4.36 shows how the average secondary electron yield (γ) evolves as a function of applied voltage and pressure.

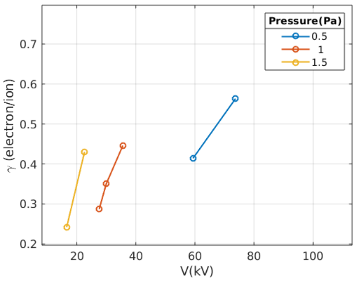

Figure 4.36: Secondary electrons emitted per unit time per hitting ion.

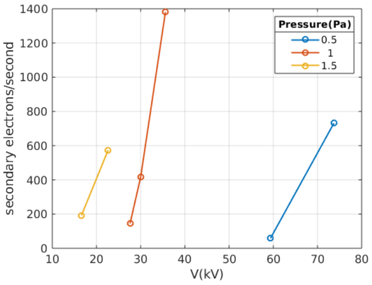

Figure 4.37: Absolute number of secondary electrons as pressure and voltage are changed.

The plot shows that in order to obtain the same secondary electron yield, it is necessary to apply a higher grid potential at lower pressure (this can be seen by comparing the $\gamma \sim 0.42$ points). In the following a possible explanation for such behaviour is given.
Most ions that hit the grid are expected to be generated quite close to it in the first place; ions that are born due to ionization far away from the central region are created preferentially along

the channels that cross the grid apertures, so their trajectories are guided inside the grid and are just slightly deflected by the grid potential, thus they are very unlikely to hit the cathode grid; an example of what ion trajectories look like near the cathode grid is shown in Fig.4.45a, 4.45b, 4.45c.Consequently it is a very unlikely event for a fast ion to hit the grid.

This leads to the fact that the ion kinetic energy when it hits the cathode grid is more ore less the one associated with the potential difference between the central region and the grid wires, which depends on the applied voltage and on pressure. Dependence of such well depth can be found in Sec.4.3.5 and clearly shows an increase of the difference as current or pressure are increased; dependence on pressure is almost linear. Another contributing factor to the relevant secondary electron number is given by the ion density in the vessel.

If the absolute amount of secondary electrons emitted is considered, an even steeper increase with applied voltage is expected. Since most ions that hit cathode grid are generate in the centre, as stated before, we expect that a denser inner cathode region could cause higher number of ions hitting the cathode (higher loss rate) and therefore higher number of secondary electrons emitted. The behaviour of the absolute number of secondary electrons shown in 4.37; increase due to increase of the applied voltage is particularly evident for the data at 1Pa. In the next section, the effect of applied voltage on the density of the central core will be assessed and it will be clear that at higher voltage the inner cathode density increases, justifying the explanation given above.

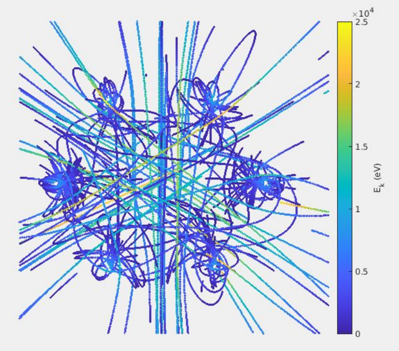

Figure 4.38: Trajectories of H_2^+.

Figure 4.39: Trajectories of H^+.

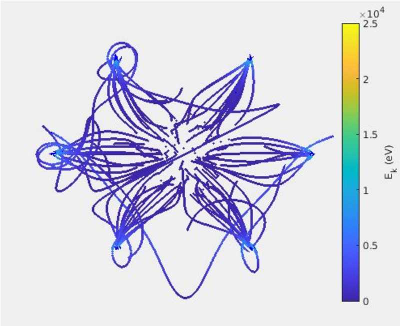

Figure 4.40: Trajectories of H_3^+.

Summary of the subsection The process of secondary emission was investigated in this section. Dependence on applied voltage is as expected. In particular, secondary emission increases with increasing voltage; at the same voltage, lower pressure entails lower secondary electrons emitted from the cathode grid.

It was however shown before that secondary emission is not as relevant as the correct modelling of the background in terms of discharge ignition and stabilization.

4.3.5 Potential

The presence of a growing charged particle density in the central region, and the build-up of a plasma, causes a relevant change in potential value in the same region. Fig.4.41 shows the difference between the potential predicted in vacuum for the given configuration and the potential in presence of the discharge. What can be noticed is an increase in voltage at the centre. In order to compare values of central voltage resulting from different applied cathode voltage, the ratio of the two is calculated.

What is expected is that the denser the centre plasma, the higher the difference with respect to vacuum condition. This means that higher pressure and higher applied cathode voltage will entail an increase in plasma potential and therefore an increase in the previously discussed ra-

tio. Fig.4.43 shows such value as a function of applied voltage at different pressures. Since the ratio between the central potential value and the applied cathode voltage at the grid wires i a constant value in vacuum, depending only on grid geometry (in our case ∼ 0.87), such ratio in the presence of plasma has the same behaviour as the one shown in Fig.4.43. Moreover, details about the central potential structure can be obtained by zooming in such region. What is seen is the formation of a small bump, of the order of some volts. The potential profile at different moments in time is shown in Fig.4.42.
Evolution of such bump as a function of applied voltage is almost negligible considering the estimate error. Moreover, even if it could be considered a virtual anode, its value is too small to produce any visible effects on fast particle motion.
On the other hand, its presence certainly affects trapping of slow room-temperature ions, such as H_3^+, which are attracted inside the two small wells.

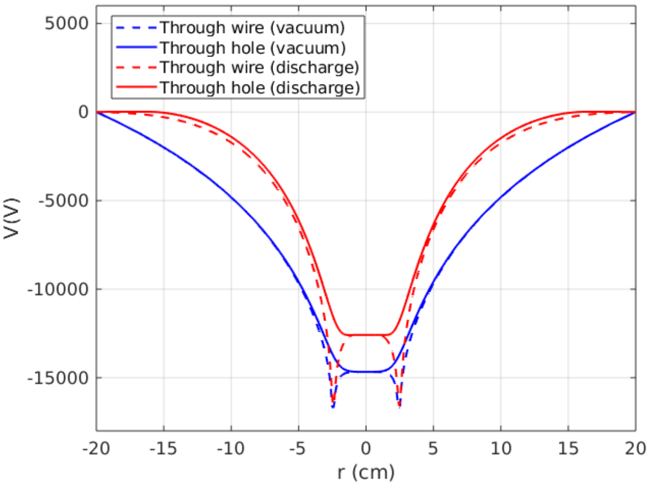

Figure 4.41: Full potential shape across the aperture (full) and crossing a wire (dashed), at p=0.5Pa,V=16kV, in vacuum and in the presence of plasma.

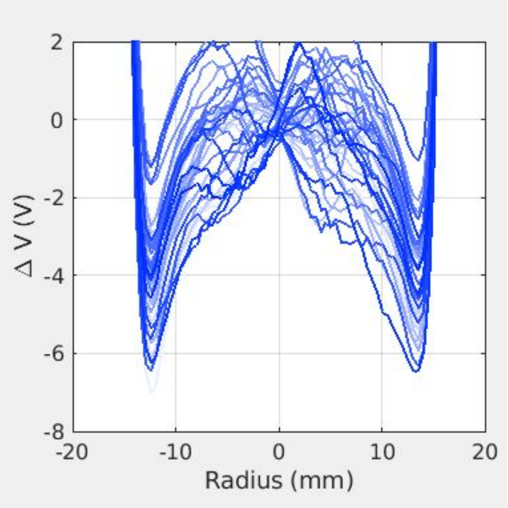

Figure 4.42: Detail of the potential profile through the grid opening inside the cathode grid (r=25mm), at p=0.5Pa,V=16kV

Despite not showing the expected behaviour, the inner structure can provide useful information

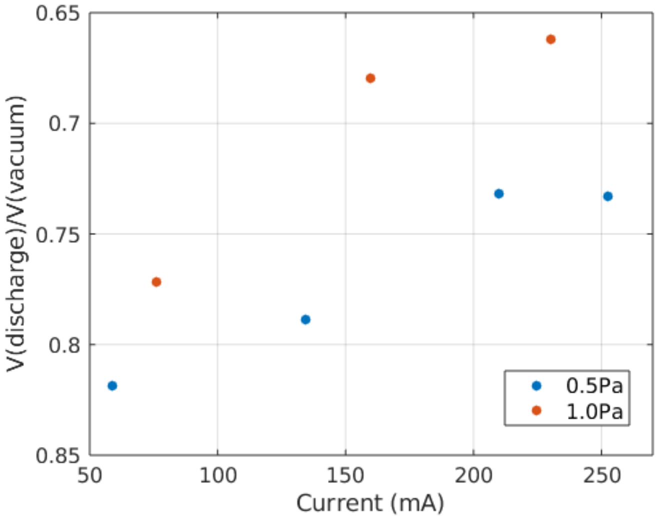

Figure 4.43: Ratio between the expected vacuum potential and potential perturbed due to the presence of plasma.

about the core radius. In particular, for the inner cathode grid modelled with 6 wires, the inner core radius is $\sim 22mm$ and its variation is not significant for change in density or applied voltage.

In order to force virtual anode formation, several attempts have been made.

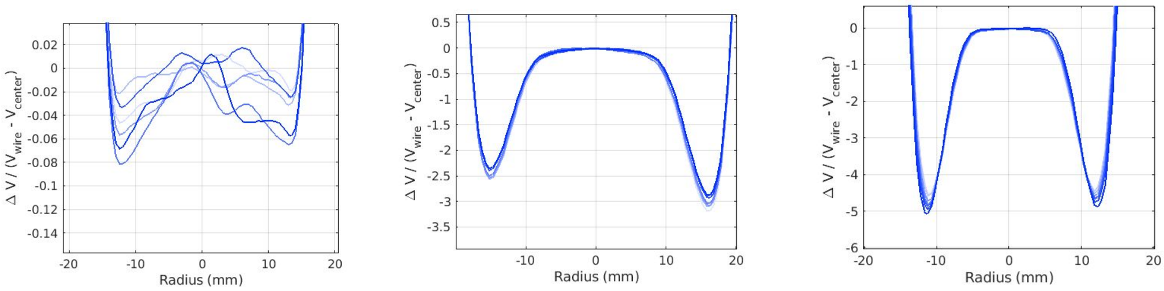

(a) d=2.5cm.

(b) d=2cm.

(c) d=1.4cm.

Figure 4.44: Potential hill in the centre created by ions for different geometries of the cathode grid, with different distance between grid wires. The quantity on the abscissa is the ratio between the height of the hill (ΔV) and the difference between grid potential and potential in the centre.

Firstly ion beams were pointed at the central region, in an attempt to reproduce Hirsch's work, but did not result in a relevant growth of an potential hill in the centre.

Secondly, the geometry was slightly changed, adding up to 8 wires to the central grid and also narrowing the distance between them (reducing the space between the single wires).

This attempt resulted in the formation of a potential hill up to 6% of the difference between the wire potential and the central potential, that is $\sim 200eV$. This evolution is shown in Fig.4.44.

The change in geometry, however, reduces the quantity represented in Fig.4.43. Moreover, focusing and energy distribution of ions inside the grid is not relevantly changed.

Summary of the subsection The effect on the potential of the presence of the discharge in the vessel was described in this subsection. The modification is in line with what was previously measured.

Moreover, a small potential formation was detected in the centre; radius and hill height is directly dependent of applied voltage, while dependence on pressure is not as clear.

Forcing virtual anode formation by injecting fast ions focused towards the centre does not result in the formation of a virtual anode.

Changes of the geometry provides promising results, as decrease of the spacing between grid wires causes increase in the virtual anode height, due to the fact that the wires maintain the low potential in the space in-between them more efficiently.

4.3.6 Trajectories and focusing

Ion trajectories in the vessel are a relevant feature to observe due to the importance of ion recirculation. They are represented in Fig.4.45 and 4.46; the former shows the difference in the behaviour of different species, whiel the latter depicts the recirculating trajectories of H_2^+ ions at two different values of pressure.

Firstly, it must be noticed that H_3^+ ions appear almost exclusively in the central area, due to the cross section for heavy particle exchange reaction being higher at lower energies. Secondly, they are soon drawn towards the cathode grid wires both due to the small well produced by the virtual anode and then by the more relevant well produced by the grid itself.

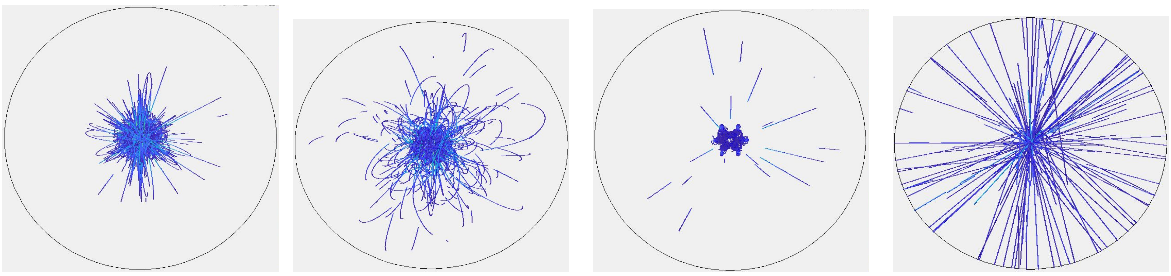

(a) H_2^+. (b) H^+. (c) H_3^+. (d) H_2.

Figure 4.45: Trajectories at 1Pa.

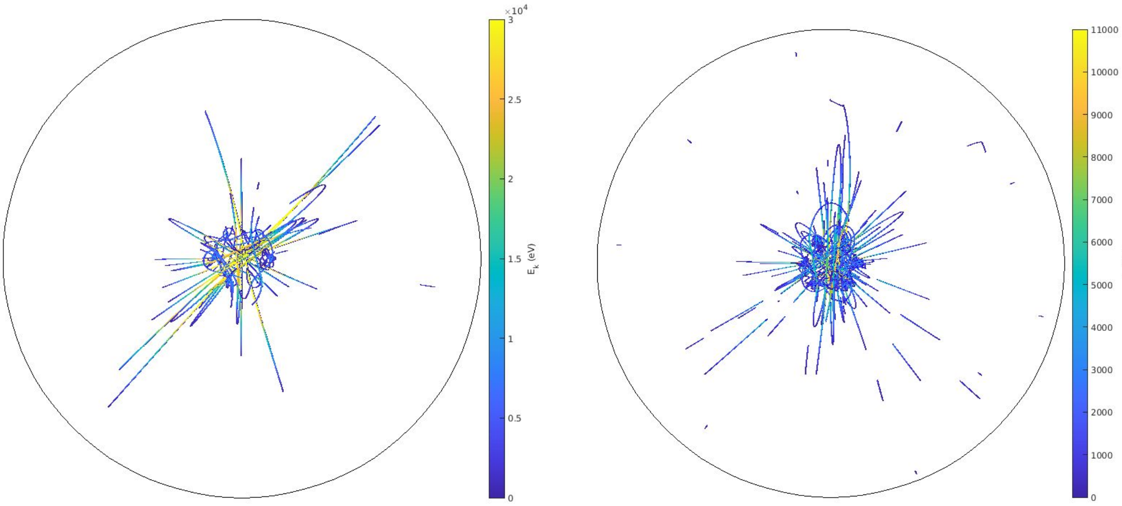

(a) 0.5Pa. (b) 1Pa.

Figure 4.46: Trajectories of H_2^+ at two different values of pressure.

H_2^+ and H^+ both exist also outside the cathode grid, but exhibit different behaviour. The former appears to oscillate back and forth, while maintaining a good focusing, that is a low tangential component of velocity. Such trajectories resemble straight lines; they are almost not present in the case of H^+. To understand the reasons of this difference, consider that straight trajectories are naturally drawn by ions being born at large radii and then accelerated by the central potential; ions being born close to the grid will be affected by the large non-spherical shape of the grid. Moreover, H^+ are lighter than H_2^+, which means that, even if they are born with the same initial energy, their velocity is twice the one of H_2^+, thus it is probable that the tangential component of velocity is already higher from the beginning.

The first observation leads us to look into the processes that generate the two species of ions. In the case of H_2^+, they are born mostly from background ionization, which might occur at grater radii due to electron impact or neutral impact. H^+ are born from dissociative ionization of the background gas due to impact of electrons,ions or neutrals. Ionization produces ions almost still, so it is not what makes tangential component of velocity higher.

On the other hand electron detachment from fast neutrals might be the cause of such behaviour, as neutrals are definitely not focused. Electron detachment is a process that produces both H_2^+ from fast H_2 and H^+ from fast H; however, electron detachment is more relevant in the formation of H^+ than it is for H_2^+.

In order to quantitatively analyze focusing, the angular momentum just outside the central region is evaluated. However, the angular momentum mixes information about particle velocity and direction; in order to evaluate the two aspects separately, two different quantities will be plotted: kinetic energy associated to motion in the tangential direction and angle between the ion direction and the radial direction.

Fig.4.47 show the evolution of the perpendicular kinetic energy distribution of H_2^+ outside the grid as the voltage is varied; Fig.4.48 shows the same but at different pressure. As expected, perpendicular kinetic energy is reduced as voltage is decreased. A visible peak around 0 is present, indicating that the perpendicular component of kinetic energy is preferentially low. Moreover, increasing the pressure value, increases the spread of the kinetic energy (this can be seen comparing the curves at $16kV$). This is due to the more frequent elastic collisions causing ions to change abruptly their direction of motion. The effect of pressure is however not enough to cause a relevant change in the size of the inner plasma core, as will be investigated in the next section.

The same effect is shown in Fig.4.49 and 4.50 for angular momentum of H^+. The broadening of the tails is different in the case of H^+, although the dependence on pressure and applied voltage are reproduced. It must be noted that having half the mass of H_2^+, H^+ ions should show a halved angular momentum, while in our case it stays comparable to H_2^+ results. This means that H^+ are definitely less focused than their molecular counterpart, as it was already evident in Fig.4.45.

Fig.4.54 and 4.53 show the histogram of the angle formed by the direction of motion and the radial direction. It is clear that the behaviour shown by the angular momentum is matched by the direction of motion, showing better focused H_2^+ at lower applied voltages and poorly focused H^+ ions.

The fact that change in pressure does not cause and evident change in angular distribution of H_2^+ ions confirms the assumption that the narrowing of the tails is actually due to the lower velocity rather than the better focusing.

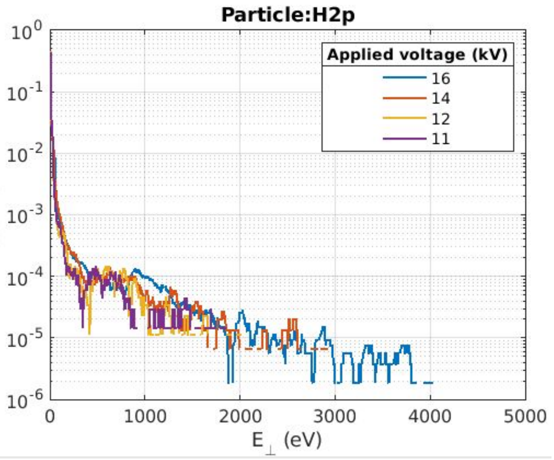

Figure 4.47: Perpendicular kinetic energy distribution of H_2^+ inside the cathode grid, at different applied voltage, at 1Pa.

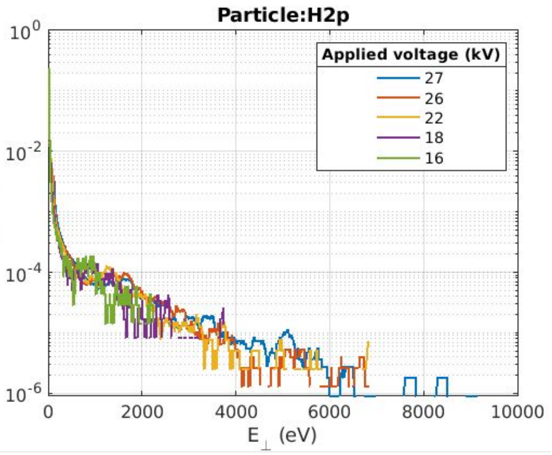

Figure 4.48: Perpendicular kinetic energy of H_2^+ inside the cathode grid, at different applied voltage, at 0.5Pa.

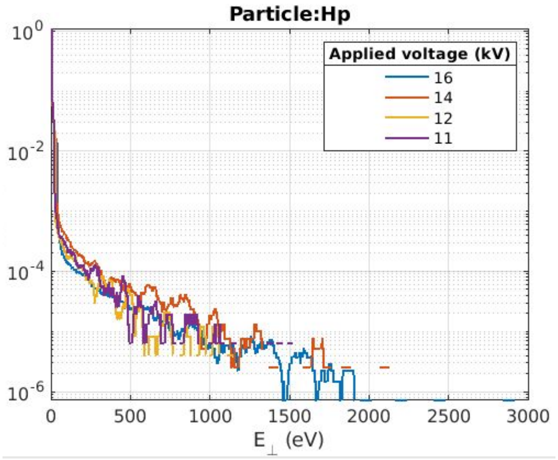

Figure 4.49: Perpendicular kinetic energy distribution of H^+ inside the cathode grid, at different applied voltage, at 1Pa.

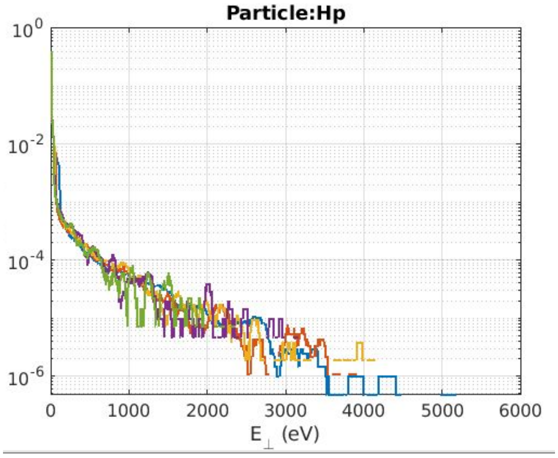

Figure 4.50: Perpendicular kinetic energy distribution of H^+ inside the cathode grid, at different applied voltage, at 0.5Pa.

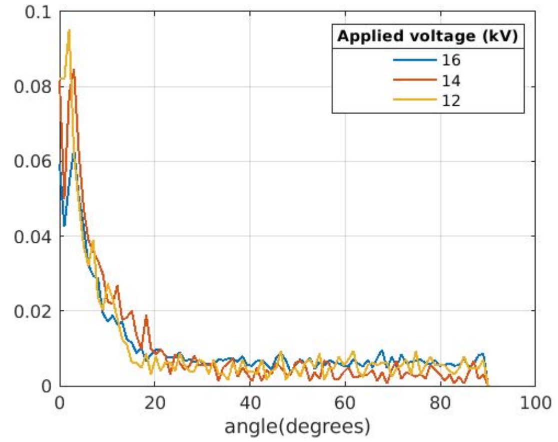

Figure 4.51: Distribution of the angle formed by H_2^+ velocity vector with the radial direction, at 1Pa.

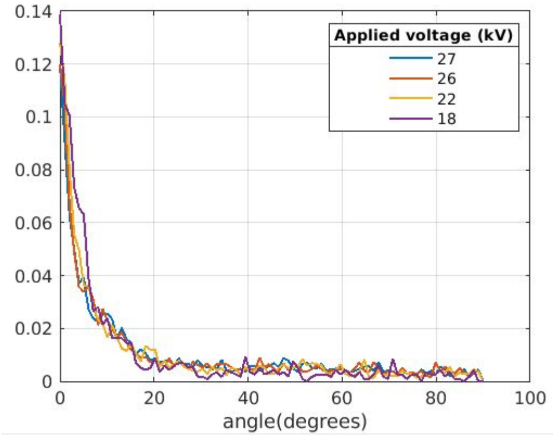

Figure 4.52: Distribution of the angle formed by H_2^+ velocity vector with the radial direction, at 0.5Pa.

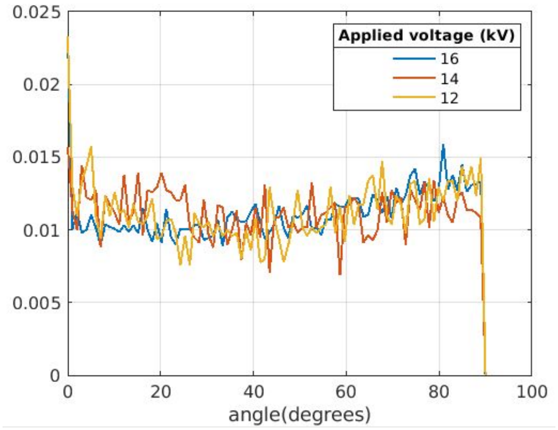

Figure 4.53: Distribution of the angle formed by H^+ velocity vector with the radial direction at 1Pa.

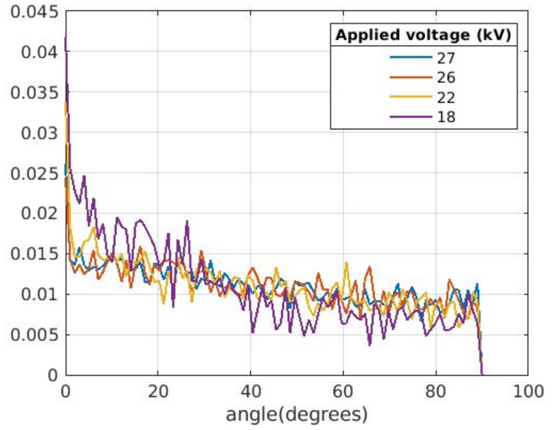

Figure 4.54: Distribution of the angle formed by H^+ velocity vector with the radial direction at 0.5Pa.

4.3.7 Spectra

Finally, the reactions listed above, in Sec.2, are used to produce excited H atoms emitting a Balmer-α photon, which can be recorded and counted as contribution of H_α radiation coming from the fusor.

Selecting only the radiation coming from a desired area and taking into account the angle between the motion of the selected neutral and the line of sight, it is possible to build a synthetic spectral line.

The 2D geometry used for the model from extracting exactly the experimentally recorded spectrum, which is built from a contribution of many different microchannels. What I think is more useful in terms of comprehension is selecting a limited segment of a microchannel and plotting the expected spectral line, using different inclinations of the line of sight with respect to the channel.

What is interesting to know, in particular, is the evolution of the detected peaks with distance from the centre and correlate it to the potential shape.

Fig.4.58 shows an example of selected lines of sight.

We already have discussed the absence of a virtual anode in our simulation, if we exclude the tiny bump forming inside the grid; based on the interpretation given for experimental spectra, which is based on the presence of a virtual anode, the presented spectra are not expected to show the same behaviour.

First off, a limitation on spectra simulation is given by the interruption of the cross section forming excited neutrals, shown in Fig.2.2 and Fig.2.1. Fig.4.55 shows the effect of such limitation. In particular, the clear peak present on the blue-shifted side of the spectrum is in reality due to the limited cross section fro the formation of fast neutrals. Fig.4.55 shows the phase space of the excited neutrals born in the time steps considered to build the spectrum. Each pixel contains the number of neutrals having the given velocity and position within a 200eV and 1mm interval, respectively; the left plot represents the kinetic energy associated with the y component of velocity, while the right plot represents the x component. The particles considered to build the plot are the ones contained in the channel taken into consideration. In order to calculate the doppler-shifted wavelength, the velocity vector of the excited neutral must be projected on the line of sight. The angle between the line of sight and the y-axis in the case of simulated spectra is $\sim 25°$, therefore the major contribution is given by the $y - component$ of velocity; in order to understand the spectral shape the plot on the left of Fig.4.55 will be used.

The phase space shows a clear concentration of neutrals at $E_{k,y} \sim 3keV$, which is the lower energy limit for the cross sections given by [46]. In order to overcome such effect, the experimental cross sections were extended using a linear interpolation between the lower energy value and the origin. Then effect is shown in Fig.4.56: the peaked energy is no longer present.

Fig.4.57 shows the comparison between the synthetic spectra acquired assuming original cross

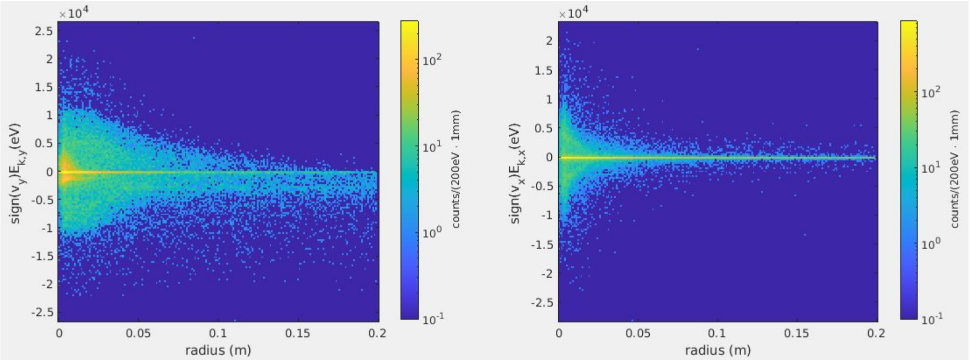

Figure 4.55: Phase space with cross section as given by [46]. y direction is along the channel, the negative sign represents ions moving out.

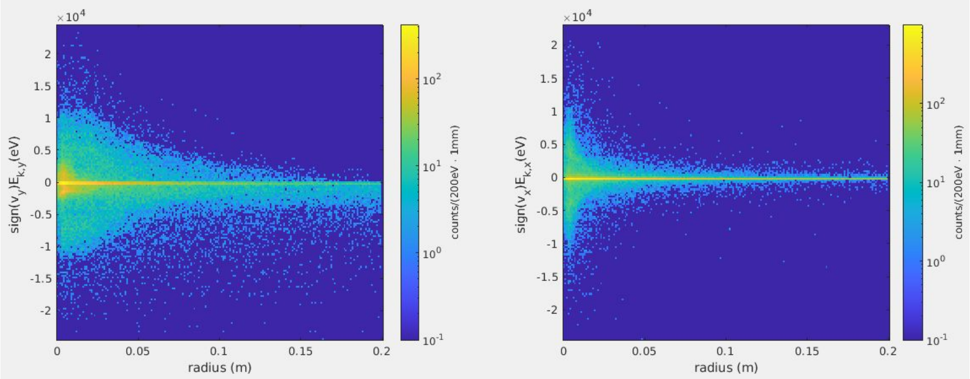

Figure 4.56: Phase space with extended cross sections. y direction is along the channel, the negative sign represents ions moving out.

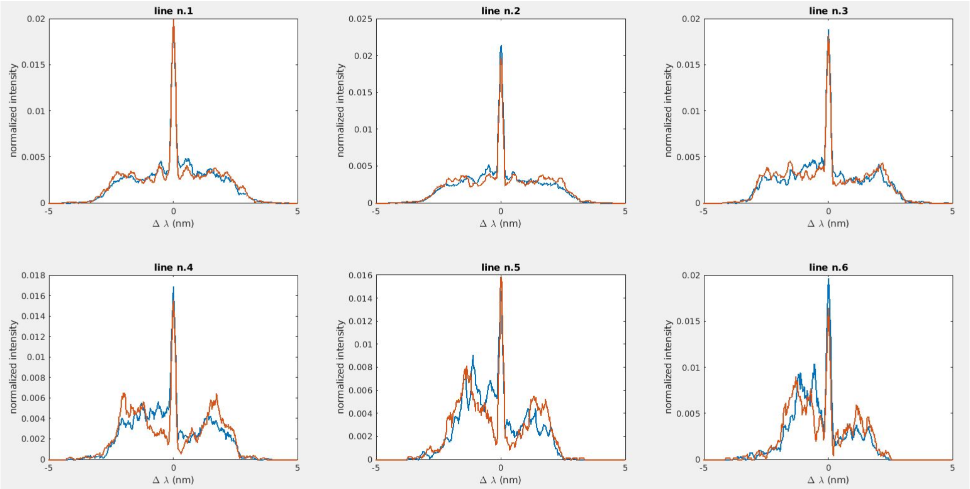

Figure 4.57: Comparison between the spectra recorded with extended cross sections (blue) and with original cross sections (orange).

sections or extended cross sections: the gap between the central peak and the shoulders is filled due to the extension of the reaction probability.

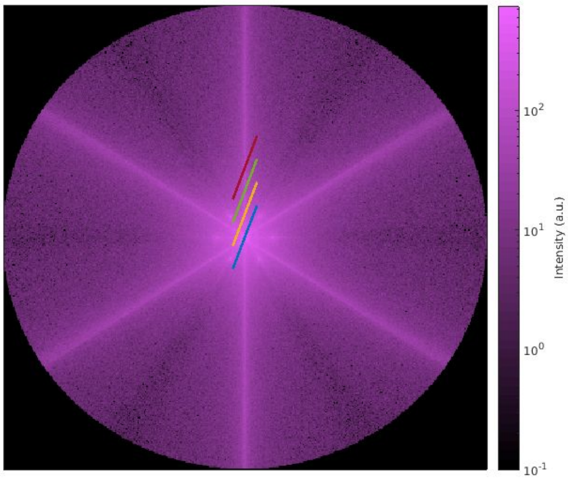

Figure 4.58: Line of sight used to extract the spectra. Only odd line of sight are depicted, in order to create a clearer picture.

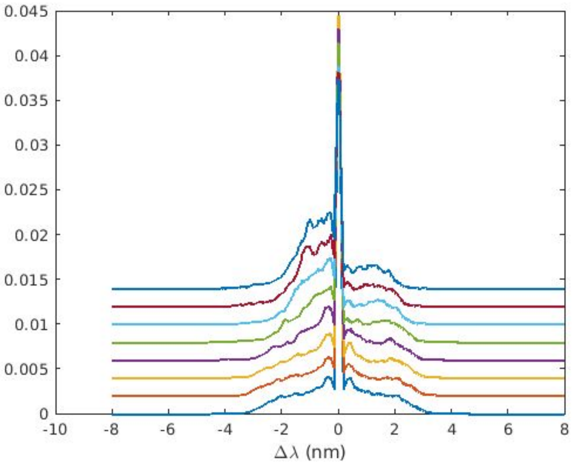

Figure 4.59: Shape of the spectra acquired at different positions along the channel in the presence of a virtual anode.

Fig.4.59 shows the spectra extracted from a 0.5Pa,25kV discharge, spectra must be read from

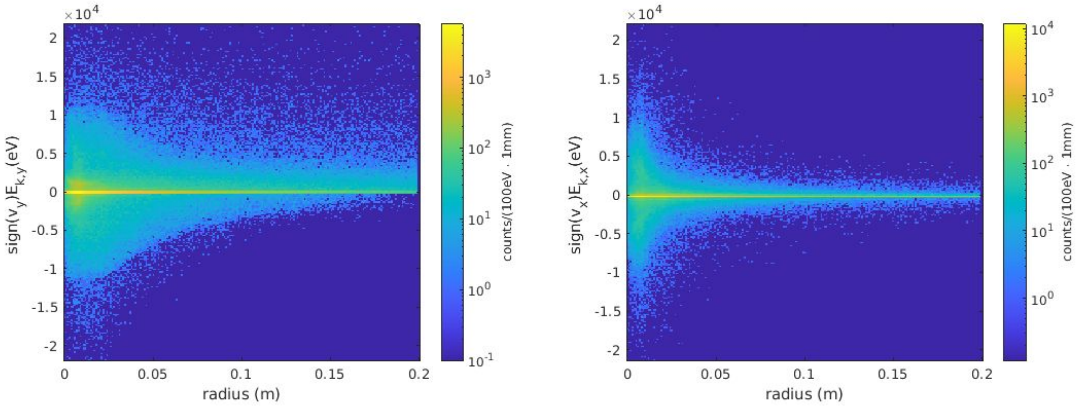

Figure 4.60: Phase space for a discharge at 0.5Pa and 25kV.

the bottom to the top, which corresponds to the increase of the distance of the line of sight with respect to the centre. It is clear that no peak is established at any position along the channel. Such feature could have been inferred from Fig.4.60; such plot also shows interesting features. The upper part (correspondent to inward moving particles), follows what is expected from the evolution of the potential, with higher energies possible in the centre rather than far out.
Towards the centre, a higher concentration of low energy particles is expected, due to the high concentration of both electrons and ions capable of forming excited hydrogen atoms. This effect is also shown by the plot.
Now take a given value of the radius (let us say 5cm); if one considers the corresponding section of the histogram, around $E_{k,y} \sim 0$ the histogram shows a peak, then a wing of intermediate energies shows up and lastly, an even less intense wing at higher energies is detected; this is expected due to the fact (explained in Chap.2) that fast H^* born from charge exchange reactions end up with the same velocity as the parent ion, meaning that ions with higher mass create hydrogen atoms with lower velocity (at the same value of original kinetic energy).
Lastly, the outwards moving component of the phase space shows a different shape: this is due to fast neutrals being excited; such neutrals have a kinetic energy which is not constrained by the potential value and therefore H^* moving out may be born at energies higher than the ones reached by H^* moving in.
Judging from the depicted phase space, the presence of a clearly positioned peak is not explained. The potential shape influences the phase space in terms of limiting the maximum reachable kinetic energy at a given position. Such limit corresponds to the value of the applied potential at such position.
The spectra obtained at 4Pa (Fig.4.61) shows symmetric peaks, both in intensity and in shift position, as measured experimentally, showing that higher pressure prevent channels from forming.

In order to obtain the effect of a modified potential on the acquired spectra an artificial potential shape was inserted in the model, imposing a virtual anode in the centre as depicted in Fig.4.62. The phase space resulting from such potential structure along the opening of the grid is shown in Fig.4.64: the potential structure is matched even in this case by the shape of the phase space. Moreover, an evident highlighted formation shows up, which looks like the shape of the virtual anode. Those are ions coming from the central core and heading outside.
According to the extracted spectra, the position of the peak, which is now, as predicted, quite defined, draws the potential shape. Such behaviour is the one that was speculated in Sec.3.
Fig.4.65 shows the evolution of the spectra as a function of the height of the virtual anode. The Doppler shift returns in each case the value of the potential in such position, with the maximum shift corresponding to the virtual anode height. The width in the centre, on the other hand, depends on the derivative of the potential in the proximity of the virtual electrode, as the line

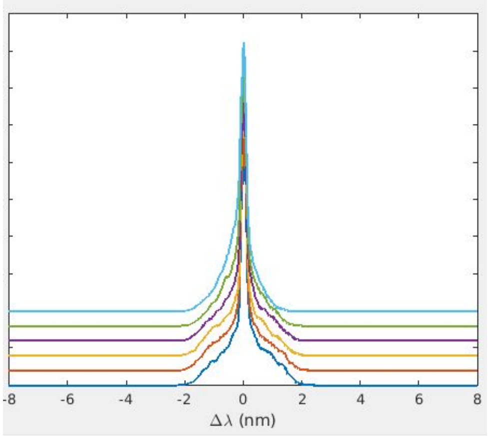

Figure 4.61: Spectra acquire for a 4Pa discharge.

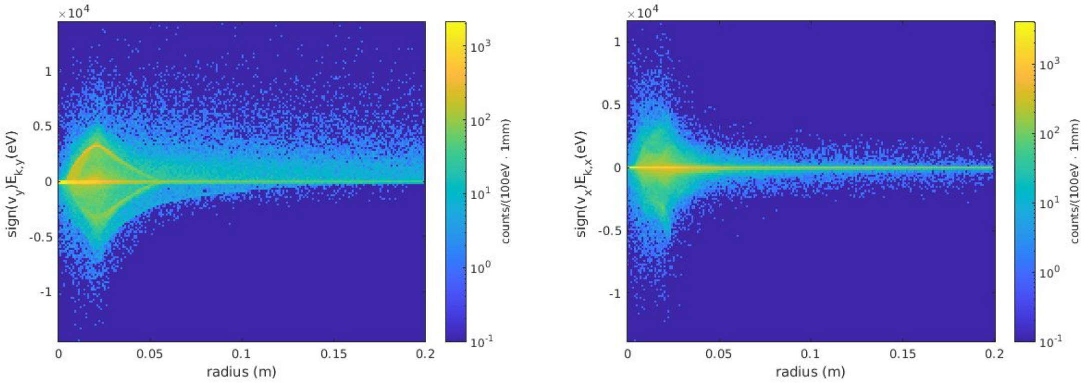

Figure 4.64: Phase space in the presence of a virtual anode.

of sight contains also information about positions near the selected one: the maximum shift is representative of the maximum recorded kinetic energy, which might belong to ions already falling down the hill.

Pressure does not change significantly the shape of the recorded lines, with the same virtual anode.

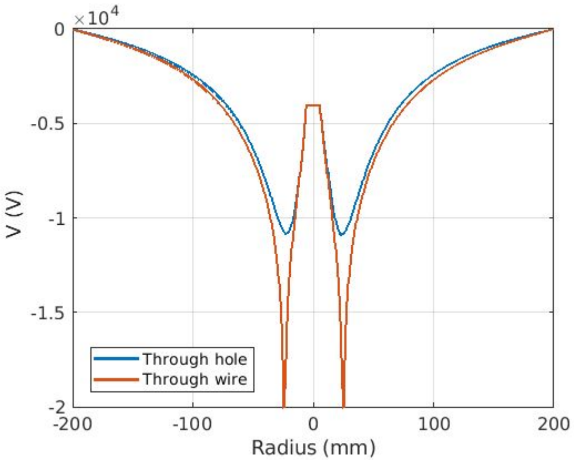

Figure 4.62: Shape of the potential with a virtual anode.

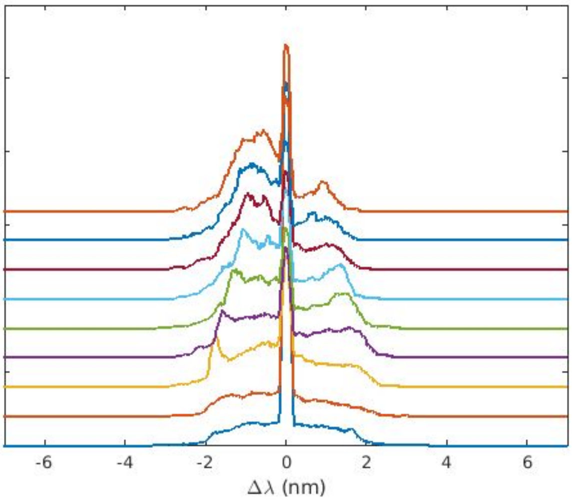

Figure 4.63: Shape of the spectra acquired at different positions along the channel in the presence of a virtual anode.

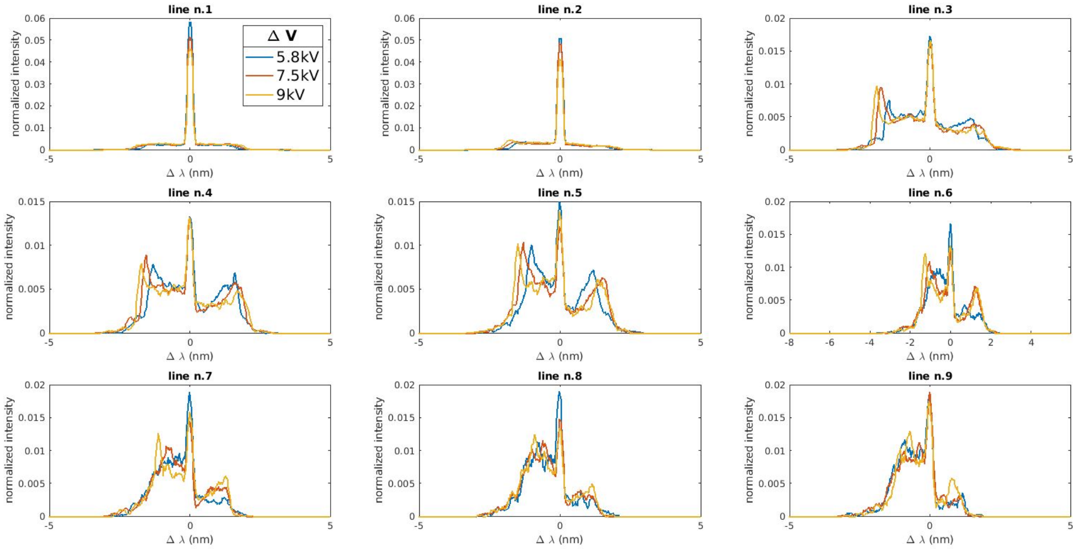

Figure 4.65: Evolution of the spectra with changing virtual anode height.

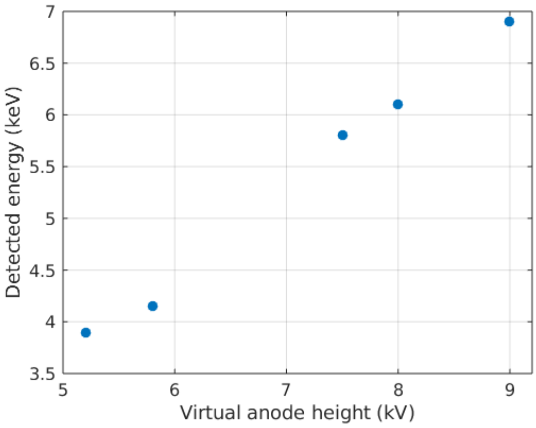

Figure 4.66: Evolution of the detected shift in the spectrum with respect to the virtual anode height.

4.4 Summary

The simulation work reproduced the expected behaviour of a fusor in terms of particle birth and their distribution in the space inside the vessel; the presence of microchannels was demonstrated at 0.5Pa by studying both ion density evolution inside and outside the supposed microchannel and the ion energy distribution along it.

The discharge current reproduces well the behaviour of the real discharge, even though the exact current and voltage values are different. On the other hand such different was expected, since even the change of the inner cathode in the same machine produced the discharge carachteristics shown by Messmer [29], which are $\sim 2kV$ shifted with respect to the ones measured in this wok with a different cathode grid. It is therefore natural to suppose that cylindrical geometry could provide a relevant change in the voltage necessary to provide the same current.

The presence of the dissociated background, with H atoms as well as H_2 molecules, allows to obtain discharges closer to the experimental ones, indicating the importance of such feature.

As expected, the central region is populated both by low-energy ions and high energy ions, being accelerated by the applied potential.

As showed by the source functions, the majority of ions is born in the inner cathode region due to ion or neutral-impact. Therefore, lower angular momentum of ions, which causes a better focusing,would cause ionization in a smaller area, resulting in faster accumulation of ions in a smaller region and therefore increase in virtual anode height.

The potential change due to the presence of plasma in the inner cathode grid region consists in an increase of the central potential with respect to the vacuum estimation.

Zoomin in the central region shows the growth of a small hill, within $5eV$, which is too low to produce any effect on the motion of fast ions. If the geometry of the central grid is changed, however, the hill grows up to $200eV$, indicating that geometry is a sensible parameters to be modified.

Overall, the spectra are not modified by such hill, and they still don't show any preferential velocity, as highlighted by experimental results. If, however, a virtual anode is imposed in the central region, spectral shapes show the growth of a peak on the blue- shifted side (that is ions diverging from the centre).

Although the presence of a peak is demonstrated, still the spectra show several differences with respect to the real ones acquired with the fusor. Firstly, the peak shows up also on the red-shifted side, as ions are bounced back. Secondly, the peak is present for a limited distance, which corresponds to the distance travelled by diverging ions before their motion is reversed due to the potential.

Experimental results show an increase in kinetic energy up to a certain position and a subsequent slow decrease as the position is moved outwards. The increase up to a maximum wavelength of the shift is seen for line 3 in Fig. 4.65; while the increase from the centre happens on a 3cm range, the decrease after reaching the maximum takes place on a longer distance.

Chapter 5

Conclusion

This thesis is devoted to the experimental and numerical characterization of an Inertial Electrostatic Confinement (IEC) device. In Chap.2 the theoretical background to the Doppler spectroscopy technique was provided, along with the discussion of previous experimental results and interpretations.

In Chap.3, the experimental activity was described.

The designed experimental apparatus provided 1° sensitivity in the horizontal movement (scanning the microchannel along its axis) and 0.3° along the vertical direction. A cathode grid with larger openings was designed in order to provide a clearer view of the microchannels.

Discharge characteristics were measured in order to find the parameter range in order to obtain a star-mode discharge; Star-mode was detected at $p<2$Pa.

By employing both moving gears to move the line of sight, spectroscopic measurements were collected in order to determine the presence of microchannel, as they were expected to provide the major component of the radiation coming out from the fusor.

Scan of the microchannels in the horizontal direction allowed to obtain the spatial profile of the kinetic energy of ions moving along the channel, upon distinguishing contribution coming from H^+ or H_2^+. Spectra showed clear peaks in the Doppler-shifted shoulders, which could be fit with gaussians. Widening of the peaks is due to different causes: notably the fact that not all neutrals de-excite at the same distance from the birth radius and the fact that the line of sight is not aligned with the channel, though the angle between the two is $< 30°$.

The estimated kinetic energy showed a decrease towards the centre and a progressive decrease as the line of sight was moved in the outer region. Moreover, dominance of the blue-shifted component was detected.

Higher pressure provide no evidence of the presence of relevant microchannels, therefore corroborating the hypothesis that the previous measurements were, in fact, detecting such formations.

With the aim of reproducing the measured behaviour, an effort to produce synthetic spectra was made. Chap.4 describes the PIC-based numerical simulation employed to reproduce the discharge in the fusor. Discharge characteristics such as current-voltage curves show agreement with experimental data in terms of behaviour, though the exact current-voltage values are reproduced within a factor ~ 2. Moreover, dissociate background is a necessary feature in the simulation in order to provide the ignition at lower applied voltage.

Star-mode operation was obtained and identified measuring ion energy and density along the channels; channels show in fact a consistent population of fast ions, strong directionality of such particles and a higher density. Moreover, most ionization reactions occur along such paths, as expected.

The spectra obtained form the simulation are different from the experimental findings in that

they do not exhibit any relevant peak in the blue-shifted side, though its dominance is reproduced as the line of sight is moved at outer positions. Moreover, the decrease in kinetic energy in the centre is not shown by the spectra produced in such conditions. Since discharge behaviour shows no relevant difference from what was measured before, and since the spectral shape is easily linked to the potential shape, it is reasonable to assume that the different spectra are obtained due to different potential shape.
A virtual anode was placed as an assumption in the central spot. Such change provided the defined peak that was observed experimentally; the shift reaches a maximum at the cathode grid radius and then decreases. The preferential velocity ceases to exist, as shown more clearly by Fig.4.64, after approximately 5cm from the centre. On the other hand, experimental results show an evident peak even at outer positions. It must be considered that in average the excited neutral lives as long as $2cm$ (or 10cm, if the electron is excited to a 3s state), as described in Sec.2, therefore information about its kinetic energy might be delayed.

Since the absence of a virtual anode results in a spectral behaviour different from the experimental one in terms of shoulder peak formation and shift evolution, the hypothesis of a potential hill being the cause of experimental results is taken into consideration. Moreover, even if the kinetic energy value is subject to many errors, the presence of a defined peak in the shoulder is undeniable and cannot be explained without assuming that such ions are actually coming from the same originating spot. There is no reason to assume that ions are born preferentially at a particular radius outside the central region; the fact that 1D simulation conducted by Messmer [29] using Emmert and Santarius [9] and the 2D Particle-in-Cell simulation done in this work show no localization of ion birth corroborate such assumption. In fact, most ions are actually born in the centre, so it is reasonable to assume that the presence of a virtual anode could cause the fall of such ions through a well defined potential hill, causing the detected peak in the spectrum. This was seen in the simulation.
Therefore, embracing the assumption of a virtual anode being the cause of the observed peak, an issue remains in interpreting the non-null kinetic energy showed in the centre. The kinetic energy in the centre is in fact related to the deceleration of ions coming from the other side, rather than ions exiting the centre, which should contribute to the central peak in such position. In fact, at such position no peak is present. As the line of sight is moved outwards, the dominating component is given by ions moving away from the centre. Contribution due to ions coming from the other side is reduced because of two reasons: firstly, the mean free path for charge exchange at 0.5Pa is $\approx 6cm$, which makes it progressively improbable for ions to survive for such a long distance, secondly ions capable of reaching a certain radius must be born at a radius greater or equal to it on the other side. As the line of sight is moved outwards, the interval of possible birth radii is reduced, therefore reducing the number of ions reaching such position. Simulated spectra without virtual anode show a sort of plateau rather than a peak: this is how the contribution from ions coming from the other side of the vessel should look like in the experimental spectrum.
Finally, also excitation due to H impact must be considered, as shown by Williams [46]: this leads to a contribution similar to the previous one, with the difference that it is not affected by the potential.
Summarizing two interesting contribution coming from ion populations are present in the blue-shifted shoulder of the spectra, assuming the goodness of the virtual anode hypothesis:

- Ions originating in the centre, creating a clear peak as they roll down the hill, particularly evident in the outer region;

- Ions coming from the other side of the vessel, forming plateau rather than a defined peak, it is dominant in the centre.

Therefore, the kinetic energy recorded in the centre should be associated to fast ions coming from the other side and being decelerated by the potential hill, therefore it is an indication of the potential value on top of the hill, while the maximum kinetic energy corresponds to the height of the potential well. Therefore, the sum of the two should be the potential at the bottom of the well. Consistently, the sum of the two is always $\sim 1.5keV$ lower than the actual applied voltage. On the other hand, the simulated spectra do not confirm such hypothesis, since also fast neutrals can travel past the centre and get excited on the other side, therefore enabling any possible value of kinetic energy to be detected.

A difficulty in interpreting experimental results is posed by the fact that pressure may play an important role in the value of kinetic energy of neutrals, as higher collisionality would allow neutrals to be accelerated by a smaller fraction of the potential hill. In particular, assuming that the derivative of the potential is the same in any situation, a doubling in pressure would cause a halving of the recorded ration between kinetic energy and potential (Tab.3.3). However, it is clear that such rule does not apply in the present case: on the contrary, if the value at 0.3Pa is taken as reference, all other ratios are higher than expected. This leads to believe that deconvolving information of pressure and applied voltage is a difficult task.

In any case, the evaluated height of the potential well, which according to Fig.3.19 ranges from 35% to 45%, agrees with estimates given by Gu and Miley [15], who argue that the virtual anode shows a depth $\sim$ 27% of the applied voltage (though they use $\sim 2Pa$ discharges), Kachan [22], which shows a fraction of $\sim$ 25% and lastly Hirsch, as presented by Miley and Murali [31], which measures a depth of $\sim$ 40%. As commented in Sec.3, discharges at 1Pa and 1.5Pa do not show a behaviour as clear as the results at lower pressure; in particular, no real maximum of kinetic energy is found.

Lastly, interpretation of the innermost peak is still missing. Simple geometrical explanation is not applicable to the case, as it would require an angle between the line of sight and the channel that is far greater than the one predicted with the geometrical reconstruction.

The hypothesis of it being the real product of the motion of fast ions along the microchannel has been considered, but its presence during high pressure discharges, in the absence of microchannels has led to believe that it could be related to some other feature; moreover, the composition of the microchannel in terms of H^+ and H_2^+ population is in accord with previous measurements, leading to believe even more than the outermost peaks have been rightly identified. Nevertheless, it could be true that the furthermost peaks are related to the ions passing closer to the cathode grid wires and becoming neutrals before hitting it, while the innermost peak could be due to ions rightly falling down the potential hill formed by the virtual anode; that would imply a kinetic energy associated with such peak of $\sim 300eV$, which is compatible with what was found by the simulated discharges; this hypothesis must be further investigated and could be ruled out by a simple clean-up of the vessel. This interpretation is however unlikely, as such neutrals would be directed along very different paths from the one of the microchannel. The same peak was found by previous studies, as shown in Chap.2 in Sidney, while recent articles done with the same machine, do not show such peak, indicating that rather than a physically relevant phenomenon it might be related to impurities.

5.1 Future work

Further improvement of the code is required in order to provide evidence of virtual anode formation. Since modelling of collisions has provided results in good agreement with experiments, the next step consists in improving geometry modelling, in particular employing 3D geometry instead of 2D.

Since the formation of a virtual anode relies on the two processes listed in Sec.1.1.1, it is instructive to think of possible ways in which spherical geometry might modify such processes. Firstly, focusing of ion trajectories might be affected by the fact that ion do not travel through two adjacent wires, but through a sector of a sphere, therefore having 3 confining boundaries rather than just two lateral ones; this would project all the ions at different z-positions in the present simulation, to a smaller portion, increasing their density and therefore also their density in the centre. Exit of electrons through the grid wires would be enhanced: in the present simulation, ions are not lost if they move in the z direction, while in spherical symmetry they would ,leaving a higher space charge behind.

In such a way, it would be possible to determine what effects cause virtual anode formation and the role of pressure in such process.

Moreover, Doppler-spectroscopy, though providing a relatively simple concept, is limited in spatial resolution. One way of providing a better spatial resolution would be building a rotating system capable of rotating exactly along mirror axis and a line of sight perfectly aligned with the center. This would provide an easier calibration (based only on geometry). Still, limitation is also related to the position of the optical apparatus and the difficulty in excluding contribution from other microchannels on a given spectra. The latter can be avoided by building a simpler grid, with only two parallel rings, so that just one channel would form; it is however not guaranteed that such geometry could provide a virtual anode; moreover, it would serve only as confirmation of the already obtained results.

Overall, though giving a clear indication of ion kinetic energy, Doppler spectroscopy is not enough to reconstruct exactly the potential profile with the resolution needed for the detection of potential formation inside the grid. Other techniques might be applied, such as LIF spectroscopy, which could provide a spatially-resolved measurement of fast ions.

Lastly,the spurious peak, which have been identified as related to impurities should be suppressed, hopefully by cleaning the vessel.

Appendix A

Cross sections

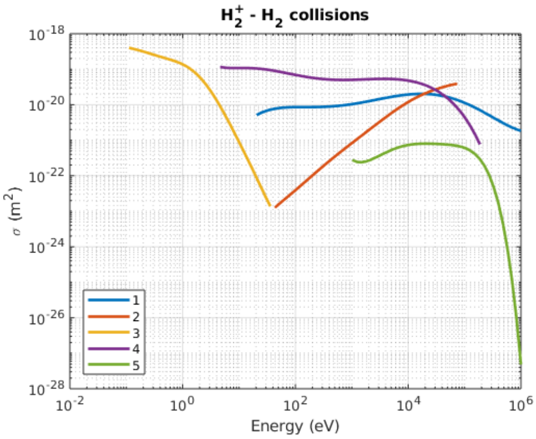

Figure A.1:
1. H_2^+, H_2 → H^+,H, H_2,e (dissociative ion.)
2. H_2^+, H_2 → H_2^+,H_2^+,e (ion.)
3. H_2^+, H_2 → H_3^+,H
4. H_2^+, H_2 → H_2,H_2^+
5. H_2^+,H_2 → H*(n=3)

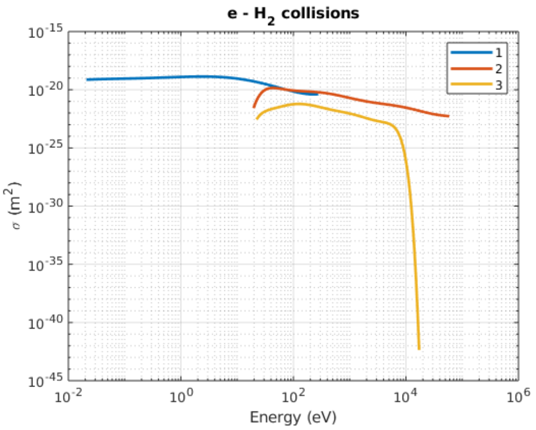

Figure A.2:
1. elastic scattering
2. e, H_2 → e,H_2^+,e (ion.)
3. e, H_2 → e,H^+,H,e (dissociative ion.)

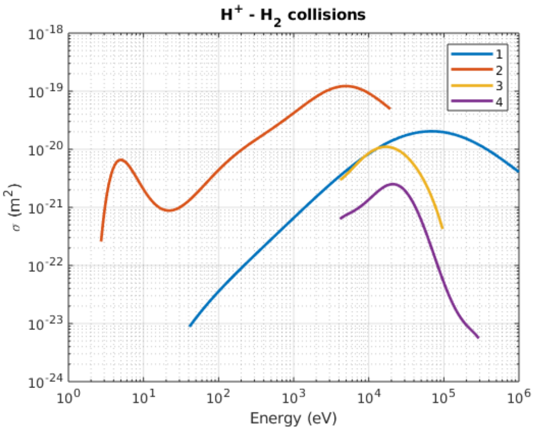

Figure A.3:
1. H^+, H_2 → H^+, H_2^+,e (ion.)
2. H^+, H_2 → H,H_2^+ (charge exc.)
3. H^+, H_2 → H^+,H,H^+,e
4. H^+, H_2 → H^+,H^+,H^+,2e

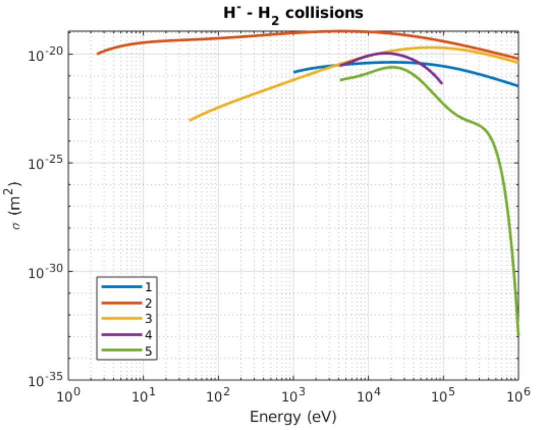

Figure A.4:
1. H^-, H_2 → H^+, H_2,2e (double el. detach.)
2. H^-, H_2 → H,H_2 (el. detach.)
3. H^-, H_2 → H^-,H_2^+,e (ion.)
4. H^-, H_2 → H^-,H,H^+,e
5. H^-, H_2 → H^-,H^+,H^+,2e

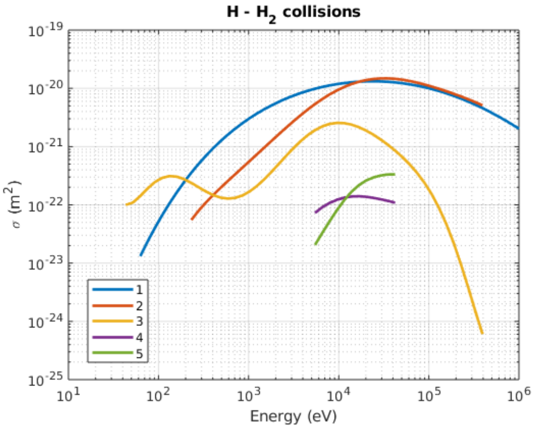

Figure A.5:
1. H, H_2 → H^+,H_2 (el. detach.)
2. H, H_2 → H,H_2^+,e (ion.)
3. H, H_2 → H,H_2^+ (charge exc.)
4. H, H_2 → H,H,H^+,e
5. H, H_2 → H,H^+,H^+,2e

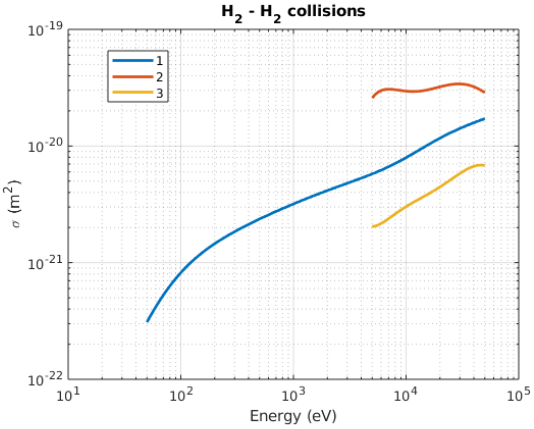

Figure A.6:
1. H_2, H_2 → H_2^+,H_2,e (proj. ion.)[41]
2. H_2, H_2 → H^+,e,... (proj. diss. ion)[37]
3. H_2, H_2 → H,e,... (proj. diss. ion)[37]

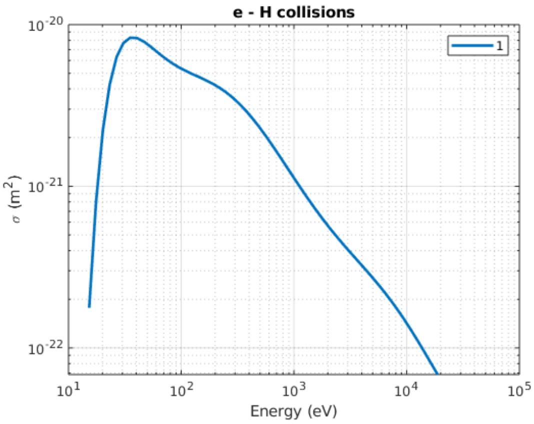

Figure A.7:
1. e, H→2e,H^+ (ion.)

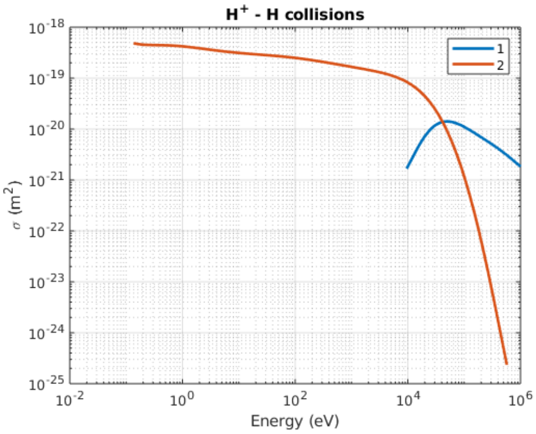

Figure A.8:
1. H^+, H → H^+,H^+,e (ion.)
2. H^+, H → H,H^+ (charge exc.)

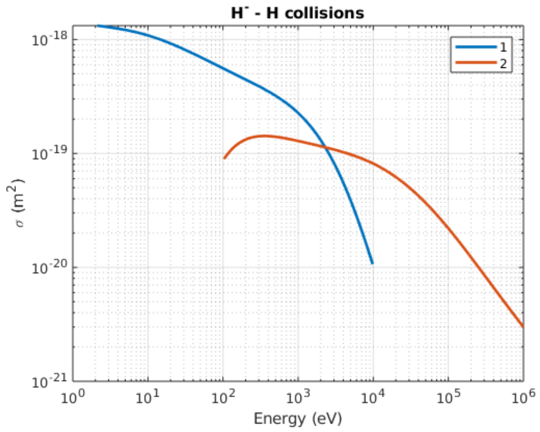

Figure A.9:
1. H^-, H → H^-,H_2^+,e (ion.)
2. H^-, H → H,H_2,e (el. detach.)

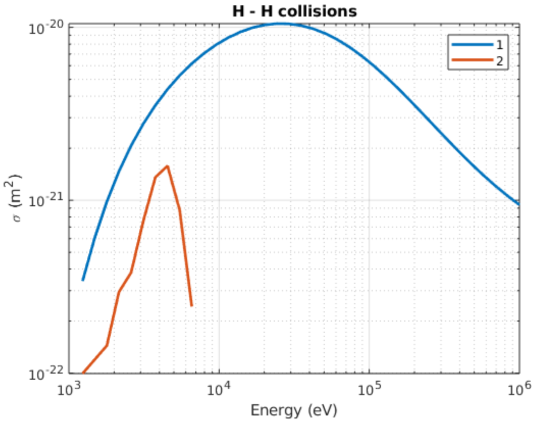

Figure A.10:
1. H, H → H^+,H,e (stripping)
2. H, H → H^+,H^- (charge exc.)

Bibliography

[1] International Atomic Energy Agency. Aladdin numerical database. `https://www-amdis.iaea.org/ALADDIN/`.

[2] Raúl A Baragiola. Principles and mechanisms of ion induced electron emission. *Nuclear Instruments and Methods in Physics Research Section B: Beam Interactions with Materials and Atoms*, 78(1-4):223–238, 1993.

[3] C. Barbeau and J. Jolly. Spectroscopic investigation of energetic atoms in a dc hydrogen glow discharge. *J. Phys. D: Appl. Phys.*, 23(1168), 1990.

[4] C Barbeau and J Jolly. Spectroscopic investigation of energetic atoms in a dc hydrogen glow discharge. *Journal of Physics D: Applied Physics*, 23(9):1168, 1990.

[5] Clarence F Barnett, Hamilton T Hunter, M Imogene Fitzpatrick, I Alvarez, C Cisneros, and Ronald A Phaneuf. Atomic data for fusion. volume 1: Collisions of h, h2, he and li atoms and ions with atoms and molecules. *STIN*, 91:13238, 1990.

[6] WM Black and EH Klevans. Theory of potential-well formation in an electrostatic confinement device. *Journal of Applied Physics*, 45(6):2502–2511, 1974.

[7] Loucas Georgiou Christophorou. *Electron—Molecule Interactions and Their Applications: Volume 2*, volume 2. Academic Press, 2013.

[8] William C Elmore, James L Tuck, and Kenneth M Watson. On the inertial-electrostatic confinement of a plasma. *The Physics of Fluids*, 2(3):239–246, 1959.

[9] GA Emmert and JF Santarius. A charge-exchange based model for the performance of gridded, spherical iec devices. part ii: molecular ions. *University of Wisconsin,(in preparation, 2006).*

[10] Ursel Fantz, H Falter, P Franzen, Dirk Wünderlich, M Berger, A Lorenz, W Kraus, P McNeely, R Riedl, and E Speth. Spectroscopy—a powerful diagnostic tool in source development. *Nuclear fusion*, 46(6):S297, 2006.

[11] DR Farley, DP Stotler, DP Lundberg, and SA Cohen. Modeling of hydrogen ground state rotational and vibrational temperatures in kinetic plasmas. *Journal of Quantitative Spectroscopy and Radiative Transfer*, 112(5):800–819, 2011.

[12] Philo T Farnsworth. Electric discharge device for producing interactions between nuclei, June 28 1966. US Patent 3,258,402.

[13] Igor B Gornushkin, Leslie A King, Ben W Smith, Nicoló Omenetto, and James D Winefordner. Line broadening mechanisms in the low pressure laser-induced plasma. *Spectrochimica Acta Part B: Atomic Spectroscopy*, 54(8):1207–1217, 1999.

[14] Hans R Griem. *Principles of plasma spectroscopy*, volume 2. Cambridge University Press, 2005.

[15] Yibin Gu and George H Miley. Experimental study of potential structure in a spherical iec fusion device. *IEEE Transactions on plasma science*, 28(1):331–346, 2000.

[16] Dietmar Hasselkamp, Hermann Rothard, K-O Groeneveld, Jürgen Kemmler, Peter Varga, and Hannspeter Winter. *Particle induced electron emission II*, volume 123. Springer, 2006.

[17] Morihide Higo, Satsuo Kamata, and Teiichiro Ogawa. Electron impact dissociation of molecular hydrogen and deuterium: Translational energy distribution of atomic hydrogen and deuterium (n= 3, 4, 5). *Chemical Physics*, 66(3):243–248, 1982.

[18] Robert L Hirsch. Inertial-electrostatic confinement of ionized fusion gases. *Journal of applied physics*, 38(11):4522–4534, 1967.

[19] Robert L Hirsch. Experimental studies of a deep, negative, electrostatic potential well in spherical geometry. *The Physics of Fluids*, 11(11):2486–2490, 1968.

[20] KM Hu and Edward H Klevans. On the theory of electrostatic confinement of plasmas with ion injection. *The Physics of Fluids*, 17(1):227–231, 1974.

[21] D. Moore J. Kachan and S. Bosi. Spatial distribution of ion energies in an inertial electrostatic confinement device. *Physics of Plasmas*, 10(596), 2003.

[22] J. Kachan and S.Collins. Measurements of ion energy distributions by doppler shift spectroscopy in an inertial-electrostatic confinement device. *Physics of Plasmas*, 8(1299), 2001.

[23] LJ Kieffer and Gordon H Dunn. Dissociative ionization of h 2 and d 2. *Physical Review*, 158(1):61, 1967.

[24] J. Kipridis. The application of doppler h_α spectroscopy to the prediction of experimental fusion rates in a deuterium-filled inertial electrostatic confinement device. 2009.

[25] J Kipritidis, M Fitzgerald, and J Khachan. Spectroscopic determination of electron energies in a discharge of atomic h produced by a monoenergetic electron beam. *Journal of Physics D: Applied Physics*, 40(17):5170, 2007.

[26] J Kipritidis, J Khachan, M Fitzgerald, and O Shrier. Absolute densities of energetic hydrogen ion species in an abnormal hollow cathode discharge. *Physical Review E*, 77(6):066405, 2008.

[27] Robert A Langley, J Bohdansky, W Eckstein, P Mioduszewski, J Roth, E Taglauer, EW Thomas, H Verbeek, and KL Wilson. Data compendium for plasma-surface interactions. *Nuclear Fusion*, 24(S1):S9, 1984.

[28] GW McClure. Differential angular distribution of h and h+ dissociation fragments of fast h 2+ ions incident on h 2 gas. *Physical Review*, 140(3A):A769, 1965.

[29] Maximilian Claus Constantin Messmer. Towards advanced operation modes of magnetic and electrostatic confined fusion machines. 2019.

[30] George H Miley, Yibin Gu, John M DeMora, Robert A Stubbers, Timothy A Hochberg, Jon H Nadler, and Robert A Anderl. Discharge characteristics of the spherical inertial electrostatic confinement (iec) device. *IEEE Transactions on plasma science*, 25(4):733–739, 1997.

[31] George H Miley and S Krupakar Murali. Inertial electrostatic confinement (iec) fusion. *Fundamentals and Applications*, 2014.

[32] S Krupakar Murali, John F Santarius, and Gerald L Kulcinski. Effects of the cathode grid wires on fusion proton measurements in inertial-electrostatic confinement devices. *IEEE Transactions on Plasma Science*, 39(2):749–755, 2011.

[33] National Institute of Standards and Technology. Nist atomic spectra database. `https://www.nist.gov/pml/atomic-spectra-database`.

[34] Masami Ohnishi, Hodaka Osawa, Kiyoshi Yoshikawa, Kai Masuda, and Yasushi Yamamoto. Particle-in-cell simulation of inertial electrostatic confinement fusion plasma. *Fusion technology*, 39(3):1211–1216, 2001.

[35] Hodaka Osawa, Takehiro Tabata, and Masami Ohnishi. Numerical study on glow discharge of iec fusion. *Fusion science and technology*, 47(4):1270–1274, 2005.

[36] O.Shrier, J. Kachan, S. Bosi, M.Fitzgerald, and N.Evans. Diverging ion motion in an inertial electrostatic confinement discharge. *Physics of Plasmas*, 13, 2006.

[37] AV Phelps. Cross sections and swarm coefficients for h+, h2+, h3+, h, h2, and h- in h2 for energies from 0.1 ev to 10 kev. *Journal of Physical and Chemical Reference Data*, 19(3):653–675, 1990.

[38] Todd H Rider. A general critique of inertial-electrostatic confinement fusion systems. *Physics of Plasmas*, 2(6):1853–1872, 1995.

[39] M Eugene Rudd. User-friendly model for the energy distribution of electrons from proton or electron collisions. 1989.

[40] F Sigeneger and R Winkler. Self-consistent analysis of a helium plasma in a cylindrical hollow cathode. *Plasma chemistry and plasma processing*, 25(2):147–168, 2005.

[41] Tatsuo Tabata and Toshizo Shirai. Analytic cross sections for collisions of h+, h2+, h3+, h, h2, and h- with hydrogen molecules. *Atomic Data and Nuclear Data Tables*, 76(1):1–25, 2000.

[42] Timothy A Thorson. Ion flow and fusion reactivity characterization of a spherically convergent ion focus. 1997.

[43] Timothy Arthur Thorson, Roger D Durst, Raymond J Fonck, and Louis Patrick Wainwright. Convergence, electrostatic potential, and density measurements in a spherically convergent ion focus. *Physics of Plasmas*, 4(1):4–15, 1997.

[44] Ivon Virgilova Tzonev, John M DeMora, and George H Miley. Effect of large ion angular momentum spread and high current on inertial electrostatic confinement potential structures. In *Proceedings of 16th International Symposium on Fusion Engineering*, volume 2, pages 1476–1481. IEEE, 1995.

[45] Vahid Vahedi and Maheswaran Surendra. A monte carlo collision model for the particle-in-cell method: applications to argon and oxygen discharges. *Computer Physics Communications*, 87(1-2):179–198, 1995.

[46] ID Williams, J Geddes, and HB Gilbody. Balmer α emission in collisions of h, h+, h2+ and h3+ with h2. *Journal of Physics B: Atomic and Molecular Physics*, 15(9):1377, 1982.

[47] K Yoshikawa, K Takiyama, T Koyama, K Taruya, K Masuda, Y Yamamoto, T Toku, T Kii, H Hashimoto, N Inoue, et al. Measurements of strongly localized potential well profiles in an inertial electrostatic fusion neutron source. *Nuclear Fusion*, 41(6):717, 2001.